Politecnico di Torino

ScuDo
Scuola di Dottorato ~ Doctoral School
WHAT YOU ARE, TAKES YOU FAR

Doctoral Dissertation
Doctoral Program in Energy Engineering (36^{th}cycle)

Boosting the performance of gyrotron resonators: optimization methods for longitudinal and azimuthal cooling

By

Rosa Difonzo

******

Supervisors:
Prof. L. Savoldi, Politecnico di Torino
Prof. A. Cammi, Politecnico di Milano

Doctoral Examination Committee:
Prof. E. Chiavazzo, Politecnico di Torino
Prof. P.A. Di Maio, Università degli Studi di Palermo (reviewer)
Dr. M. Cavinato, Fusion for Energy (reviewer)
Prof. K.A. Avramidis, National and Kapodistrian University of Athens
Dr. B.E. Ghidersa, Karlsruhe Institute of Technology

Politecnico di Torino
2024

Declaration

I hereby declare that, the contents and organization of this dissertation constitute my own original work and does not compromise in any way the rights of third parties, including those relating to the security of personal data.

Computational resources were provided by HPC@POLITO, a project of Academic Computing within the Department of Control and Computer Engineering at the Politecnico di Torino (http://www.hpc.polito.it)

Rosa Difonzo
2024

* This dissertation is presented in partial fulfillment of the requirements for **Ph.D. degree** in the Graduate School of Politecnico di Torino (ScuDo).

To Neta, Rut, Ella and Camilla, with the hope that science and technology would facilitate the path toward a bright future of justice and peace

A Neta, Rut, Ella e Camilla, nella speranza che scienza e tecnologia facilitino il percorso verso un futuro luminoso fatto di giustizia e pace

Acknowledgements

Many people contributed with help and support in this long and challenging journey. I would like to address the first thank to my supervisors. Thank you, Laura, for giving me the opportunity to work with you, creating the space to bring my abilities to the fullest. I really appreciate your constant work in guiding me to see the good in my accomplishments and to understand my strengths. When I look at myself now, I realize that a lot of my development is due to your trust in giving me responsibility and your motivation to keep getting better. Thank you, Prof. Cammi, for your dedication in supporting me from goal setting to the smallest steps, for your endless availability and kindness. I will take with me our discussions, which ranged over the most diverse topics, and especially your critical thinking and honest research method, which I tried to learn from you.

Un grazie speciale va alla mia famiglia. Ai miei genitori, per avermi sempre supportata in ogni mia scelta, credendo in me e nelle mie decisioni senza mai contrastarle. La fiducia e la libertà di decidere per la mia vita, anche quando non era ciò che voi avreste scelto, sono stati il regalo più grande che poteste farmi. Gran parte della persona che sono oggi è sicuramente merito vostro, grazie per esservi buttati in questa sfida che è la genitorialità e per averci messo tutti voi stessi. Grazie per le infinite possibilità che mi avete dato e per quei no, a volte molto difficili da accettare, ma sicuramente formativi. Grazie per aver scoccato la freccia ed averla lasciata andare. Ringrazio i miei fratelli, per avermi sempre mostrato, con i loro sguardi e abbracci, la stima che hanno in me, ma soprattutto per avermi infastidita più che potevano (è a questo che servono i fratelli, no?) anche quando tornavo a casa per poco tempo, dando forza a me e ai nostri legami. Grazie Domenico, per non esserti mai fatto bloccare dal numero di kilometri da guidare pur di rivedermi. Grazie Michi, per la tua sensibilità, la cura che hai per ognuno di noi e per il modo speciale che hai di farci ridere. Grazie Federica, per aver scelto di far parte di questa famiglia, per portare sempre il tuo tocco in tutti i momenti di condivisione e per aver

accolto nella tua vita le differenze culturali. Grazie Camilla, per la gioia immensa che hai portato nelle nostre vite, per aver orientato il mio sguardo al futuro e il mio vivere al presente!

I also want to thank the MAHTEP group, especially my office mates, for listening to each other, for fully understanding the difficulties in this shared journey, and for the space we created, always open to complaints xD. A special thank goes to Sofia, my mate from the beginning until the end, for the long video calls working together during the covid-period, for the support in our most private life difficulties and the essential help even in our thesis details. I get emotional looking at the strong bridge we built between our so diverse personalities! My most tender thanks go to Eleonora, you are always ready to help anyone is in need and you cannot imagine how your compliments, supportive phrases and hugs helped me through many difficult moments. I am really impressed with your ability to analyze my sleeping pattern! Matteo, I am so happy with the relationship we have today, that we were able to learn not only to work together and appreciate each other, but even to open up to each other by allowing vulnerability. Thank you Elia for joining me in the test challenge, I couldn't ask for a better partner in breaking pipes. Gianvito, you are the latest discovery as a good interlocutor, from work related topics to political issues and it was a nice surprise, thank you for the very human support you showed. Hossein, we shared this journey from the beginning and I admire your continuous struggle in trying to convert me to solar power, thank you for sharing with me the PSA adventure. Ceci, I am impressed by our late communication development through looks! Farzaneh, thank you for paying so much attention to my daily mood, it was a pleasure to share and exchange our cultural backgrounds and a big fortune to be there for each other in our mutual fears. I want to thank again each one of you and Alessio, Daniele P, Daniele L., Aldo, and all the others, for being there for me, in different ways, in one of the most difficult periods of my life. The green office has become one of the safest places for me.

Exclusive thanks go to Andrea, first of all for convincing me to join you in starting a PhD: I will blame you forever for all the pain that this brought to me, but give you as well the merit of the many joys that came in these years. I look backward with smiling eyes at our friendship development, from nights of writing scientific abstract together, the powerful fights, toward knowing each other better and better until becoming good reciprocal confidants and supporters.

I want to address a firm thank to all the international colleagues I had the honor to work with in these years, in particular Alberto, Sebastian and Kostas, for the constant ideas exchange and availability to answer to all my questions, and also the KIT for hosting me for the test campaign.

I am truly grateful to Prof. Giannakoglou, for hosting me and opening the door to his important knowledge. I want to thank as well the entire PCOpt group for welcoming me as part of the group and showing me the beauties of Athens. A special thank goes to Vaggelis, for the time, patient and passion he put in helping me during my stay at NTUA, and to the entire office and whoever was stopping by, joining our crazy long language conversations.

I would like to address heartfelt thanks to my Turin family, to the ones still living these beautiful streets and the ones who left toward other places, we learned together family links do not depends on physical distance. I want to mention Elisa, for your sweetness and always opening your door (even the car one) anytime I have been in need; Dionisio, for the most free speeches I could have with a friend, unencumbered by any kind of judgment; Hedyeh, my precious kuchulu, for allowing a continue reciprocal contamination of our very different selves, always driven by a huge amount of love; Giovanni, my partner in desserts seeking, for never agreeing, for so much sharing, from books to Greek island adventure; Gianluca, for the level of intimate talks that even the jet lag and meeting twice a year cannot change, you never end surprising me with your diverse knowledge; FDL, for always showing up, at every kind of request and proposal, from the scientific help, the concerts to the private life reciprocal support, Carry, for your always challenging questions, and constantly being ready for having fun! Pablito, my LaTeX savior, thank your for your diverse helps, from the most technical things to the social conversation and your care. Simona, you helped me stand up when I just wanted to lay down, every weekend you are in Turin my heart is full of joy; Sofia, I admire you so much, thank you for caring and showing love even in deep disagreement. And thanks to the newest family I found; Nappo, my one month roommate, for how much we shared already in this fast growing friendship, and for bringing so much culture and curiosity in our Saturday nights; Ale and Carlos, for your very very warm love, that I can feel in each word and hug.

I would like to express my profound gratitude to the whole Nusan family, for welcoming me and making me feel at home, for always showing support and pride

in each of my achievements. Every good word coming from each one of you played a decisive role in helping me overcoming obstacles throughout this year. I truly feel privileged to be part of this family.

David Dov Nusan, you are my greatest supporter. And I feel blessed for meeting you in my life. Thank you for always believing in me, for repeating me that I would make it, for being so patient with me in this very hard times. Thank you for the constant challenge, for the growing together, hand in hand, for the numerous adventure we shared (even for that hike I thought I would die) and for bringing flowers and light in my life. Your positive energy, your listening, your craziness and your wisdom made this journey much more pleasant.

Abstract

One of the main challenges for the realization of future fusion reactors for energy production is the heat removal from many systems and components. One of these components is the resonant cavity of gyrotrons, a candidate technology for the Electron Cyclotron Resonance Heating, to be used as external heating of the plasma in magnetic confined fusion machines. During the normal operation of gyrotrons, MWs of power are transferred to the plasma in the form of radiofrequency waves, while a high amount of energy loss is released on the cavity inner wall, with a heat flux peak that can reach 25 MW/m^2. The resonant cavity constitutes the gyrotron component where the the interaction between the electron beam and the electromagnetic field occurs, determining the amplification of the RF wave at the desired frequency, thanks to its geometry and by a proper tuning of the magnetic field and beam parameters. Because of the importance of the cavity inner wall shape, its cooling plays a crucial role limiting the temperatures on the cavity inner wall, to limit the cavity expansion and hence the frequency down-shift of the output wave. Moreover, the peaked axial shape of the heat flux loading on the cavity inner wall, drives a similar temperature profile. In other words, high thermal gradient can be experienced in the cavity, leading to high thermal stresses, that could reach the yield strength of the material (Glidcop for European gyrotrons). In addition, the cooling system of the gyrotron sets a limit on the allowed pressure drop to around 6 bar for the cavity. The mentioned requirements are to be accounted for in the design of an efficient cooling system for the gyrotron cavity and bring to the need of an optimization study: the minimization of the frequency shift is required while monitoring pressure drop and stresses.

In the present dissertation, the problem of the cooling of the gyrotron cavity is faced through several strategies. Starting from the analysis of the already existing cooling solution and the proposed ones for the European gyrotrons, some improvements are proposed for them. Moreover, different optimization studies, making use

of different optimization methods, are presented. The considered cooling strategies can be classified for the main direction of the coolant flow: longitudinal and azimuthal. For both, designs with and without ducts are considered.

Considering the longitudinal direction as the main one for the coolant flow, an optimized annular configuration is designed. An evolutionary algorithm is coupled to a thermos-mechanical model with finite elements, defining an optimization work in the thermos-mechanical field. The minimization of the displacements is aimed, to minimize the frequency shift, and avoiding yield strength. The obtained pressure drop is also under the allowed system limit. An advanced design with longitudinal mini-channels is also presented here, characterized by the reduction of the temperature peak and the pressure drops with respect to previous mini-channels designs. Both these solutions, the annular one and the mini-channels one, present better results compared to the actual cooling solution used for the European gyrotrons, the Raschig Rings one.

Concerning the design of cooling configurations exploiting the azimuthal direction of the flow, two optimization studies are presented here. They both use the adjoint-based topology optimization method. A solution using azimuthal microchannels is optimized in terms of flow rate distribution in the microchannels, to reduce the temperature gradients that lead to thermal stresses. In this case, the optimization work is done considering only the hydraulic physic of the problem. Two different strategies are compared: one aiming to an homogeneous flow rate distribution over channels with density following the heat load curve and the other based on equally spaced channels with a peaked flow rate distribution. The main outcomes are the better improvement of the cost function in the first case as well as the easier manufacturability of the geometry found. The second optimization work starts from a configuration that forces the flow in the azimuthal direction, without the use of ducts. In this case, the optimization problems is defined in the thermal-hydraulic field. Comparing the final result with the one obtained with the evolutionary optimization algorithm, the latter presented better temperature profile, with almost 70 $^{\circ}$ C less in the temperature peak. Further parametric studies could be conducted to obtain better results with the topology method.

Some validation studies have been conducted for the mini-channels cooling system, being the more advanced one in the exploration path toward an alternative more efficient solution for the cooling of European gyrotron cavities. The importance of

the model validation is due to its double use of predicting gyrotron performances and guiding the design of new cooling configurations. A cavity mock-up equipped with straight mini-channels allowed the validation of the hydraulic part of the model. Thermal results were also compared from a second test campaign performed on a second cavity mock-up at KIT. In this work, the simulated temperature are higher than the measured ones and, even if similar qualitative profiles can be defined with the several thermocouples available, the quantitative discrepancies cannot be justified with the available information on the measurement uncertainties. Further test campaigns are scheduled with improved test set-up and measurement instrumentation.

Overall, by comparing the results of the different optimization strategies analyzed, the use of the longitudinal direction as main flow direction in the cooling presents higher sensitivity to the modification and optimization, remaining the preferable one to be further analyzed. The experimental activities are encouraging with respect to the models prediction of the designed cooling configurations.

Contents

List of Figures

List of Tables

Nomenclature

Roman Symbols

$\ddot{Q}$	Heat flux (W/m^2)
$\dot{m}$	Mass flow rate
$\dot{Q}$	Power per unit length
$\mathscr{A}$	Matrix of the coefficient of the state matrix
$\mathscr{B}$	Matrix of the coefficient of the input matrix
$\mathscr{F}$	Interface velocity
$\mathscr{L}$	Least square function
$\mathscr{S}$	Source term of level set function
$\mathscr{U}$	Input matrix
$\mathscr{X}$	State matrix
A	Area
a	Coefficient
C	Coefficient
C	Massive heat capacity
c_p	Specific heat
D	Diameter

D	Experimental result
d	Diameter in Xs and Ds
E	Comparison error metric
er	Error
F	Generic function
f	Wave frequency (Hz)
G	Constraint definition
g	Inequality constraint
h	Equality constraint
h	Reference cell size
J	Cost function
k	thermal conductivity
L	Length
l	Turbulent scale
M	Mass
N	Number of
P	Production term
p	Pressure
Q	Heat load (W)
R	Resistance
r	Ratio
S	Simulation result
s	Strain rate tensor

T	Temperature
t	Time
u	Uncertainty
V	Covariance matrix
V	Volume
w	Vorticity tensor
w	Weights in cost function
w	weight in cost function
X	Sensitivity coefficient vector
X	Set of design variable for unconstrained problem
x	Variable

Greek Symbols

α	Impermeability field
β	Regularized and projected α field
χ	Material indicator in topology
Δ	Difference
δ	Small variation
ε	Turbulent dissipation rate
η	Immigration rate in the Biogeography-Based Optimization algorithm
Γ	Generic transported quantity
γ	Expansion coefficient?
ι	Thickness of interface
κ	Kinetic turbulent energy

Λ	Additional contribution to transport equation
λ	Linear expansion coefficient
μ	Dynamic viscosity
ν	Kinematic viscosity
Ω	Source term
ω	Specific dissipation rate
Φ	Level set variable
ϕ	Reduced normal stress
ψ	Penalty coefficient
Ψ'	Coefficient of constant parameters
σ	Von Mises stress
τ	Pseudo time
τ	Turbulent time scale
θ	Computed order of convergence
Υ	Model coefficient for the Λ term
φ	Elliptic blending factor
ξ	Emigration rate in the Biogeography-Based Optimization algorithm
ζ	Model coefficient

Superscripts

T	Transpose

Subscripts

0	Initial
21	Between the first and the second one

beam	Beam
c	Coolant
cells	Cells
ch	channel
D	Experimental
dev	deviation
el	Electron
f	Fluid
he	Heated
hy	Hydraulic
I	Individuals
i	Internal
in	Inlet
input	Input
j	j-th set point
loop	Hydraulic loop without mock-up
m	Metal
mean	Mean
mv	Multivariate
num	Numerical
o	Outer
out	Outlet
p	Pressure drop

RF Radiofrequency

s Heat exchange surface

target Target

target target

th Thermal

tot Hydraulic loop + mock-up

total Fluid + solid

v Volume

val Validation

Acronyms / Abbreviations

ASME American Society of Mechanical Engineering

ATO Adjoint-based Topology Optimization

BBO Biogeography-Based Optimization

BC Boundary Conditions

cal Inductive heat load calibration factor

CPs Control Points

disp Radial displacement

EB Elliptic Blending

EC External cylinder

ECRH Electron Cyclotron Resonance Heating

ECRM Electron Cyclotron Resonance Maser

ED Electro-dynamic

ESR Electron Spin Resonance

GA Genetic Algorithm

GCI Grid Convergence Index

HSI Habitat Suitability Index

HTC Heat Transfer Coefficient

KPI Key Perfomance Indicator

MC Mini-channels

MUCCA MUlti-physiCs tool for integrated simulation of CAvity

NMR Nuclear Magnetic Resonance

NormFactor Normalization Factor

Nu Nusselt number

Pr Prandtl number

QF Quality factor for gyrotron

RANS Reynolds-average Navier Stokes

Re Reynolds number

RF Radio Frequency

RR Raschig Rings

stdev Standard deviation

TH Thermal-hydraulic

thick Thickness

TM Thermo-mechanic

WS Water-stopper

Chapter 1

Introduction

The forecast increase of the world population together with improvement in society's life standards results in an increasing demand for energy consumption [1]. In parallel, an average increase of 0.06 $^{\circ}C$ per decade of the Earth temperature has been observed since 1850 [2]. As a result 2023 was the warmest year since the global record began, with 1.18$^{\circ}C$ above the 20-th century average (13.9$^{\circ}C$), for the average Earth temperature. The Environmental Defence Fund listed nine lines of evidence [3] that humans activity causes climate change, in particular with the production of CO2. Modern society needs to face, hence, the challenge of producing enough energy for the increasing need while reducing the greenhouse gases emissions to contrast the climate change. For these reasons, the research & development in new systems for energy production increased in the last decades, such as photovoltaic, wind power, geothermal and so on, with the advantageous characteristic of a theoretic infinite availability and very low CO2 production, if compared to traditional fossil fuel power plants. On the other hand these energy systems presents the disadvantage of being intrinsically intermittent, seriously endangering the management of the electric grid stability and resulting totally unfit to meet the baseload of electricity demand. Moreover, not being constantly available, they require the development of advanced storage systems to meet the demand in time. Nuclear fission power plants constituted and still are an important contribution to the base load of the energy request. Meanwhile the nuclear research has also turned toward the development of nuclear fusion power plants. Such a technology would keep the continuous availability and independence from external factors of energy production and low emissions of the fission technology while overcoming the production of long life

radioactive waste, using a fuel with infinite availability and presenting intrinsic safety: no reactivity accident is possible due to the absence of chain reaction.

In this chapter, a general introduction on nuclear fusion machines is reported in the session 1.1, while more details are given about the Gyrotron in section 1.2, with its working principle and applications. In section 1.3 the issue of the cooling of the resonant cavity, an important component of Gyrotrons, is introduced and analyzed, being the object of study of this thesis. Section 1.4 explains the organization of the thesis.

1.1 Nuclear fusion machines and plasma heating

A nuclear fusion reaction is a process in which two light nuclei interact, by overcoming their electromagnetic repulsion, to form a single compound nucleus, that typically decades into a heavier nucleus and a particle, releasing nuclear binding energy in the form of kinetic energy of the reaction products [4]. Nuclear fusion reactors exploit this principle to produce thermal energy, then converted in electric energy.

Among the considered fusion reactions for nuclear fusion machines, the easiest to reproduce on earth uses two hydrogen isotopes: deuterium and tritium, which basically does not exist on earth due to fast decay. For this reason it needs to be produced and the possible processes are the interaction of neutrons with Li, B^{10} and Deuterium or by fission of uranium and plutonium. The reaction is reported in Eq. 1.1

$$D + T \rightarrow He + n + 17MeV \tag{1.1}$$

In order for fusion to occur in plasma and ensure its self-sustainement, the following conditions are necessary:

- High plasma temperature $T \sim$10-20 keV
- High plasma density*energy confinement time (respectively n and τ_e):
  - $n \sim 10^{20} - 10^{21}\ m^{-3}$, $\tau_e \sim 1s \rightarrow$ magnetic confinement;

– $n \gg$ solid, τ_e short$\rightarrow$ inertial confinement.

The combination of the previous three conditions derives from the Lawrence criterion or triple product, reported in Eq. 1.2.

$$n * \tau_e * T \geq 10^{21} keV * s/m^3 \tag{1.2}$$

One important challenge for the realization of fusion machines is the confinement of plasma, for which two main ways are being followed in the research programs around the world: inertial and magnetic confinement.

- Inertial confinement consists in generating a high density plasma ($10^{30} ions/m^3$), in order to limit its own expansion thanks to the inertia for a confinement time sufficient for the ignition [5], without using any external confinement.
- Contrary, in magnetic confinement the movement of the plasma charged particles is governed by external magnetic field lines.

Most of the research projects about fusion for energy production aims to use magnetic confinement, which in turn can be obtained through two technological methods:Stellarator and Tokamak.

- In stellaretors, external helical coils are adopted to produce twisted magnetic field lines [5]. Once the confinement is reached, this configuration presents a better stability with respect to tokamaks.
- Tokamaks use three types of magnets. A central solenoid characterized by a pulsed current produces a magnetic field. The consequent flux induces an electric field, and hence a current flowing in the plasma in the toroidal direction. A poloidal magnetic field is generated by the latest current, thanks to Amper law. A set of toroidal field coils is also located around the torus, to generate toroidal magnetic fields. The sum of these two contributions leads to a helical field able to confine the plasma. Morover, poloidal magnets are used to generate a vertical field (figure 1.1). Tokamaks are easier to construct and are better at maintaining plasma temperature.

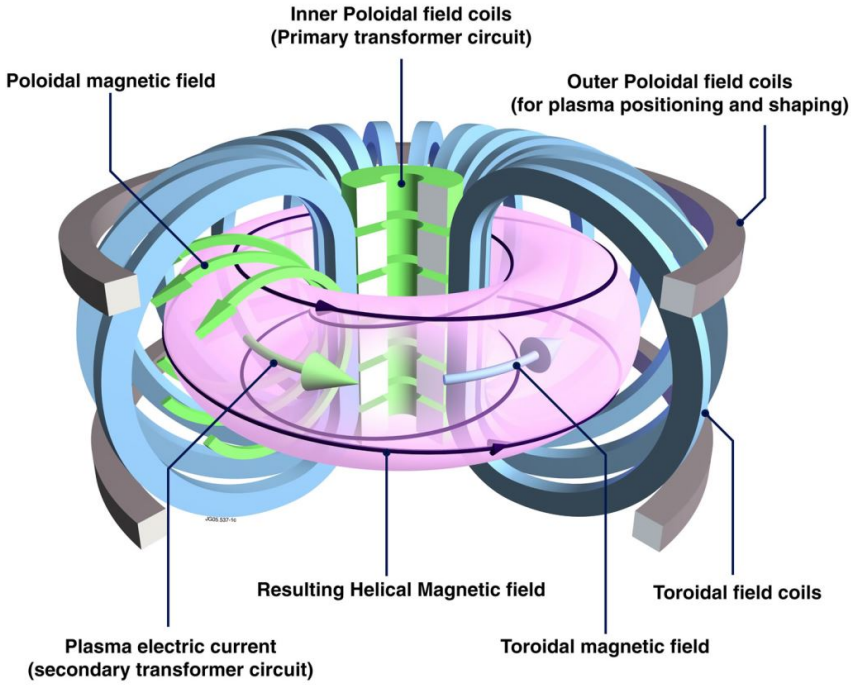

Fig. 1.1 Sketch of a tokamak. Image taken from [6].

The majority of the researchs on fusion machines are based on the tokamak concept.One of the most important project is ITER, an international experiment carried out by seven domestic agencies, one for each international partner: European Union, Russia, China, Japan, USA, India and South Korea. The European domestic agency is Fusion for Energy. An important example of experimental stellaretor project, instead, is the W7X in Germany. A noteworthy project is also the tokamak SPARC, acronym for "Smallest Possible ARC" (affordable, robust, compact), under development by the MIT Plasma Science & fusion Center in collaboration with private fusion startups [7].

As already mentioned, an important requirement for fusion to occur is that the plasma temperature should reach 150 million °C, and maintain this temperature to extract energy. For this reason, different ways to heat the plasma are used in a fusion machine: intrinsic and auxiliary. Intrinsic ohmic heating is used for the start-up of the fusion reaction and it occurs thanks to the plasma electrical resistance when inductive current flows into it. It is more effective in the early stage as the plasma resistance is higher at lower temperature. Another important intrinsic heating, happening after the fusion reactions started, exploits the high energy alpha particles,

product of the D-T reaction: through collision they transfer energy to the plasma, playing an important role in the self-sustenance of the fusion reaction. Auxiliary methods use electromagnetic waves with appropriate frequency to transfer energy to plasma particles, or neutral beam injection, constituted by high energy particles shot into the plasma and transferring their energy to plasma particles through collisions with them.

The electromagnetic wave method can be classified in three groups, depending on the type of resonance and species (electrons or ions) [8]:

- ion cyclotron resonance heating (ICRH): frequency range 30-120 MHz;
- lower hybrid heating (LHH): frequency range 1-8 GHz;
- electron cyclotron resonance heating (ECRH): frequency range 80-200 GHz.

For the ECRH particular vacuum tube are used: the gyrotrons.

1.2 The gyrotron: working principle and applications

1.2.1 Working principle and components

The gyrotron is high power (order of MW) long pulse (order of hours) oscillator that produces radio frequency (RF) waves in the millimeter and sub-millimeter range, covering the gap between microwaves tubes and laser. Its working principle is based on the Electron Cyclotron Interaction. By migrating to lower energy levels, electrons provide a portion of their energy to an electromagnetic wave. This happens in a strong magnetic field, generating the rotational component of the electron motion, thanks to the Lorentz force, from which the name gyro-tron [9].

In Figure 1.2 a schematic view of the gyrotron is visible. Its main components are the magnetic injection gun (MIG) or electron gun, the magnets, the beam tunnel, the resonant cavity (or resonator), the launcher, a set of quasi-optical mirrors, the RF output diamond window and the collector.

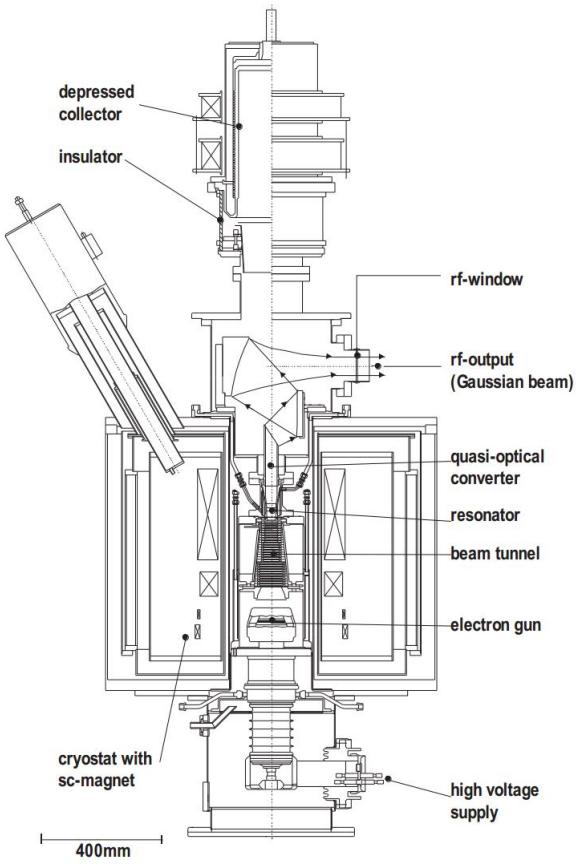

Fig. 1.2 Scheme of a gyrotron (taken from [10]).

The MIG, operating in the temperature-limited region, generates an annular electron beam meeting the necessary conditions for the cyclotron resonance interaction in the cavity [9]. The velocity of the electrons in the beam has an axial component, allowing them to proceed toward the resonator [10], and transverse component determining the rotational motion. The result of the two is an helical trajectory, following the helical path of the external field lines of force. The eventual parasitic oscillations are absorbed in the beam tunnel. In the resonant cavity, a portion of the beam energy is converted in RF power at the desired frequency and mode thanks to the magnetic field generated by the main coils in which the cavity is immersed. The obtained microwave power passes through the launcher and a set of mirrors, where, in modern gyrotrons, is converted in a Gaussian wave [8] and focused toward the output vacuum window, transparent to the wave. The so-called spent electron beam overcomes the launcher toward the collector where its power is dissipated in the form of thermal energy, usually with Hypervapotron technology.

In order to asses the performance of gyrotron we may look at the following key parameters.

- The **electron efficiency** gives information about the fraction of electrons kinetic energy is successfully converted in millimeter wave radiation and it is defined as the ration between the radiofrequency power (Q_{RF}) generated in the resonant cavity and beam power (Q_{beam}) (see Eq. 1.3).

$$\eta_{el} = \frac{Q_{RF}}{Q_{beam}} \tag{1.3}$$

  It can also be defined in relation to the pitch $\alpha = \frac{v_\perp}{v_\parallel}$ (being $v_\perp$ and $v_\parallel$ the transverse and axial components of the velocity respectively), as in Eq. 1.4.

$$\eta_{el} = \eta_\perp \frac{\alpha^2}{1+\alpha^2} \tag{1.4}$$

  Where $\eta_\perp$ is the transversal efficiency, indicating how efficiently the transverse energy has been transferred to the RF field [11].

- The **quality factor** is fundamental to measure the "efficiency" of the resonator, characterizing its global losses. It is defined as the ratio between the energy stored in the resonator W and the total power losses Q_{loss}, multiplied by the angular frequency of the wave $\omega = 2\pi f$ (f is the frequency in Hertz) as reported in Eq. 1.5 [8].

$$QF = \omega \frac{W}{Q_{loss}} \tag{1.5}$$

  It gives indicates of how efficiently the energy of the electromagnetic wave is confined, more precisely about the stability and precision of the wave frequency.

1.2.2 Gyrotron applications

The research and development of gyrotron was mainly catalyzed by its prospective use in confined fusion plasma. As a high power source, it exhibits a number of special advantages over other millimeter/submillimeter wave generators, such as

vacuum- or semiconductor-based devices. Because of its power capability it is the best candidate for the Electron Cyclotron Resonance Heating (ECRH). Compared to other heating techniques, the ECRH has two key advantages: it can heat the plasma in specific areas and it enables the launching structure to be located distant from the plasma. In controlled nuclear fusion applications, gyrotron frequency ranges from 80 to 200 GHz [11].

Remaining in the field of nuclear fusion, gyrotrons can be a useful tool for plasma diagnosis, in particular for the Collective Thomson scattering. This measuring method can be used to determine the temperature of the electrons in the plasma, the temperature of the bulk ions, the measurement of impurity ions, etc. The measurement exploits the scattered signal detection from a specific imposed frequency. For this purpose mainly gyrotrons with frequency 60 GHz [12][13] and 354 GHz [14] are used.

Exploiting their heating capability, Gyrotrons found application in industrial processes, such as ceramic sintering [15] or other material processing [16]. The use of microwave, in facts, presents better uniformity and volumetric heating results if compared to oven heating [17]. The two ways millimeter wave energy can be used in material processing are:

- as a beam for the surface treatment like surface hardening, drying, etc., by using focusing mirrors to guide the millimeter wave into the beam
- volumetric heating by spreading the millimeter wave energy in a large volume.

The aim of volumetric heating and focused surface treatment is obtained by means of an applicator [18], which is an overmoded cavity particularly designed for sample treatment. Initially, fusion scopes designed gyrotrons were used for industrial application, with several disadvantages like big size, heavy weight and large power consumption. New type of low frequency, medium power, light gyrotrons (by operating at second harmonics) has been created to address these drawbacks, specifically designed for material processing applications. Gyrotrons operating in the 20–35 GHz frequency range are mostly employed in millimeter wave industrial applications [15] [16] [19] [20]

Gyrotrons are adopted also in the submillimeter wave radiation (also called THz radiation), ranging from 300 GHz to 3 THz. These kind of radiation can

penetrate through several kind of materials like clothes, paper, wood, etc., but they are absorbed in the atmosphere. Their absorption strongly depends on the water contained in the traveling media, hence this property can be exploited to estimate the water percentage in materials. Gyrotrons can produce waves up to 2 THz with power in the range 10-1000 kW, making them advantageous in this field. On the other hand, the major technological challenge is the required magnetic field, 20-40 T, since it is proportional to the frequency. The future development of THz gyrotrons can gain advantage on the current research on superconducting material like NbTi, Nb_3Sn, but the manufacture and maintenance of the cryostat, to cool down the superconducting material below the Curie temperature, make the THz gyrotrons advancement difficult. The main application of THz gyrotrons are Electron Spin Resonance (ESR) and solid state Nuclear Magnetic Resonance (NMR) spectroscopy, radioactive material detection and as a radiation source in imaging and sensing for inspection and control in different industrial processes. A comprehensive overview of advantages and applications of THz gyrotron can be found in [21].

Raytheon developed for the US Air Force Research Labs the Active Denial System (ADS): a non lethal weapon system that produces focused millimeter wave energy beam capable of inducing intolerable heating sensation. This allows to dismiss the human target without injury and can be used at a distance beyond the effective range of small arms [22]. This kind of technology uses 95 GHz wave radiation.

Among the other gyrotrons applications we have:

- atmospheric monitoring, in particular for humidity detection using 183 GHz oscillators [23] (because the water absorption rate is maximum at this frequency), 35 GHz and 94 GHz for air turbulence detection[24], ozone conservation [25];
- planetary defense, where 35 GHz gyrotrons can be used for debris detection radar system [26];
- planetary science, for surface topology map of planets, such as the italian MAGIA project or the Indian Chandryan, with the goal of investigate the soil characteristics of the Moon and Mars [27].

For a further detailed analysis of the possible applications of gyrotrons and their peculiar characteristics toward the specific application see [28].

1.2.3 State of the art for fusion applications

The ITER heating and current drive equipment will also include 24 gyrotrons, each delivering 1 MW. Both Russia and Japan will provide eight gyrotrons each, two will be delivered by India and Europe is in charge of six. This creates a competitive environment which can push forward the development of the gyrotron technology. For this reason, looking at the status of the gyrotron research activity of the different players of the ITER project can give a good point of view on the worldwide status of gyrotrons for fusion applications.

Concerning the Russian gyrotrons, they will be delivered by the IAP RAS/GYCOM partnership. Their design is based on the $TE_{25,10}$ mode of an oversized cavity, allowing the "cooling of the cavity walls in the regime of continuous-wave generation of megawatt power" [29]. They are equipped with depressed collector, a system aimed to recover the unspent electron beam energy, ensuring a total efficiency of the device around 52-53%. In the time window 2016-2020 four gyrotron complexes (including gyrotron, superconducting magnet, matching optical unit, auxiliary power supply, additional magnetic coil and control unit) have been finished, tested and they all satisfied the ITER requirements [29].

All the eight required gyrotrons from Japan have been manufactured together with their auxiliary components. In 2021 four of them achieved the required test criteria (1 MW for 300 s pulse, 50% efficiency, 5kHz modulation with more than 0.8 MW) [30].

The designated manufacturer for the European gyrotrons, for ITER and other European research projects, is the France based company Thales Microwave & Imgaing Sub-system. The present European gyrotrons are designed to operate in Continuous Wave (CW) conditions (up to 1-hour pulse length) and are equipped with a single-stage depressed collector. Different is the case of the european gyrotrons developed for the Tokamak à Configuration Variable (TCV, french for variable configuration tokamak) that will operate in medium pulse (2 s). The TH15007 (for W7X) and TH1509U (for ITER) generate respectively 140 and 170 GHz, 1 MW CW output power at the window. All the THALES gyrotrons are equipped with a "patented beam tunnel and the cavity modes are chosen to reduce mode competition" [31]. A pre-series gyrotron TH1509U for the Divertor Tokamak Test (DTT) facility, with similar characteristics of the ITER ones, is currently under test at the Falcon

facility. The gyrotron has demonstrated 1.02 MW of power at the output window and an efficiency of 40% for five consecutive pulses of 100s [32].

1.3 The issue of the gyrotron cavity cooling and aim of the thesis

The recent trend of research and development of fusion oriented gyrotrons shows an increase in power demand and required tube efficiency, to satisfy the raising request of heating power [33] . In this path, a crucial role is played by the heat sink capability of the cavity cooling system. The cavity is the component where a portion of the electron beam energy is transformed in RF power [10], while eddy currents are induced in the cavity inner wall, with consequent release of huge amount of heat load (Q) on its inner wall. In a gyrotron cavity, the RF electric field is disposed transversally to the direction of propagation of the power and the RF magnetic field has a tangential component that, laying on the cavity surfaces, induces eddy currents on the surfaces. Moreover, a skin effect is present, operating at high frequency, reducing the penetration depth: the current density significantly concentrates on the surface of the cavity inner wall, while drastically reducing moving forward [34]. For these reasons the largest amount of heat load concerns the cavity inner wall and not the volume. The resulting heat flux ($\ddot{Q}$) presents a peaked shape in the axial direction, with peak values of $\sim$25 MW/m^2. In Figure 1.3.a an example of cavity is shown with a normalized profile of heat load, showing the area of the peak. The peaked $\ddot{Q}$ will turn in high temperature peak in the resonant cavity area, causing a cavity thermal expansion. By increasing the cavity dimensions (radius and length), the electromagnetic wave can now travel a longer path within the cavity, hence lowering the frequency at which the cavity resonates. The RF wave's frequency is shifted downward by the inner wall expansion. Depending on the field distribution of the operative mode and the cold frequency (the frequency before reaching the nominal temperature) of the cavity, the interaction efficiency decreases: the cyclotron motion of the electron beam is less synchronized with the RF wave, resulting in a lower amount of net energy transferred from the electron beam to the RF wave. This, in turn, modifies the amount of heat load delivered onto the cavity wall, and so on [35] (see Figure 1.4). More in details, the higher cavity wall temperature leads to a reduction of the electrical conductivity of the material, causing an increase in

the ohmic wall loading. On the other hand, a significant reduction in the produced microwave power, due to a lower QF, can reduces the surface current induced by the RF field in the cavity walls, reducing the ohmic heating. This contribution could compensate the previously mentioned ohmic loading increase linked to the temperature increase. Hence, the multiphysics problem described here, strongly depends on the capabilities of the resonator cooling system and constitutes a major challenge for the development of high power gyro-devices.

Due to the multiphysics characterization of the cavity working principle and its importance for the gyrotron performances, important work of the Work Package HCD of the Eurofusion project [36] had been devoted to the development of a multiphysics tool for the analysis of the resonator itself. The MUlti-physiCs tool for the integrated simulation of the CAvity (MUCCA) [37] was developed, to self-consistently compute the operating conditions of the gyrotron resonator, including all the physics shown in Figure 1.3. It consists of an electro-dynamic (ED) module which, by means of the EURIDICE code (see [38]), models the beam interaction with the electromagnetic field in the cavity, computing the ohmic loading on the cvity wall. This is then used as driver in the thermal-hydraulic (TH) module coupled to the thermo-mechanical (TM) module, which computes the cavity displacements. The resulting deformed inner wall profile and the corresponding temperature profile are fed back to the ED module for the evaluation of the new ohmic loading profile. This tool is currently used for the numerical analysis of gyrotron cavity performance, and in particular how it is affected by the cooling efficiency.

The present European gyrotrons, manufactured by Thales, are cooled with sub-cooled water and use the Raschig Rings (RR), a maccheroni-like porous structure surrounding the cavity external wall for its cooling (see Figure 1.3.b). The RR are named after their inventor, the German chemist Friedrich Raschig, and are mainly used as column packing for distillation and other chemical processes [39]. This configuration exploits the extensive heat exchange surface of the porous media for the heat removal. Design improvement studies have also been conducted on this cooling technology, involving stretching or shrinking of the area equipped with RRs [40]. The outcome has already been implemented in dual frequency TCV Gyrotrons with good performance [41].

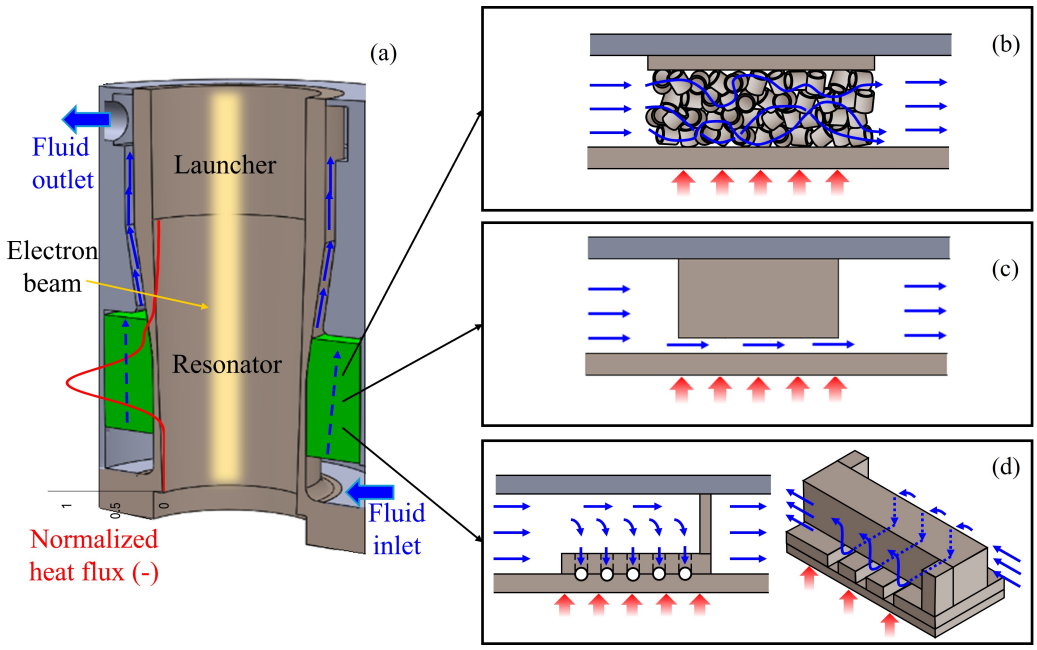

Fig. 1.3 a) Sketch of gyrotron resonant cavity, showing the fluid path and a normalized HL profile, to evidence where the peak is experienced. The green area is devoted to cooling strategies. b) RR cooling strategy, c) longitudinal MCs cooling strategy, d) azimuthal micro-channels cooling strategy. Modified from [42]

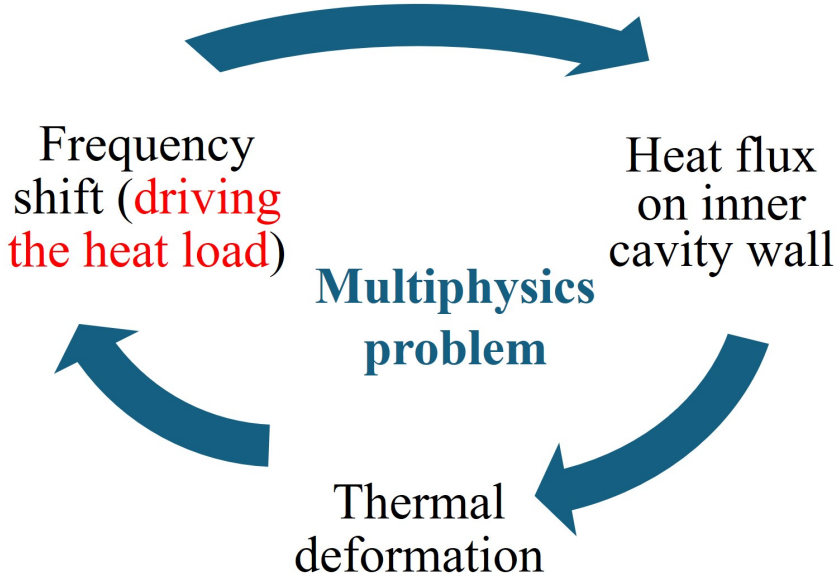

Fig. 1.4 Scheme of the multiphysics cavity cooling problem.

Alternatively, several studies have already been conducted to equip the future European gyrotrons with a cooling system based on mini-channels (MC), drilled along the axial direction of the resonator [43][44] [45] [46] (see Figure 1.3.c), exploiting the high Heat Transfer Coefficient (HTC) of the coolant due to its high speed. A planar mock-up equipped with MC was manufacture by Thales and tested at the Areva premises, with encouraging results [47] and similar design is under consideration for high-power coaxial cavity gyrotrons at Karlsruhe Institut fur Technology (KIT) [48]. Cylindrical cavity mock-up equipped with MC have also been manufactured and tested by Thales for hydraulic measurement and model validation purposes [49] [50], and by KIT for thermal-hydraulic validation [51].

Another cooling option under consideration utilizes micro-channels in the azimuthal direction [46] (see Figure 1.3.d). A design for the W7X gyrotrons has been proposed by the Max Plank institute, showing competitive results in terms of temperature peak and pressure drops with respect to RR. This kind of solutions allow a more homogeneous cooling in the azimuthal direction.

Although all the mentioned configurations are capable of an efficient cooling, sometimes at the expense of the pressure drop, the thermo-mechanical analysis shows high equivalent Von Mises stresses. The computed values of those stresses can, in some gyrotrons configurations, overcome the yield strength of the cavity material (Glidcop), causing the plasticization of the metal. Notice that a plasticized cavity will present a different electrodynamics and, most probably, cooling capability, varying the operating conditions of the gyrotron in the subsequent pulses. The high equivalent stresses are probably due to the large thermal gradients experienced in the radial direction, resulting in outer circumferential fibers tending to expand less than the inner circumferential fibers, creating tensile hoop stress near the inner wall. In addition, the high peaked heat flux axial profile, due to the ohmic losses on the cavity inner wall, can induce a further contribution to the equivalent thermal stresses, due to the different radial thermal gradients in the axial direction. As well the peaked temperature profile will induce a non uniform radial displacements profile, which may negatively affect the shape of the cavity inner wall profile and its QF. Moreover, as already mentioned, to enhance the cooling capability to overcome the displacements and stress problem by increasing the water velocity, will be payed in pressure drop rise.

Summing up all the previous considerations, the need of an optimization study, aiming an efficient cooling system design, is evident. The multi-objective optimization characterizing the cavity cooling problems should account for the minimization of the displacements, directly linked to the frequency down-shift, keep the thermal stresses under the yield strength limit, to avoid plasticization that would irreversibly change the cavity shape, and control the pressure drop.

In the present study different already existing optimization procedure are analyzed and adapted to the cavity cooling problem. The resulting optimized design are compared with the already existing ones, obtained with traditional experienced-based design method. The analyzed optimization procedure and their final results are compared with the aim to establish a general procedure for the design of the cooling system, given a cavity electrodynamics design (with the related heat flux profile).

1.4 Thesis organization

The work presented in this dissertation can be divided in three main branches: design through numerical and optimization methods, experimental and model validation, theoretical analysis. The numerical one constitutes the majority of the work and serves for the design activity carried out on the cavity cooling system. An important part of the research activity was instead devoted to the analysis of experimental data, with active participation in one of the test campaign through the design and construction of the test loop, measurements and results analysis. The experimental results have also been used for the validation of the used numerical models. A minor part of the research presents a more theoretical and analytical characteristic: the stability analysis of an optimized annular cooling configuration. A scheme of the thesis organization is shown in Figure 1.5.

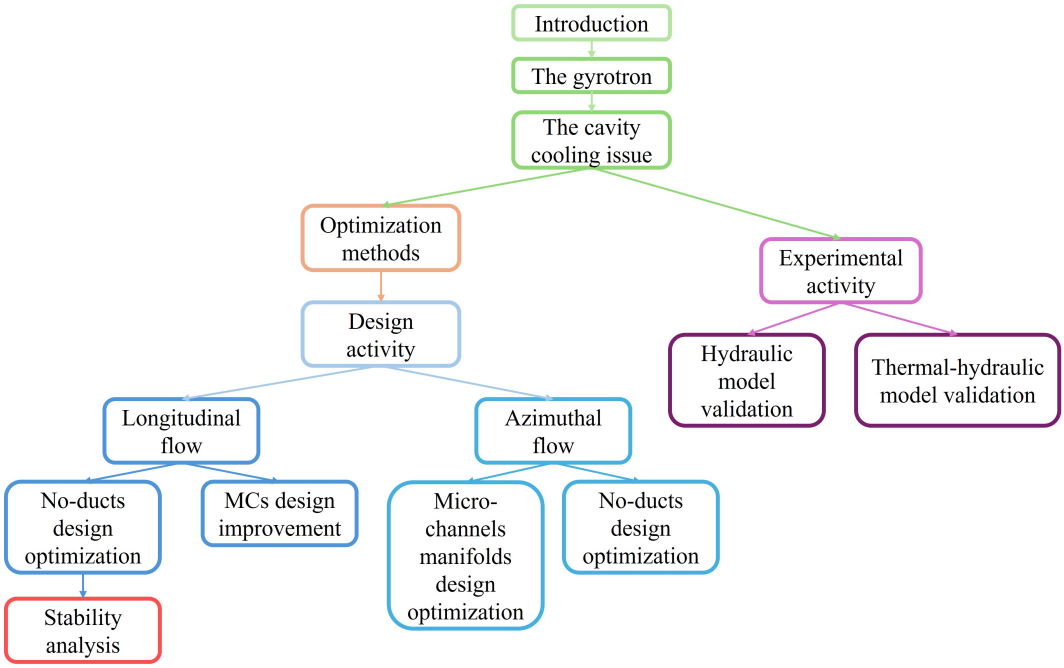

Fig. 1.5 Scheme of the thesis organization.

Chapter 2 is dedicated to a general description of what optimization is and why is useful for design and decision making. Some more details on the theory of two optimization methods used for the work reported in this dissertation are given: adjoint-based topology optimization algorithm and Biogeography-Based Optimization algorithm. An overview of the application of optimization methods to fluid and heat transfer problems is also reported.

Chapter 3 and 4 are dedicated to the design optimization of cooling configurations for the gyrotron cavities, by applying the previously mentioned optimization methods. The activity has been distinguished on the main direction of the coolant in the cooling configurations studied:

- axial main coolant flow direction in Chapter 3
- azimuthal main coolant flow direction in Chapter 4

In Chapter 3, section 3.1 is devoted to the design of a cooling configuration without ducts, showing how an optimized design can be reached using an evolutionary optimization algorithm. Subsection 3.1.3 is instead devoted to the theoretical part of

this thesis, presenting the stability analysis of the previously presented optimized configuration through the development of a 0D analytical model. In section 3.2 the design of a cooling configuration exploiting more ducts or MCs is presented.

In Chapter 4, section 4.1 is devoted to an optimization study considering duct or micro-channels (in the azimuthal direction), exploiting a pure hydraulic model for the definition of the optimization problem, using adjoint-based topology optimization. In section 4.2 the optimization method used is the same, but the problem is faced from a thermal-hydraulic point of view and no ducts are considered in the initial design to be optimized, drawing a parallel path with Chapter 3.

Chapter 5 covers the analysis of experimental results on cavity mock-ups and the model validation. Section 5.1 is addresses the pure hydraulic model validation on a straight MCs mock-up while section 5.2 describes the experimental activity and the measurements and simulation uncertainty quantification carried out on an improved MCs design. Section 5.3 is dedicated to the thermal-hydraulic model validation.

The conclusions and future perspectives of this work are reported in Chapter 6.

Chapter 2

Optimization methods and application to fluid and heat transfer problems

Few decades ago, the design of components and systems was mainly based on experience and correlations. The design chain has been characterized by an initial design, based on experience, the realization of a prototype and its testing, bringing the new knowledge that can be used to a design improvement and a new prototype, until the requirements are satisfied. It consists in an iterative process, that may be expensive in terms of time, due to manufacturing of prototype and multiple iterations, and money, for the material and working hours spent in the prototypes design, production and tests.

Nowadays, thanks to the development of several numerical methods, such as finite volumes, which are the main method for computational fluid dynamics, and finite elements, widely used in structural mechanics analysis, the design process is aided and accelerated by preliminary numerical analysis. The main challenges of today design process are, in fact:

- shortening the design cycle;
- rapidly adapt to the market demands;
- improve the performance (i.e. higher efficiency).

The increasing trend in use of computational tools and the improvement of computational power (allowing more complicate models and to reduce simplifications), help speed up the design process and meet the above listed demands. Experiments remain an important step, to verify the performance of the chosen design and validate the numerical models (used to improve the designs). However, the current new challenge is in the availability of several parameters, contributing to the design, which could be varied and explored: shape, material, manufacturability, cost and so on. The increasing complexity of the task of the design process, leads to the need of new tools to help the decision making process, in which the decision maker navigates among many parameters. While the need of human expertise remains crucial, at least for an initial design, we need to prevent this to became a bottleneck for further design improvements. For this reason, the use of optimization tools and algorithm is increasing, allowing to explore new area of the design space and obtain new design solutions.

2.1 Optimization

Optimization means more than improvement! It is not the process of trying 2/3 or more previously designed possible solutions, starting from a non satisfactory one and choosing the best one among those analyzed. It means "as good as possible" [52].

In mathematics, optimization is the selection of a best element with regard to some criteria from some set of available alternatives. In the simplest case, an optimization problem consists of minimizing (or maximizing) a real function (the objective) by systematically choosing input values for design variables within an allowed set while satisfying all constraints.

2.1.1 Definitions

The general form of an optimization problem is given by the mathematical formulation reported Eq. 2.1, in which f assigns to each value $x_1,...,x_n$ a cost.

$$min(f(x_1,...,x_n)) \; or \; max(f(x_1,...,x_n)) \tag{2.1}$$

- $f(x_1,...,x_n)$ is the objective or cost function;
- $x_1,...,x_n$ are the decision or independent or design variables;
- $x_1,...,x_n \in X$ with X decision set (domain of definition for the independent variables).

The goal is to find the values of the design variables (or independent variables) that minimize or maximize the cost function. The set defines the maximum and minimum values among which the independent variables can vary. This defines an unconstrained optimization problem. A constrained problem, instead, will also include the following conditions:

- $h(x_1,...,x_n) = 0$, equality constraint;
- $g(x_1,...,x_n) \geq 0$, inequality constraint;
- $x_1,...,x_n \in F$ with $F \in X$ constraint set.

In this case the goal is to find the values of the design variables that minimize or maximize the cost function value and satisfy the constraint.

Considering a case of a single design variable, the value x^* that minimize the cost function is called global minimum if $f(x^*) \leq f(x)$ for all $x \in F$ with $x \neq x^*$. $x^* \in F$ is a local minimum if there is a open neighborhood $N \subset F$ of x^* such that $f(x^*) \leq f(x)$ for all $x \in N$ with $x \neq x^*$. $x^* \in F$.

If we are dealing with complex problems, it is not possible to find an analytical solution to the optimization problem. This leads to the necessity of using iterative methods to find the minimum. A general scheme of an iterative optimization method for complex problems is reported in Figure 2.1. The red box contains the analysis model, which allows to compute the value of the cost function, given a value for each design variable of the optimization problem considered. Based on the value of the cost function and, depending on the method, its gradients, the optimizer will suggest new values of the design variables, that could minimize the cost function value.

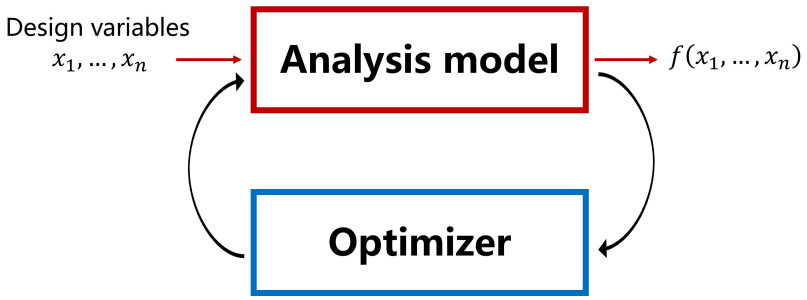

Fig. 2.1 Scheme of optimization iterative process in case of complex problems.

Based on what the optimizer uses to search the new values of the design variables, optimization methods can be classified in zero-order if they only use cost function values, first-order if they use gradients and second-order if they use Hessian matrix. Another possible classification of optimization methods is in the search method, which could be deterministic, characterized by the reproducibility of the result, or stochastic, including randomness in the process.

Optimization methods have been adopted in fluid and heat transfer problems, such as mechanical problems to help design processes. In the following sections two main optimization methods are generally described, to guide the comprehension of the next chapters where they are applied.

2.1.2 Adjoint-based topology optimization in heat transfer-fluid problems

The Adjoint-based Topology Optimization (ATO) method is a gradient-based optimization method based on a transformation of the direct sensitivity approach. In a gradient-based approach the sensitivities help understanding how to change the design variables to minimize the cost function. The direct sensitivity method requiring to solve as many linear sets of equations as the number of design variables, while using the adjoint equations the solution of only one linear system for each cost function is required, independently on the number of design variables. Both methods result in the same values of the final derivatives at the end, but the adjoint one is less computational expensive if only one cost function is present with several design variables. A detailed description of the theory behind this approach is reported in [52].

In the last decades ATO has been applied to optimization problems in several fields such as structural problems [53], fluid dynamics [54] and heat transfer problems [55]. A comprehensive analysis of the state of the art of the application of adjoint methods to fluid-based problems, such as the one at hand, is reported in [56].

The method is used in fluid-dynamics problem with the aim of determining the material distribution χ (solid/clear fluid) within a given computational domain, subject to a pre-set cost function. The optimization process starts from an initial design domain (Ω_d) with a given fluid/solid distribution, solid material is added or removed to find an optimized distribution. In other words it aims to find the optimal material distribution χ (fluid-solid distribution) capable of minimizing or maximizing the cost function. The key feature of this method is freedom: no initial guess is needed and the number of design variables is equal to the number of the cells of the grid. This means that a very high number of solutions is available, to reach the optimal one. In Figure 2.2 an example of a simple optimization problem solved with adjoint-based optimization method is reported. In Figure 2.2.a we can see the initial domain, completely filled by fluid, and the boundary conditions. In order to minimize the cost function, the pressure drop for this case, the optimizer adds solid material, giving at the end of the optimization the optimized material distribution in Figure 2.2.b. The possibility to add solid material is allowed, for this case, only in the square, which constitutes the design space of the optimization problem.

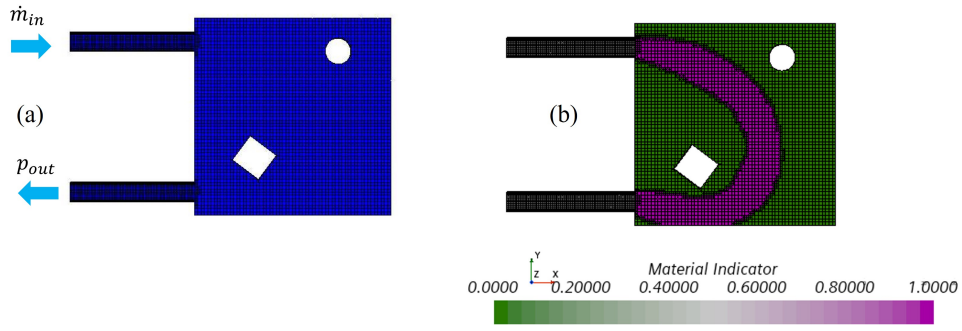

Fig. 2.2 Example of topology optimization in STAR-CCM+. In (a) the computational domain, initially filled by fluid, and e mesh are represented. In (b) the resulting material distribution from the adjoint-based topology optimization, in purple the fluid and in green the solid.

To perform design-aimed topology optimization we need three tools: a model for the design definition, a model for the analysis of the design performances and

an optimizer. As schematized in Figure 2.3 a design model tool is needed to model the design variable $x_1, ..., x_n$ and transform them in the material distribution, which is then used in the analysis model, e.g. the thermal-hydraulic model. This serves for the computation of the value of the cost function J. For adjoint-based methods, the sensitivity of the cost function and constraint are evaluated by using the adjoint method. After that, based on the optimization problem defined (cost function, constraints) a search strategy is used to minimize the cost function, by using the so-computed gradients, to update the material distribution. In the adjoint-based topology case, a gradient based method is used. Going more into the details of the design model, topology mainly utilizes two methods for the modeling of fluid and solid material: the density approach and the level set approach.

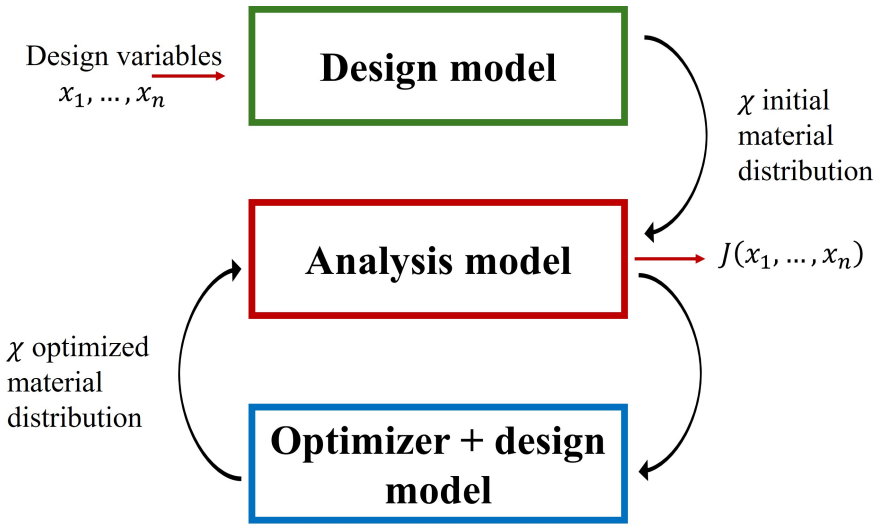

Fig. 2.3 Scheme of the tools needed for design-aimed optimization.

In the density approach, the fluid and solid domain are distinguished by using an impermeability field, α, whose values constitutes a set of design variables and change during the optimization [55]. In other words, a α values is assigned to each discretization element of the design space (i.e. cell). The impermeability field is included in the governing equations through the so-called Brinkman source term [57], which takes non-zero values in solid areas, thus penalizing the flow. In particular α takes on 0 values in the fluid volume and a value of 1 in the solid volume.

In the case of the level set method the interface between fluid and solid material is modeled with a level-set function, based on the distance of each cell of the design

space from the interface itself. For a detailed analysis of the two methods see the review by Sigmund and Maute [58].

2.1.3 Population based algorithm

We may face problems where gradient based methods could not be applied or could not represent the best effective option, hence the need of other methods. An example is optimization problem characterized by cost function which are not differentiable or present discontinuities, or in general when gradients cannot be computed analytically or precisely numerically estimated. Gradient based method may also struggle in finding the global optimum in case of complex, high-dimensional space, due to the large search space. Meta-heuristic methods are strategies designed to deal with complex optimization methods, where traditional exact methods may be infeasible or not efficient. Meta-heuristic methods are strategies used to guide the search process, not based on algebraic models and usually use randomized search techniques. They present the advantage of having wide range of applicability, in discret and continuous problems, and can efficiently explore the search-space in order to find good near-optimal feasible solutions. On the other hand they cannot mathematically guarantee to find the solution, even provide no guarantee of local or global optimality and present a lack of metric of goodness of solution, often stopping the optimization algorithm due to an external time or iteration limit. Tools attempting to solve the previous listed disadvantages can be the incorporation of mechanisms to avoid getting trapped in a confined area of the search space (local minimum), the possible use of memory to better guide the search, to evolve the search process through multiple solutions, giving the name "population based algorithm" to the methods.

Population based algorithms start with the generations of several solutions, the individuals, which constitute the population (N_I). Then a fitness for each individual in the population is evaluated. This gives information on how well the solution satisfies the problem. After that, a subset of the population is selected to create the next generation, based on their fitness, and techniques such as reproduction and variation are used to introduce diversity in the population. Some individual of the initial population are substituted with new individuals of the new population. Then in the next iteration the fitness is evaluated and the stopping criteria checked. The process is repeated until the stopping criteria (maximum iteration, fitness threshold) is satisfied. As mentioned, in population based algorithms, the optimization process

works on several parallel solutions, exploring a large search space. The comparison of the obtained solutions, if converging to similar cost function values, would give a confirmation of the convergence of the optimization problem. This can be compared to what in biology is now called convergent evolution: different species with their independent evolutionary histories, develop analogous adaptations when exposed to similar environmental challenges [59]. An example is the binocular vision in animals [60].

Some examples of population based algorithms are Genetic Algorithm (1975), Particle Swarm Optimization (2005), Biogeography Based Optimization (2008), social network Optimization (2013).

2.2 State of the art of application of optimization algorithms to fluid and heat transfer problems

Optimization methods constitute a vast family of very diverse algorithms. They can, in fact, be classified in several ways, 0/1st/2nd order algorithms (based on the information used for the search direction), deterministic or probabilistic (if they use randomness), global or local (if capable or not to guarantee the finding of the global solution). This diversity gives also different advantages and disadvantages peculiar of each method, which makes the choice of the method a first important step in the decision making process of the optimization design.

In this section, a general review of the application of optimization algorithms to numerical models is given. It is done in particular for fluid and heat transfer problems, being the main fields of application of this thesis. The review can give an idea of what are the most used algorithm in these fields and why and help understand the choice made for this dissertation.

Among the meta-heuristic, population based algorithms, the longest history one and well established is the genetic algorithm (GA). It is based on the theory of natural genetic and natural selection. The first appearance of a GA application as an optimization tool, in fact, dates back to 1967, with the work of Bagley [61] using the expression for the first time, although the first main work is attributed to Holland [62]. Among the main fields of applications we can find electronics [63][64] and telecommunication [65] [66]. Thanks to its long history it can boast numerous other

fields of application such as medicine (in particular disease screening, diagnosis, treatment planning, etc.) [67], software testing [68], image processing [69]. Water management presents many application examples: a review on the optimization of pipeline systems is given in [70] or it is used to design ground-water cleaning system [71]. A review of the application of GA on mechanical engineering is given in [72].

Although its relatively long history, with respect to other evolutionary/population based algorithms, the application of GA to heat transfer is quite new. This is probably due to the high computational cost of heat transfer problems the international community would be interested in optimizing, especially if they are involving CFD. However, thank to the increasing availability of high performance computers, the use of such optimization algorithms in heat transfer problems is increasing in recent years. Talking about heat transfer problems, the main application is design of thermal systems, which is the application of interest of this thesis. Works on the optimization of several kind of thermal systems can be found, such as heat exchangers, heat and fluid networks, heat sinks. In order to apply optimization for a design, as stated before and schematized in Figure 2.1, a model for the analysis is needed, which can span from quite simple algebraic/analytical models to CFD. Some thermal systems for producing, converting and transferring energy, can often be modeled with algebraic equations and correlations, still allowing a high number of design variable, and hence taking advantage of the use of optimization algorithms for their design. An example is heat exchangers (HE), that can be easly modeled with analytical and empirical correlations to find the HE performance. Several studies are available in literature where the minimization of the cost of the HE is the main cost functions considered with different number of design variables. An example is the design of a shell-and-tube HE based on 6 design variables such as tube diameter, tube pitch, number of passes and so on given in [73]. In [74] the case of the shelland-tube HE is optimized with eleven design variables (tube pitch, tube layout pattern, number of tube passes, baffle spacing at the center, baffle spacing at the inlet and outlet, baffle cut, tube-to-baffle diametrical clearance, tube bundle outer diameter, shell diameter and tube outer diameter). The analysis model is constituted by correlations that estimate the HTC and pressure drop. A higher complexity example is given by the optimization of a plate fin HE for two separately analyzed cost functions, the weight and the operation cost, described in [75].The inclusion of constraint in the optimization problems is allowed by the use of artificial neural network, trained on

the first GA population of 500 individuals. Several other examples of other kind of thermal system optimization can be found.

The thermal systems characterized by the highest complexity in the models are usually those cases including fluid-flow, in other words thermofluid systems. The traditional design procedure applied for those kind of systems is the comparison of a small number of experienced based design or a parametric analysis, due to the high computational cost of the analysis model, and it is often labeled as optimization. Nevertheless, the use of actual optimization algorithms for thermofluid system is not forbidden by any fundamental reason if not computational cost and model accuracy, even in case of complex geometries and physics. Despite that, most of the application cases available in literature are still characterized by simple geometries (e.g. single channel) and simple models (2D laminar and steady-state flow). An example is the work of Wildi-Tremblay and Gosselin [76], who optimized a porous layers pile for heat sink purpose. The design variable are the porosity and material composition in each layer. The cost function is the minimization of the hot spot with the implementation of mass and cost constraint through a penalty method in the cost function. The analysis model is a 2D energy equation solved to determine the hot spot temperature, while the velocity profile is know based on algebraic equations. Examples in which CFD is used for the analysis model can be found such as the optimization of the micro-channels heat exchanger reported in [77]. The aspect ratio of the micro-channels is optimized to minimize the pressure drop and the hot spot temperature. An other example is given in [78], where the GA is couple to CFD simulation performed in Fluent. This is done to optimize the geometry of a heat exchanger, to minimize the pressure drop and maximize the heat exchanged.

Other applications of GA in thermal problems can be inverse heat transfer problems, a method mainly used to determine material properties or boundary conditions (BC) (e.g. heat transfer coefficient) starting from measured data such as temperature and heat flux. By formulating the problems as an optimization problems where the error between the measured and predicted values (using the estimated properties or BC). It can as well be used for the fitting and estimation of models parameters. For a complete review on the heat transfer applications of GA see [79].

Another family of optimization method considered here is the topology one, meaning that the method decides where to place solid, creating removing and merging holes in the fluid. It is out of the definition of topology the pure shape optimization,

where only modifications of the fluid-solid interface is possible. This method was firstly introduced in the solid mechanics field [80], but today finds application in many other fields such as fluid and heat transfer. Several applications to fluid-based problems can be found in literature. Alexandersen and Andearsen present in [56] a comprehensive review of this kind of problems, considering fluid-based those problems where at least one governing equation for fluid flow is solved. The seminal work for fluid topology was published in 2003 by Borrvall and Petersson [81]. They set the mathematical basis for topology optimization applied to Stokes flow. the obtained equations presented similarity to the Brinkman-type model of the Darcy law for porous medium flow analysis. Numerous models for the solid material and interfaces representations have been theorized [82], implemented [83] and their limit [84] analyzed a since then. Topology has been developed also for a model using the Lattice Boltzman method (LBM) to approximate the Navier-Stokes [85] and applied to the optimization of a Tesla-type valve design problem [86]. Many application work can be found in the literature in case of flow in laminar regime such as the design of centrifugal pumps without blades [87], the vortex-type passive fluidic diode valves for nuclear applications [88], or topology for rarefied gas problems using LBM [89].

More recently the topology method has been developed and implemented also for turbulent flow, but still in a modest number of publications. This work is still limited to the use of Reynolds-Averaged Navier-Stokes (RANS) equations, using the steady-sate time averaged approximation of turbulence. The first work on topology optimization of turbulent flow, including also the Spalart-Allmaras turbulence model in their analysis of the continuous adjoint sensitivities is given by Kontoleontos et al. [55]. A discrete adjoint approach for the Spalart-Allmaras turbulence model was presented in by Yoon [90]. He also used a κ-ε to design 2D flow components minimizing turbulent energy [91].

Some work has been done also for the application of topology to conjugate heat transfer: when the coupled heat transfer between solid and fluid is considered, together with their temperature field. Concerning heat transfer in forced convection, the first studies are the ones of Dede [92] and Yoon [93]. Dede made use of the commercial software COMSOL to optimize both conduction and conjugate heat transfer [92].Yoon used topology to optimize the design of a heat dissipating structure [93]. In [94] the results of the topology optimization of an active cooling heat sink device was manufactured and tested. The first full conjugate heat transfer model for

density-based topology optimization of turbulent system, where also the temperature field in the solid is modelled, was published by Dilgen et al. [95]. Among the most recent works we can cite the application of a multi-objective density-based method to the design of liquid-cooled eat sinks by Li et al., who presented also numerical and experimental comparison to reference design [96]. The comparison of an optimized microchannel heat sink with a reference straight channel design is given by Hu et al [97].

Chapter 3

Analysis and optimization of cooling techniques with axial flow direction

As already mentioned, the problem of the cavity cooling is characterized by several requirements in different physics fields. The requirements are to minimize the frequency down-shift (which is directly connected to the minimization of the radial displacements), to maintain the level of the stresses below the yield strength of the cavity material, while keeping the pressure drop below 6 bar. To tackle all these requests, the use of optimization methods for the design process is considered in this thesis, to help understanding in particular where the cooling should be enhanced and where is not necessary, in other words to find an optimal spatial distribution of the cooling efficiency, and how to achieve it.

In this chapter the design work done on cooling configurations that exploit mainly the axial flow direction is described.

Section 3.1 is dedicated to a design that does not include the use of ducts. The design work is carried out through an optimization procedure established to particularly face the problem of the cooling of resonant cavities. After the description of the two main steps of the optimization in subsections 3.1.1 and 3.1.2, a stability analysis of the optimized configuration is reported in subsection 3.1.3.

Section 3.2 is devoted to the analysis and design of cooling configurations that, still being characterized by longitudinal main flow direction, exploit ducts or channels. In particular Subsection 3.2.1 describes an improved MCs cooling configuration, currently under test.

Portions of the present chapter were already published in the following scientific papers:

- R. Difonzo, A. Allio, A. Cammi and L. Savoldi, "Biogeography-Based Optimization of the Resonator Cooling in a MW-Class Gyrotron for Fusion Applications". *IEEE Transactions on Plasma Science*, vol. 50 (11), pp 4074-4079, 2022. [98]
- R. Difonzo, A. Cammi, C. Introini, L. Savoldi, "Stability assessment of an optimized cooling configuration of a fusion gyrotron resonant cavity through an analytical model", *Fusion Engineering and DEsign*, vol. 203(3), 2024. [99]

3.1 Design of longitudinal cooling without ducts using optimization

The multiphysics nature problem characterizing the cooling of the cavity requires the use of optimization techniques to guide the design of future cavity cooling systems. In this section, the optimization study characterized by the use of an evolutionary algorithm to find the optimal cooling configuration for the gyrotron cavity and namely the Biogeography-Based Optimization (BBO) algorithm. Here the BBO is applied for the first time to a multi-physics thermo-mechanical problem. Going into the details of our problem, that we want to solve through an optimization procedure, it is important to state that the final aim should be the minimization of the frequency down-shift. The latter is directly linked, with a linear law, to the cavity expansion, hence we will work on the inner wall displacements. As an efficient cooling should minimize the displacements on the inner wall of the cavity as much as possible, the cost function of the cooling optimization problem should be defined targeting the minimum displacement. On the other side, a physical limit is represented by the thermo-mechanical stability of the cavity, depending on the material used. Plasticization must be avoided, hence the stress should not overcome the yield strength of the material at the temperature reached during the operation. The limit on the stress constitutes a constraint for the optimization problem. The novelty of the work is the application of an evolutionary algorithm to a physical problem solved with a best-estimate code instead of a parameter-based or reduced

order model, maintaining the physics of the original problem. The used code for the evaluation of the cost function value consists, in fact, of a thermo-mechanical model with finite elements, allowing the best model-based estimation of displacements and equivalent stresses.

The BBO is an evolutionary algorithm inspired by geographical distribution of organisms and ideated by Dan Simon [100]. Mathematical models of biogeography describe how species migrate from one habitat to another. When a habitat has such characteristics to make it suitable for habitation, it is said to have a high Habitat Suitability Index (HSI) . The logical flow chart of the BBO algorithm is presented in Figure 3.1. The design variables of the general optimization problems constitute a habitat, in the BBO, while all the habitats, or individuals, represent the population of the optimization algorithm. After the values of the design variables, for each habitat, are randomly generated, the HSIs, corresponding to the cost function, are evaluated for each habitat. Based on the value of HSI, emigration rates ξ (the greek letter used in the literature is μ) and immigration rates η (the greek letter used in the literature is λ) are evaluated for each individual of the population and used to modify the population. In the present study a modified BBO is applied, in particular ξ and η are computed with a quadratic model, which resulted as the most promising model in a comparative analysis of different migration models [101]. The new HSIs are evaluated for each habitat after the modification. Since a meta-heuristic optimization method is used, there is the risk to fall into a local minimum. To avoid this, a dedicated technique has been developed, called "cataclysm" [102]. During the process, the number of times the best solution presents the same value of the cost function is counted. If it is more than a pre-set maximum number N_{max}, a cataclysm occurs: only a fixed number of best habitats is kept and all the other are destroyed and newly randomly generated. The number of best habitats kept in the cataclysm is called "elitism". In this work an elitism equal to one is used. The use of cataclysms allows not to get stuck with the same population, which could represent a local minimum. When the maximum number of optimization iterations is reached, the process is stopped and the optimized solution is obtained. For more details on the BBO algorithm see Appendix A.

Since its introduction in 2008 as a benchmark function and sensor for aircraft engines, the BBO has already extended across a number of applications., as reported in [103]. The main applications are the management and economic analysis of power system, parameter estimation and control, scheduling problems, data analysis,

network and antenna problems, and image processing. There are applications in the realm of heat transfer, such as the design optimization of shell-and-tube heat exchanger [104].

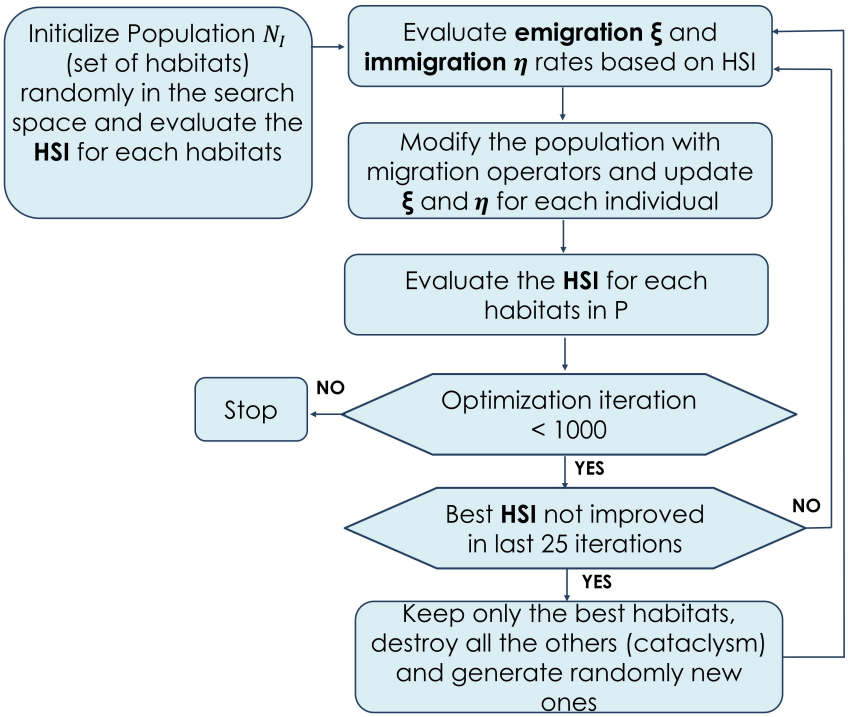

Fig. 3.1 Workflow of the BBO algorithm with cataclysm and specific values adopted in the current work. Modified from [98]

The procedure ideated for the design of the cooling system of the cavity is organized in two main steps. The first step of the analysis for the problem at hand consists of an optimization study which aims to find the optimal profile of the HTC along the axial coordinate of the cavity. The optimal solution should be able to minimize the displacements on the inner wall of the cavity and ensure that no plasticization is experienced, i.e. ensure that the yield strength of the material is not overcame. The optimization work has been carried out by performing thermo-mechanical simulations of the cavity to check the performances of the HTC profile found with the BBO. The second step consists of the design of a simple cooling solution, able to reproduce the optimized HTC profile. The optimized solution is analyzed using a coupled fluid-structure thermal-hydraulic model to evaluate the temperature map. This is used afterwards in a thermo-mechanical model, to demonstrate that the optimized configuration meets the requirements on displacement and limit stress. The

procedure is schematically represented in Figure 3.2. Ultimately, the performance of the designed optimized cooling solution is compared to the performance found in the thermo-mechanical analysis of the solution with the minimized cost function, to validate the procedure.

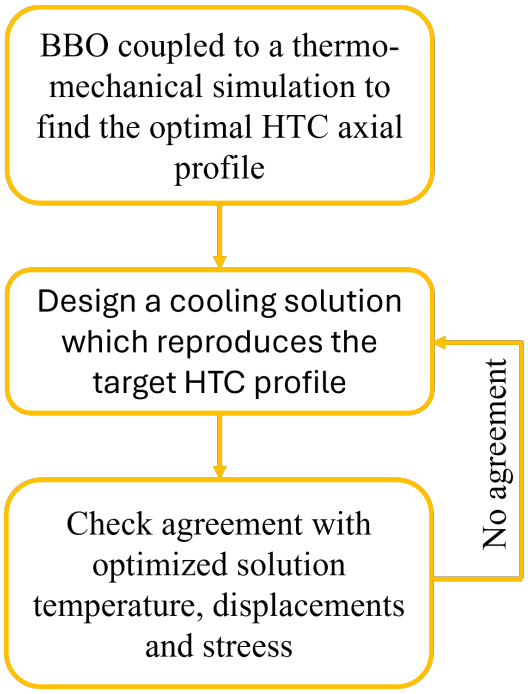

Fig. 3.2 Scheme of the 2-steps procedure used for the optimization and design of the cooling solution. Taken from [98]

3.1.1 First step: optimal profile for the HTC

The aim of the first step of this work was to find the optimal HTC profile along the axial coordinate of the cavity, on the interface between the cavity and the coolant. To do that a thermo-mechanical model has been developed, to evaluate displacements and stresses corresponding to a certain cooling configuration, with a given HTC profile and average fluid bulk temperature, which can be considered as uniform due to an expected negligible variation in the axial direction (as verified in previously studied cavity cooling solutions).

The thermo-mechanical model

The steady-state, thermo-mechanical simulations are performed using a proper module of the commercial software STAR-CCM+, based on the finite elements method. A linear elastic isotropic behaviour of the metal is used as assumption in the model. To reduce the computational cost of the simulations and thus of the optimization process, a slice of 5° ($\pi/36$ rad) of the cavity was cut and used as the computational domain as reported in Figure 3.3, with periodic boundary conditions. The problem is, in fact, axisymmetric, but the utilized software does not allow the use of 2D axisymmetric configurations for finite element analysis. A heat flux profile was imposed on the heated surface of the cavity, corresponding to the red line in Figure 3.3.c. The heat flux profile is obtained using the EURIDICE code, used as ED module in the MUCCA tool, ones the multiphysics analysis reaches the convergence for a cavity equipped with RR. The choice of a converged heat flux profile, even if in the RR cooling configuration, instead of the profile computed with cold cavity (which would be independent from the cooling solution), is dictated by the fact that once converged, the heat flux peak is slightly shifted in the axial coordinate. Being the optimization of the HTC profile on the axial coordinate, this choice goes in the direction of meeting the final heat flux distribution. On the fluid-solid interface, represented in Figure 3.3.b with the blue line, a convective boundary condition was imposed with an HTC profile varying with the axial coordinate (see Figure 3.3.a).

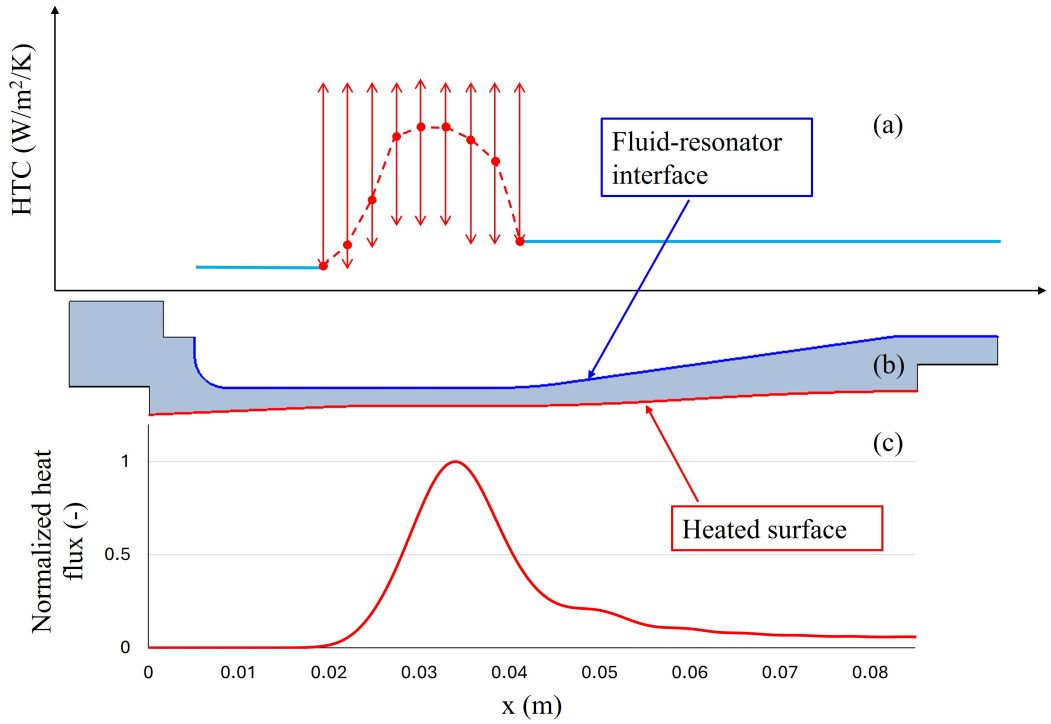

Fig. 3.3 Axial view of the computational domain of the finite elements simulation, with thermal boundary conditions: a) the heat transfer coefficient axial profile is represented; b) heated surface (red line), where the heat flux is applied, and solid-fluid interface of the convective BC (blue line). In c) normalized heat load profile.

The optimization problem

In the current optimization problem the design variables are constituted by the different values of the HTC along the axial coordinate, in the area of the heat flux peak. In that area, 9 points of unknown HTC were chosen, and lower and upper values were imposed: the HTC there could vary between the lower and upper value. The upper bounds have been chosen considering the eventual possibility to manufacture an engineering solution that could reproduce those high values of HTC. In particular, the maximum values obtained in numerical simulations with MCs have been taken as a reference. The lower bounds for the central design variables are slighlty higher than the fixed values at the extremes of the axial coordinate range of the design variables (see Figure 3.3.a), in order to reduce the search space and hence the computational cost of the optimization, since high value of HTC were expected to be found in the central points through the optimization procedure. The rest of

the HTC profile was characterized by constant values, taken from a simulation of a cavity cooled with a mini-channels system [10].

The cost function J of the optimization problem was initially defined with the aim of minimizing of the radial displacements (in μm) on the inner wall. Where the heat flux is higher, the displacement has a larger weight, as shown in equation 3.1.

$$J = \frac{\int_{x_1}^{x_2} disp(x) * \ddot{Q}(x)dx}{\int_{x_1}^{x_2} \ddot{Q}(x)dx} \tag{3.1}$$

where $disp$ is the computed radial displacement on the heated surface, $\ddot{Q}$ is the heat load and x is the axial coordinate.

As mentioned before, it is crucial to design a cooling configuration capable of preventing plasticization. To do that, a constraint in the optimization problem is needed on the maximum stress that should be lower than the yield strength of the material, at the computed temperature. The constraint is defined using the temperature-yield strength curve of the glidcop, with a safety range of 20 MPa (as reported in figure Figure 3.8), on the heated surface. As reported in equation 3.2, the difference between the yield strength ($\sigma_{yieldStrength}$), at the computed temperature of the location where the maximum equivalent Von Mises stress is found, and the computed maximum equivalent Von Mises stress (σ_{max}), in accordance to the Von Mises yield criterion, augmented by a safety term, is evaluated. If this difference is positive, the constraint is satisfied. Notice that this is in accordance with the above mentioned use of a linear elastic model for the material law: the stresses calculation is not affected by error due to plasticization since solutions overcoming the yield strength will be "discarded" thanks to the included constrained.

$$\Delta\sigma = \sigma_{yieldStrength}(T(\sigma_{max})) - \sigma_{max} - \Delta\sigma_{safety} \tag{3.2}$$

If this difference is positive, the constraint is satisfied. If it is negative, the constraint is not satisfied. To be included in the optimization problem, the value of $\Delta\sigma$ is added in the cost function when the constraint is not satisfied, obtaining an augmented cost function $J^{'}$ as reported in equation 3.3, with a penalty factor ψ. It is, in fact, not trivial, to directly discard solutions not meeting the constraint, because it would reduce the population size during the optimization iteration, while the use of an augmented cost function, with the proper tuning of the penalty factor, ensures the

satisfaction of the constraint while keeping constant the population size. The value of the penalty parameter ψ is determined in order to have $\psi * (-\Delta\sigma)$ of the same order of magnitude of J. A representative case has been preliminary considered: the displacement was of the order of 40 μm while $\Delta\sigma$ was of the order of $30 * 10^6$ Pa. A value of $\psi = 1.33 * 10^{-6}$ was thus obtained and kept frozen for all optimization simulations. In this way, solutions meeting the constraint turn out to be better than solutions not meeting the constraint but with lower J.

$$J^{'} = J + \psi * (-\Delta\sigma) \tag{3.3}$$

Being the optimization problem defined in the thermo-mechanical field, no direct control on the fluid velocity and hence on the pressure drop could be included a priori. This means that consideration on the pressure drop and other issues correlated to the coolant velocity, such as the material corrosion, should be done a posteriori in the decision making process.

Optimization results

In Figure 3.4.a and b the evolution of five minimum values of the cost function J (HSI in BBO) along the optimization iterations is reported for two cases of population size N_I, or number of individuals. In both cases we can notice how the chosen number of maximum iteration gives a converged solution, observing that the minimum values of the cost function abruptly reduce in the first 200 iterations while a slower reduction tending to the same value is observed in the following 800 iterations. A zoom in a reduced range of cost function values is reported in Figure 3.4.c and .d for the two cases of N_I considered, showing how a larger population size ensures a faster convergence: after 700 iterations a convergence can be observed for the $N_I = 40$ case. Moreover, in the latter case, the curves of the different trials show closer values, resulting in a higher reliability of the solution. These considerations are confirmed by the evolution of global quantities, specifically the average minimum cost value and its standard deviation, represented respectively in Figure 3.5.a and .b. The red dashed lines of Figure 3.5.a shows, in fact, a faster convergence, while the standard deviation for the case with $N_I = 40$ in Figure 3.5.b shows lower values, confirming the lower dispersion of the results in case of bigger population size. Another important parameter to be observed during the optimization procedure is the

$\Delta\sigma$ defined in Eq. 3.2, included in the augmented cost function to account for the constraint on the maximum equivalent stress. Its evolution along the optimization iterations is reported for the two cases considered of population size in Figure 3.6.a and .b. For both cases it can be notice that its values goes to zero in the first 200 iterations and remains sable until the end of the optimization process, confirming the robust definition of the constraint in the optimization problem definition.

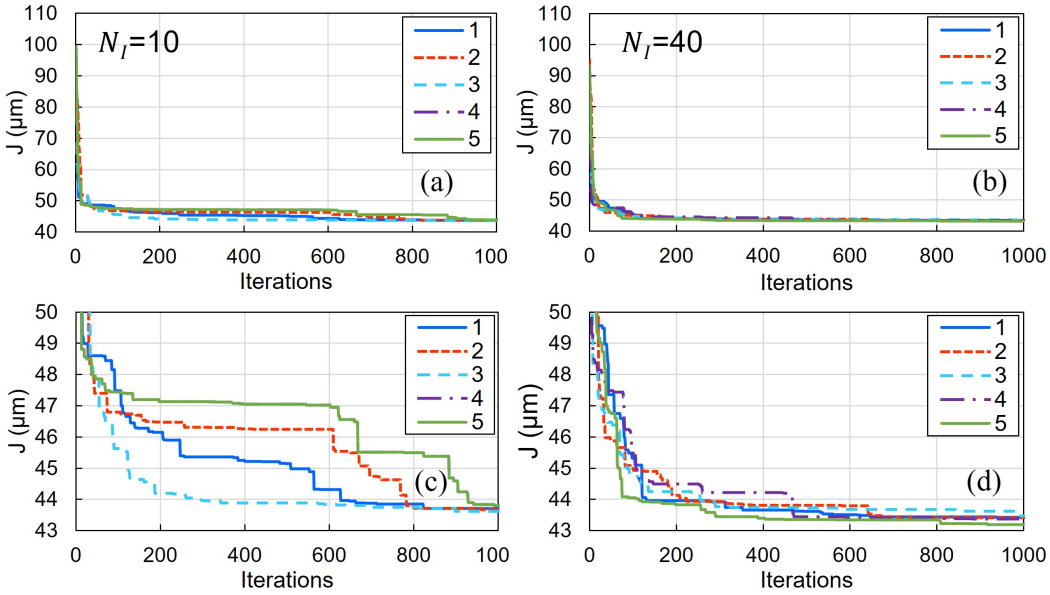

Fig. 3.4 Cost function evolution along the optimization iteration for a population size N_I equal to a) 10 and b)40. c) and d) report a zoom on a reduced range values of the cost function evolution for the two cases.

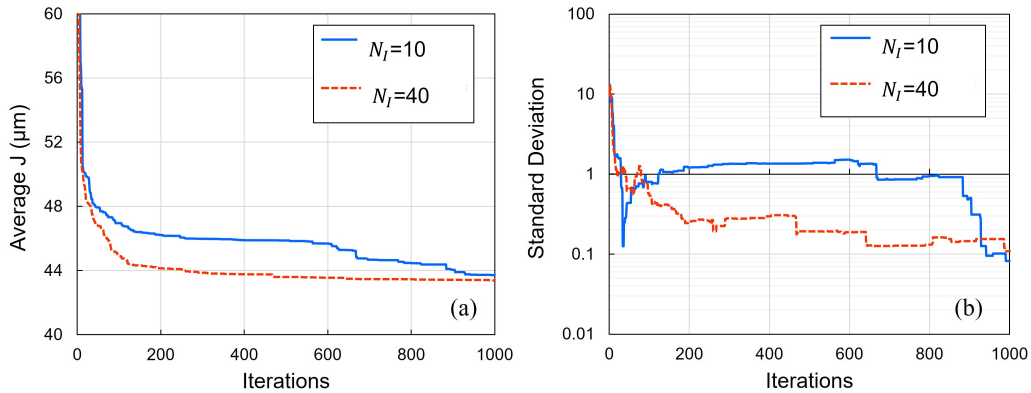

Fig. 3.5 a) Average minimum cost and b) standard deviation along the optimization iterations.

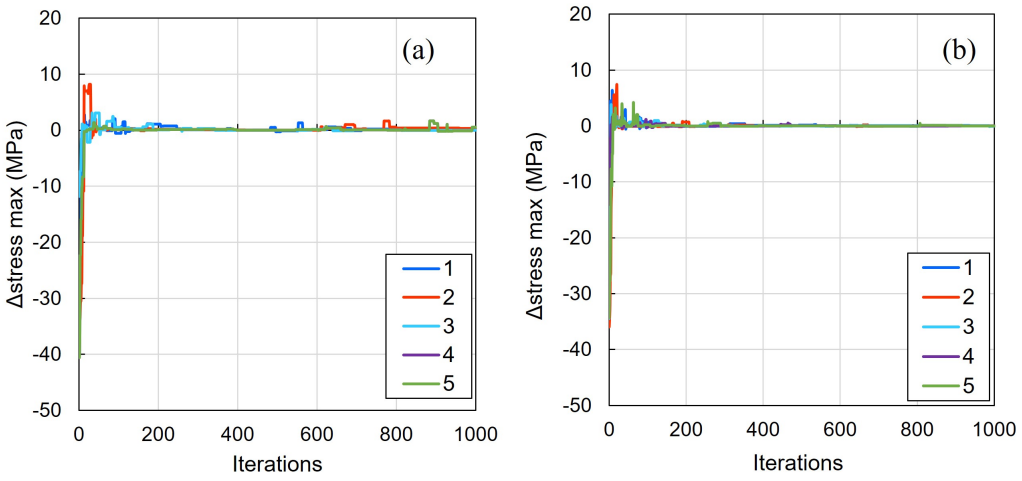

Fig. 3.6 $\Delta\sigma$ evolution along the optimization iteration for a population size N_I equal to a) 10 and b)40.

Among the obtained optimized results, the one presenting the lowest cost function was chosen. An optimized HTC profile was obtained as a result of the optimization process (see Figure 3.7). In the area of the heat load peak, the optimization leads to the highest HTC allowed in the defined range to reduce as much as possible the displacements. On the other side, at the other axial coordinates, lower values of HTC are found. This effect can be understood since a temperature profile as flat as possible is needed to reduce the stresses that could be caused by axial temperature difference. The solution respects the constraint on the stress limit, avoiding plasticization, as confirmed by Figure 3.8, where all the stress computed along the heated surface, in green, are below the limit stress at that temperature. The limit stress, the red curve, is defined as the yield strength decreased by the safety term of 20 MPa. This demonstrates that the addition of a penalty on the cost function worked as expected, confirming the appropriate setting of the constraint in the optimization algorithm. The radial displacements on the inner wall, resulting from the evolutionary optimization algorithm, are represented in Figure 3.9. As expected, the maximum value is observed near the peak, where the maximum HTC is also chosen by the algorithm.

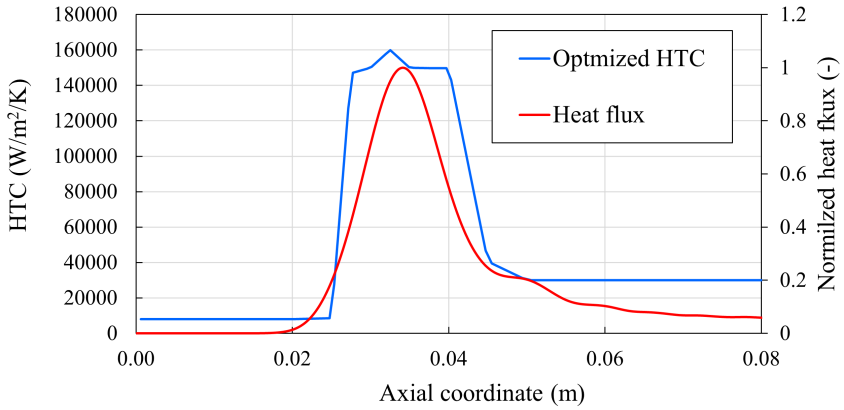

Fig. 3.7 Optimized axial profile of the HTC and normalized heat load

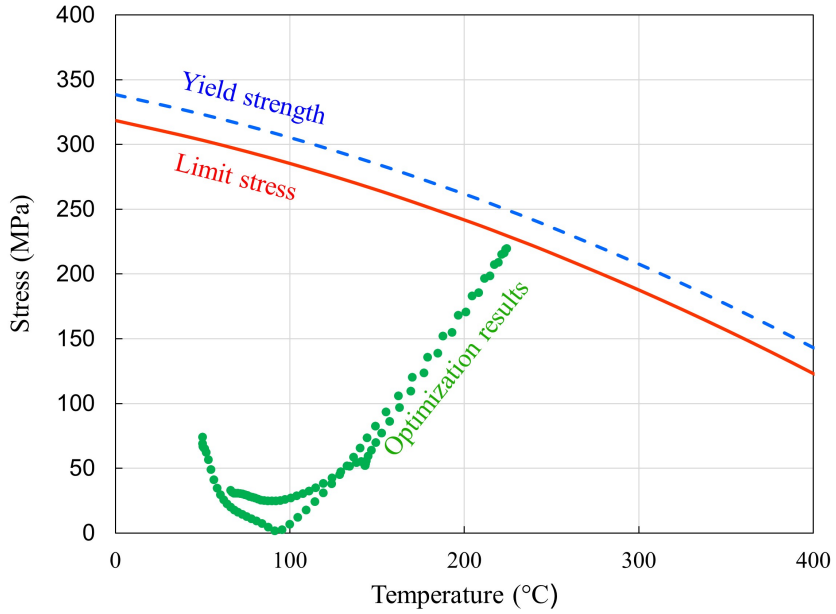

Fig. 3.8 In blue the yield strength curve of the Glidcop with respect to temperature. In red the yield strength curve decreased by the safety term of 20 MPas. In green the stress and temperature along the heat surface. Taken from [98]

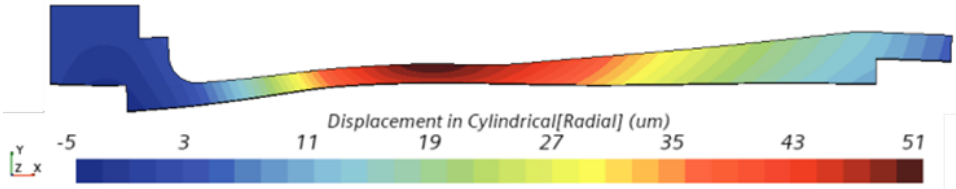

Fig. 3.9 Radial displacements of the optimized solution on a cavity section. Taken from [98]

Few sensitivity analyses have been performed to assess the robustness of the computed results. Because of the low values of the heat flux in the upstream area, the optimization results do not change if the optimization domain is extended leftward in Figure 3.3. On the contrary, enlarging the optimization domain in the right-side direction, the displacements in that region could be still reduced, but their relevance for the overall cavity performance is small, in view of the low values of stresses observed in that area (see also below). On the other side, the results obtained in the considered optimization domain, hence in the heat flux peak area, do not change expanding the lower-upper range of the HTC optimization.

3.1.2 Second step: design a cooling configuration for the desired HTC profile

Once the optimal HTC profile has been found, the second step for the analysis (Figure 3.2) has been to design a simple cooling solution able to reproduce that profile. The simplest possible cooling solution for the water flow has been identified as an annular region surrounding the cavity (see Figure 3.10), with a variable thickness ($thick_f$) along the axial coordinates. The fluid enters the cooling system with a temperature of 30° and a flow rate of 0.7 l/min corresponding to 50 l/min of total flow rate for the entire circular cavity. For the evaluation of the thickness of the annular region, the geometry has been approximated to a flat plate, since the thickness is much smaller than the radius of the cavity. The Dittus-Boelter correlation (equation 3.4) has been used to evaluate the necessary $thick_f$ to obtain the desired HTC.

$$Nu_{DB} = 0.023 Re^{0.8} Pr^{0.4} \tag{3.4}$$

where Re is the Reynolds number (defined using $thick_f$ as the characteristic length) and Pr is the Prandtl number.

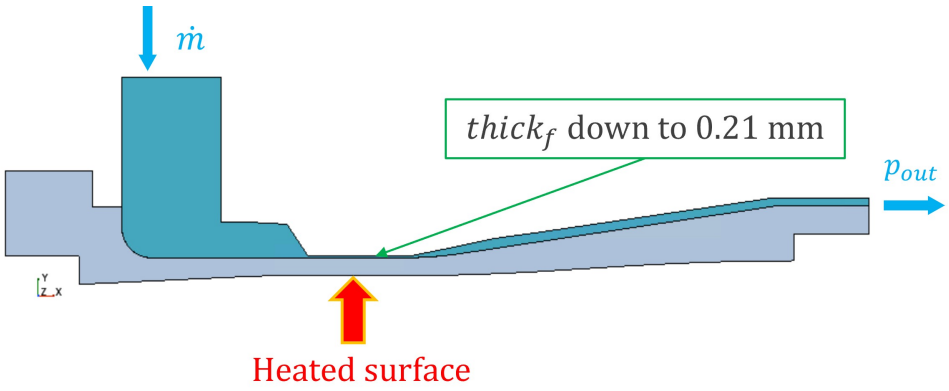

Fig. 3.10 Annular cooling configuration reproducing the optimized HTC axial profile. Modified from [98].

The performance of the cooling solution has been checked with a 3D, axisymmetric, steady state, conjugate heat transfer fluid-solid coupled model, with Lag EB $\kappa - \varepsilon$ turbulence model [50], considering the same portion of domain used in the thermo-mechanical model coupled with the BBO. The temperature map obtained from the CFD analysis has been then used in a thermo-mechanical 3D, axisymmetric, steady state model, to evaluate the displacements and the stresses of the cooling solution. Note that this procedure is well consolidated in the multi-physical analysis of gyrotron cavities [37].

The performance of the designed annular cooling solution has been compared to the results of the optimization analysis. Temperature, radial displacements and stress profiles on the inner wall are reported in Figure 3.11, Figure 3.12 and Figure 3.13, respectively. All the results show a good agreement between the two solutions, demonstrating the robustness of the procedure. Concerning the temperature profile in Figure 3.11, the CFD results of the annular solution slightly differ from the BBO results (obtained with convective BC in TM model) around the axial coordinate of 0.04 m (close to the end of the optimization region in Figure 3.7, which spanned from 0.02-0.045 m), where the abrupt increase of the $thick_f$ occurs. The impinging-jet effect of the water arriving form the narrow channel leads, in fact, the lower temperature observed with the CFD. This corresponds to lower displacements in Figure 3.12 in that area, driven by the lower temperature. Also, the computed stress presents lower values in the annular configuration, with respect to that resulting ones from the optimization. As we can notice from Figure 3.12, a maximum of $\sim 45\ \mu m$ of radial displacement on the heated surface is computed in the area of the heat load

peak, where $thick_f$ is $\sim 200\ \mu m$. This needs further analysis because the highest displacement on the solid-fluid interface is also expected there, inducing a different cooling configuration. This could possibly introduce instability problems that are discussed in section 3.1.3.

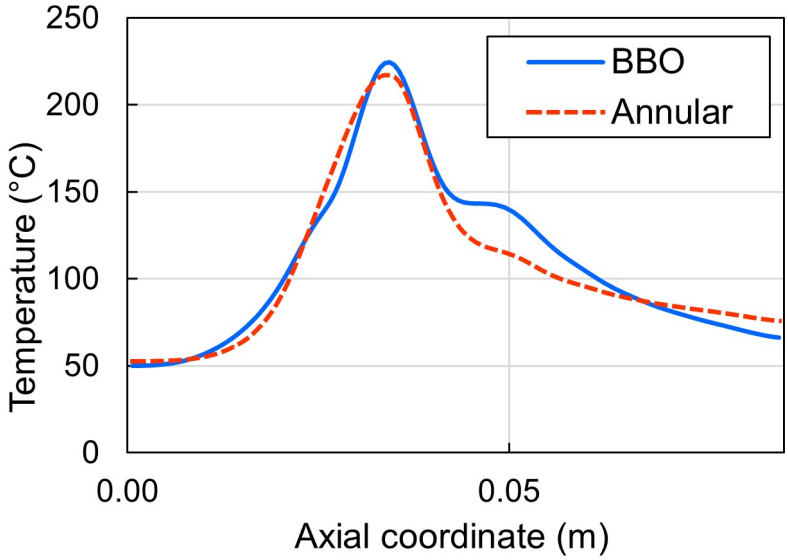

Fig. 3.11 Temperature profiles obtained with the optimization and the designed annular cooling solution. Taken from [98]

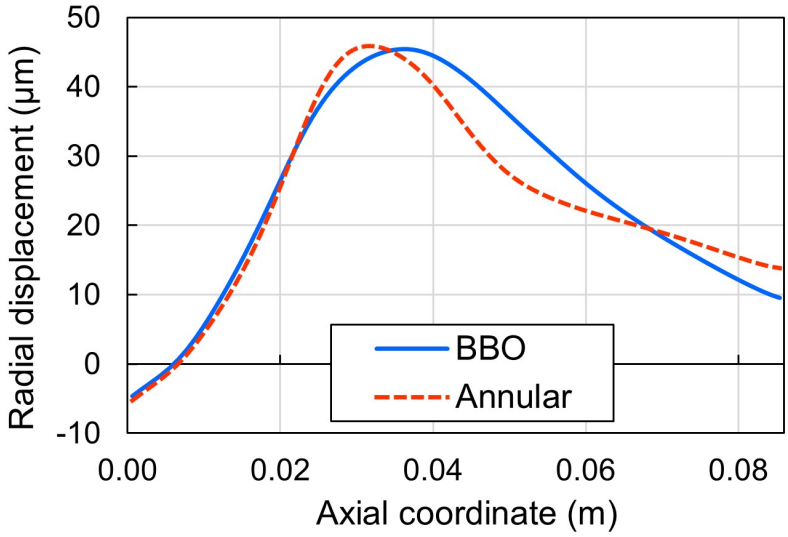

Fig. 3.12 Radial displacements profiles obtained with the optimization and the designed annular cooling solution. Taken from [98]

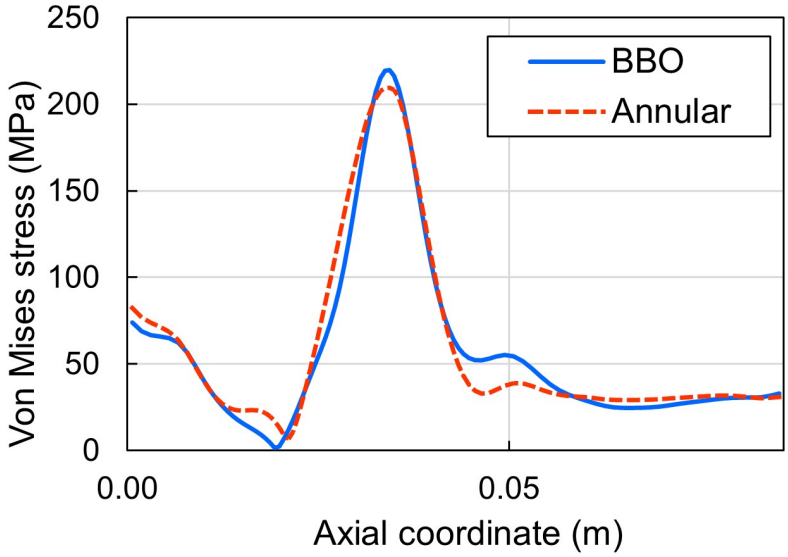

Fig. 3.13 Stress profiles obtained with the optimization and the designed annular cooling solution. Taken from [98]

Comparison with RR cooling solution

The European Gyrotron cavities are currently equipped with a RR cooling system. A comparison of the performance of the cooling solution designed in the present chapter and the RR solution has been performed using CFD fluid-solid coupled model and subsequently a TM finite element mode using the CFD obtained temperature map. The two cooling solutions are applied on the same cavity geometry, with the same heat flux profile and same water flow rate. In Figure 3.14, the computed temperature profiles of the two cooling solutions are reported for the sake of comparison. The configuration designed in this chapter presents a much lower maximum temperature than the RR one, resulting consequently in smaller maximum radial displacement, as shown in Figure 3.15. This is due to the high HTC reached with this configuration, as obtained in the BBO optimization. Note, however, that the optimization algorithm tends to take the upper bound of the HTC in the maximum position. A reduction of the HTC upper bound would have resulted in a larger temperature and displacement in the optimized solution. On the other side, in the optimized cooling solution also stresses are lower, as it is shown in Figure 3.16. This is the remarkable point of the procedure, which allows to have high-efficiency cooling solution, while satisfying

the constraint on the yield strength, which is an important physical limit for the RR solution.

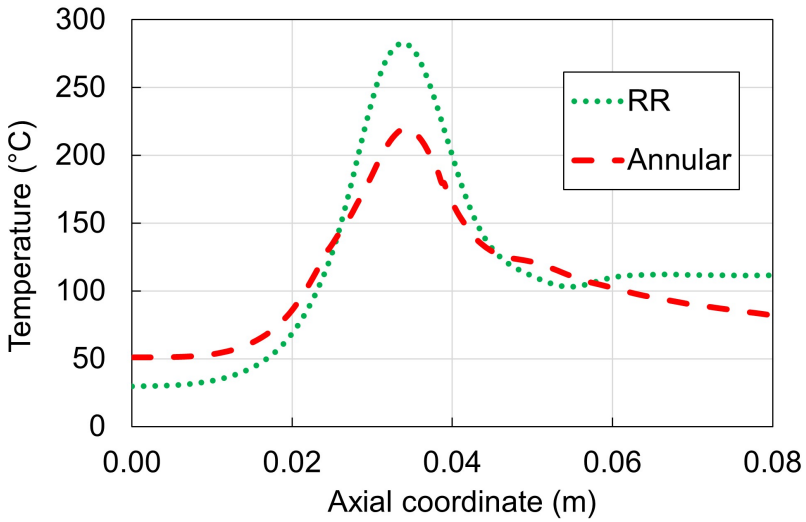

Fig. 3.14 Temperature profiles obtained with CFD of the optimized annular cooling and with RR. Modified from [98]

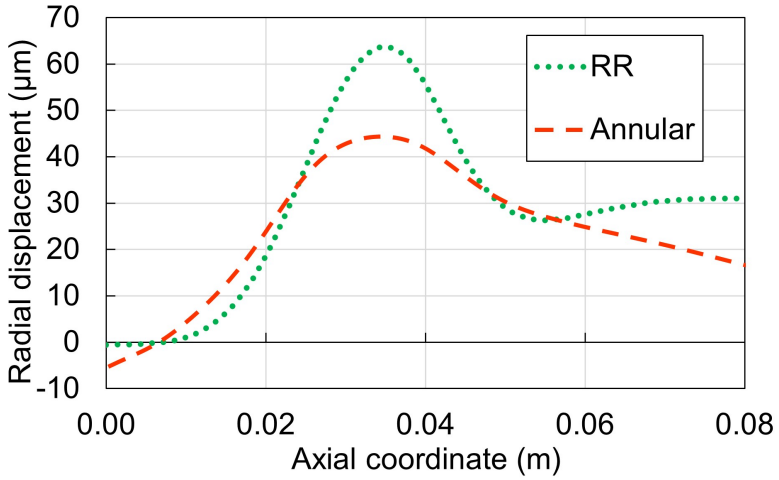

Fig. 3.15 Temperature profiles obtained with TM finite elements model, using the CFD obtained temperature map, of the optimized annular cooling and with RR. Modified from [98]

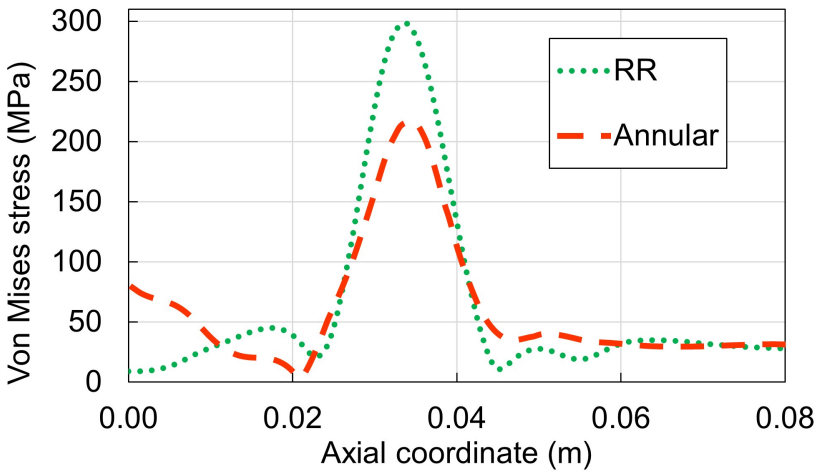

Fig. 3.16 Temperature profiles obtained with TM finite elements model, using the CFD obtained temperature map, of the optimized annular cooling and with RR. Modified from [98]

3.1.3 Stability analysis

The optimized design of the annulus configuration presents promising results, but, apart from the manufacturability of such a thin annulus, the very small thickness could present some instabilities, being only one order of magnitude bigger than the evaluated radial displacements. During the normal operation of gyrotrons, in fact, variations in power are expected, with variation in the heat load released on the inner wall of the cavity. This might lead to perturbation in the cooling capability of the system, because of deformation in the geometry, due to the high temperature. A preliminary prediction of the qualitative phenomena described is represented in Figure 3.17. The dependence of the product of the heat transfer coefficient HTC and the heat transfer surface A_s with respect to the internal diameter D_i is plotted. We can notice as, increasing D_i, the product also increases, with a general positive effect on the heat transfer of the system. The point corresponding to the present study is represented with the circle in the figure. The range of variation of D_i is limited by the dimension of the external diameter D_o in Figure 3.18. The diameter expansion can also be assimilated to a condition in which an impurity could reduce the flow passage thickness. Here the problem of the stability is addressed from a time-dependent point of view, by verifying the stability of the system and its response to perturbations in time.

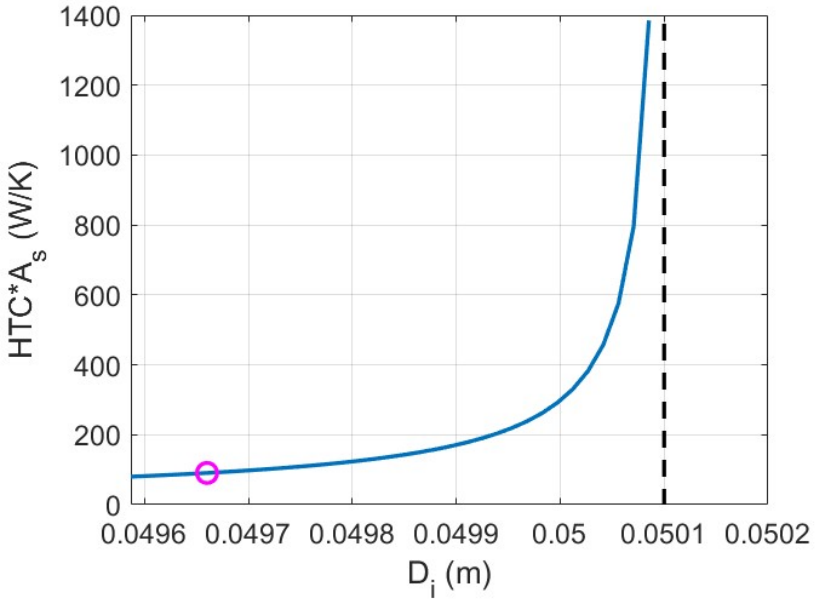

Fig. 3.17 Evolution of the product of the heat transfer coefficient h and the heat transfer surface A_s varying the internal diameter D_i. In black the value of the external diameter D_o. Modified from [99].

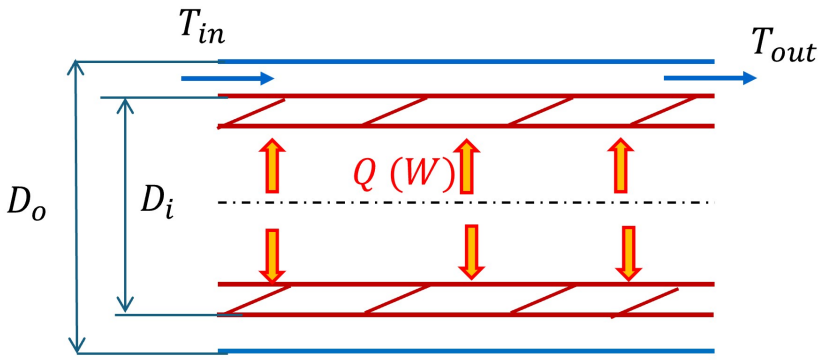

Fig. 3.18 Annular geometry under investigation in the present work. Modified from [99].

Methodology

The initial approach to the stability problem begins with a linear system to exploit Lyapunov's criterion [105]. The Lyapunov's criterion states that, given a system of equations, if and only if all the eigenvalues of the associated matrix of coefficients have negative real part, the internal stability of the system is verified. In other words,

if all eigenvalues of the matrix are in the left-half plane of the complex plane, the system is asymptotically stable [105]. After completing the linear stability analysis, which involves linearizing the system and examining its eigenvalues, the study of the nonlinear system is addressed. The time-varying transient is analyzed to validate whether the stability predictions, based on a linearized model (which is only valid for small input perturbations) are corroborated by the nonlinear transients.

The mathematical model and its linearization

To investigate and verify the stability of the critical portion of the annular cooling system, i.e. that characterized by the very small thickness. A lumped 0D model is purposely developed, assuming the same temperature in the entire fluid volume and the same temperature in the entire metal volume. The modeled annular geometry is represented in Figure 3.18. The red part represents the metal (Glidcop in the case of the European gyrotron cavities), while the blue part represents the coolant (subcooled water in this case). The quantity D_i is the internal diameter of the fluid annulus, corresponding to the external diameter of the cavity in the analyzed region, while D_o is the external diameter of the fluid annulus, and has been determined as an average value of the longitudinally varying diameter shown in Figure 3.10. The heat load Q released on the cavity inner wall is evaluated as a surface integral of the heat flux ($\ddot{Q}$) profile on the analyzed portion of the cavity, where the heat flux peak is located. T_{in} and T_{out} are the inlet and outlet water temperatures respectively.

The energy conservation laws describing the system simplify to Eq. 3.5 for the metal with average temperature T_m and Eq. 3.6 for the coolant with average temperature T_c, respectively:

$$M_m C_m \frac{dT_m}{dt} = Q - HTC \times A_s (T_m - T_c) \tag{3.5}$$

$$M_c C_c \frac{dT_c}{dt} = HTC \times A_s (T_m - T_c) - \dot{m} C_c (T_{out} - T_{in}) \tag{3.6}$$

where M_m, C_m and T_m are the mass, the massive heat capacity and the average temperature of the metal, while M_c,C_c and T_c are the mass, the massive heat capacity and the average temperature of the fluid. A_s is the heat transfer surface and $\dot{m}$ the

Table 3.1 Values of the 0D model parameters

M_m	kg	1.38
C_m	J/kg/K	394
M_c	kg	4×10^{-4}
C_c	J/kg/K	1486
$\dot{m}$	kg/s	0.83

mass flow rate. The values of the prameters included in the model are reported in 3.1.

Assuming the coolant temperature $T_c = \frac{T_{in}+T_{out}}{2}$ and rewriting the equations introducing a small perturbation for all the variables we obtain Eq. 3.7 for the metal and Eq. 3.8 for the fluid.

$$M_m C_m \frac{d\delta T_m}{dt} = \delta Q - \delta(HTC \times A_s)(T_m - T_c) - HTC \times A_s \delta(T_m - T_c) \tag{3.7}$$

$$M_c C_c \frac{d\delta T_c}{dt} = \delta(HTC \times A_s)(T_m - T_c) + HTC \times A_s \delta(T_m - T_c) - \dot{m} C_c \delta(2T_c - 2T_{in}) \tag{3.8}$$

By analyzing an annular geometry, the hydraulic diameter is evaluated as $D_{hy} = D_o - D_i$ while the heated diameter as $D_{he} = (D_o^2 - D_i^2)/D_i$ [106]. This choise is due to the fact that the analyzed configuration is one-side heated. The Dittus-Boelter correlation is introduced in the equations, under the assumption that it will well represent the problem at hand given the configuration differences from the one used to retrieve the correlation, so that the product of HTC and heat transfer surface gives 3.9:

$$\begin{aligned} HTC \times A_s &= 0.023 k^{0.7} c_p^{0.3} \mu^{-0.5} * (4\dot{m})^{0.8} \pi^{0.2} L * \frac{D_i^2}{(D_o + D_i)^{\frac{9}{5}}(D_o - D_i)} \\ &= \Psi' \frac{D_i^2}{(D_o + D_i)^{\frac{9}{5}}(D_o - D_i)} \end{aligned} \tag{3.9}$$

Now the small variation of the product of the HTC and the heat transfer surface is computed by introducing the linear thermal expansion law (Eq. 3.10) in Eq. 3.9, giving Eq. 3.11. A comprehensive computation of the total deformation should include also the stress-induced mechanical deformation and combine it with the thermal one. Given the aim of this analysis, aiming to investigate the dynamic correlation between the thermal expansion and the cooling system functioning, and being the elastic deformation negligible with respect to the thermal one, it is not accounted in this preliminary analysis.

$$\delta D = \lambda D_0 \delta T_m \tag{3.10}$$

$$\begin{aligned}\delta(HTC \times A_s) = \Psi' \lambda D_i \left(\frac{2D_i^2}{(D_o+D_i)^{1.8}(D_o-D_i)} + \frac{-1.8D_i^2}{(D_o+D_i)^{2.8}(D_o-D_i)} + \right. \\ \left. + \frac{D_i^2}{(D_o+D_i)^{1.8}(D_o-D_i)^2}\right)\delta T_m = \Psi \delta T_m\end{aligned} \tag{3.11}$$

In Eq. 3.10, λ is the linear thermal expansion coefficient of the Glidcop. Notice that, introducing the thermal expansion law, the dependence on the diameter is removed, and the two equations will depend only on δT_m and δT_c. We want, in fact, to represent the analyzed problem in the state-plane, in the general form of Eq. 3.12, where $\mathscr{X}$ is the state and $\mathscr{U}$ the inputs. The final set of perturbed equations is reported in Eq. 3.13 in the compact form. More in details, T_m and T_c are the state variables of our problem and Q and T_i are the inputs. The introduction of small perturbations for both state variables and inputs in Eq. 3.7-3.8 allowed us to linearize the problem with the further implementation of the linear expansion law for the diameter.

$$\dot{\mathscr{X}} = \mathscr{A}\mathscr{X} + \mathscr{U} \tag{3.12}$$

$$\frac{d}{dt}\begin{bmatrix}\delta T_m \\ \delta T_c\end{bmatrix} = \mathscr{A}\begin{bmatrix}\delta T_m \\ \delta T_c\end{bmatrix} + \mathscr{B}\begin{bmatrix}\delta Q \\ \delta T_{in}\end{bmatrix} \tag{3.13}$$

In Eq. 3.13, $\mathscr{A}$ is the matrix of the coefficients for which the eigenvalues are evaluated, to verify the internal stability of the system and is reported in Eq. 3.14, while the coefficient of the matrix $\mathscr{B}$ are reported in Eq. 3.15.

$$\mathscr{A} = \begin{bmatrix} \frac{-\Psi T_m^0 - HTC \times A_s + \Psi T_c^0}{M_m C_m} & \frac{HTC \times A_s}{M_m C_m} \\ \frac{\Psi T_m^0 + HTC \times A_s - \Psi T_c^0}{M_c C_c} & -\frac{HTC \times A_s}{M_c C_c} - \frac{2\dot{m}}{M_c} \end{bmatrix} \tag{3.14}$$

$$\mathscr{B} = \begin{bmatrix} \frac{1}{M_m C_m} & 0 \\ 0 & \frac{2\dot{m}}{M_c} \end{bmatrix} \tag{3.15}$$

At this stage, the step response of the system is computed, perturbing one of the inputs while keeping constant the other one. First the fluid inlet temperature T_{in} is perturbed of 1 $^{\circ}C$ and the input power Q is constant, then Q is perturbed of 1 kW and T_{in} kept constant. This is done also for the non-linear system, that is solved in MATLAB using the ode15s solver. The perturbation of the model inputs, and of Q in particular, represents the general phenomena that can actually occur during the normal operation of the gyrotron, as described in the introduction.

Results

The eigenvalues of the matrix $\mathscr{A}$ are represented in the Gauss plane in Figure 3.19. Both eigenvalues found have negative real part, falling in the left side of the complex plane representation. This means that, exploiting the Liapunov's criterion, the system is internally stable. In other words, small perturbations of the initial conditions will reflect in perturbations in the output reaching a steady state condition. The stability analysis for the linear model has also been repeated for different values of D_i. Negative real eigenvalues are found for all the cases, as shown in Figure 3.20, confirming the expectation that the system is always stable, also in conditions different from the nominal one.

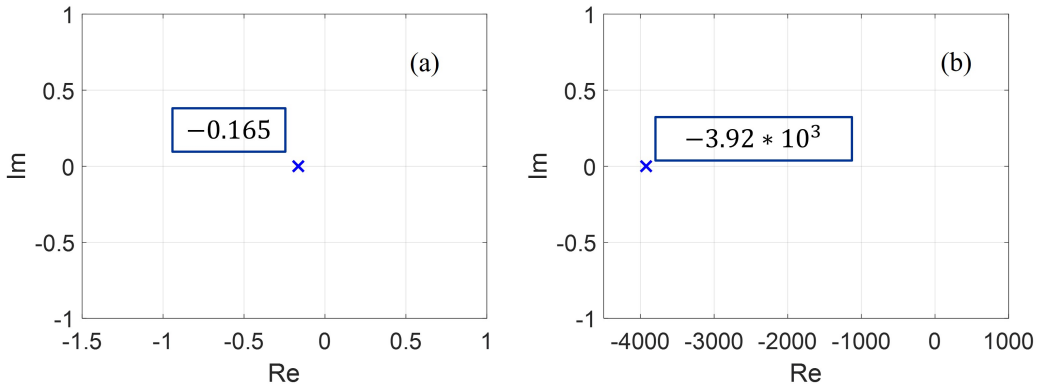

Fig. 3.19 (a) First and (b) second eigenvalue of the matrix A represented in the Gauss plane for the nominal case. Modified from [99].

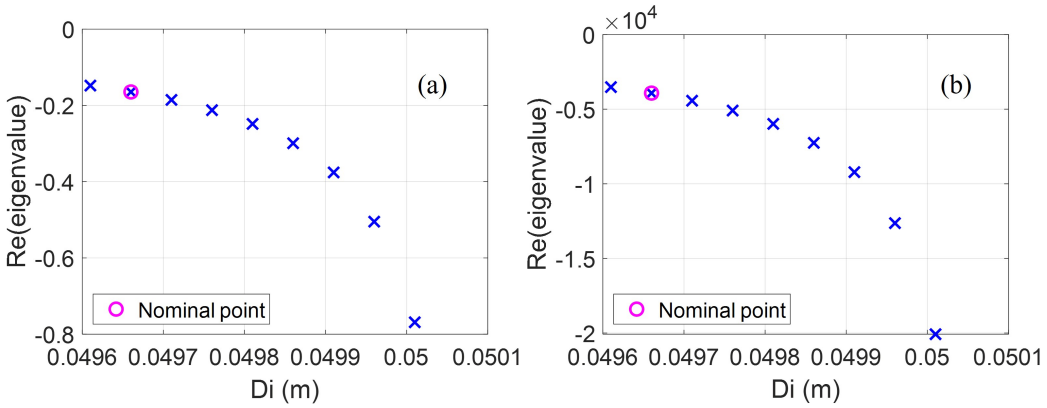

Fig. 3.20 Real part of the (a) first and (b) second eigenvalue of the matrix A on the y-axis for different values of D_i on the x-axis. Modified from [99].

The step responses of the linear and non-linear model are reported in Figure 3.21 for the perturbation of 1 $^{\circ}C$ of T_{in} and in Figure 3.22 for the perturbation of 1 kW of Q. In both cases, both T_m and T_c present similar behaviors in the linear and non-linear models. More in details, the results show that a steady-state condition is reached for all the quantities analyzed, with very similar time-constant for the two models. Also, the amplitudes of the step response are the same in the two models. This means that the non-linearity is not strong and the linear model can well represent the response, in the analyzed range of values. Moreover, no oscillations are observed, as expected since the eigenvalues are real. The time constants of the metal and the fluid, including the advective one are evaluated with equations 3.16, 3.17 and 3.18 respectively.

$$\tau_m = \frac{M_m C_m}{hA_s} \tag{3.16}$$

$$\tau_c = \frac{M_c C_c}{hA_s} \tag{3.17}$$

$$\tau_m = \frac{M_c}{\dot{m}} \tag{3.18}$$

Looking at the graphs in Figure 3.22, the metal temperature presents a higher time-constant (∼6 s), due to the higher thermal inertia of the material, if compared with the evolution of fluid temperature , showing a smaller time-constants (∼0.02 s and advective one $5.16 * 10^{-4}$ s). The vertical variation of the T_c in Figure 3.21 is due to the variation of the T_{in}, given the 0D model developed here.

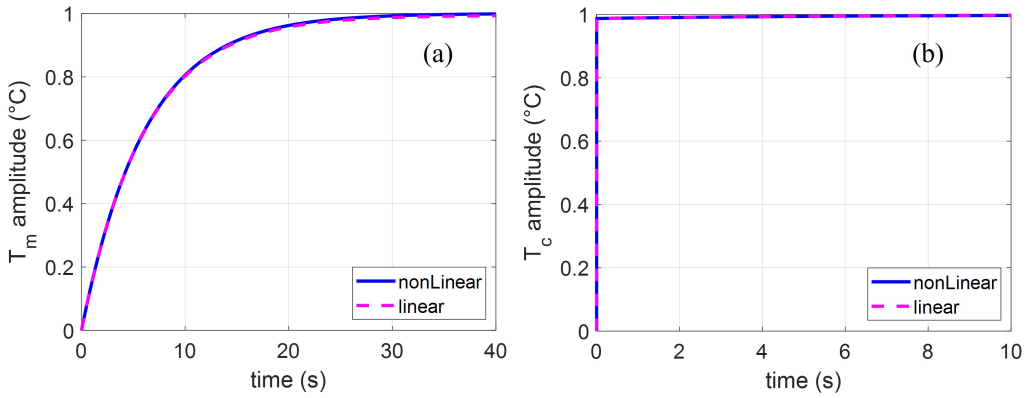

Fig. 3.21 Step response in case of 1 $^{\circ}C$ of perturbation in the T_{in} for the (a) metal temperature and (b) fluid temperature. Taken from [99]

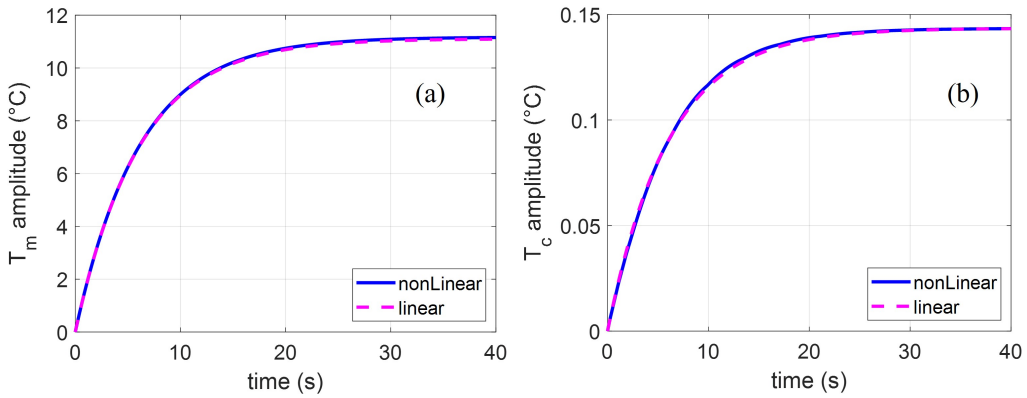

Fig. 3.22 Step response in case of 1 kW of perturbation in the Q for the (a) metal temperature and (b) fluid temperature. Taken from [99]

Numerical analysis

The $thick_f$ reduction reaches $\sim 25\%$ of the original thickness, and this shrinkage will cause a non-negligible effect on the different thermal-hydraulic behavior. A new simulation has been then done to check the performance of the deformed geometry, accounting for the computed radial displacement on the solid-fluid interface (blue line in Figure 3.3). To do that, the mesh deformation solver implemented in STAR-CCM+ has been used to deform the original mesh in a new one by adding the radial displacements previously found as an output of the thermo-mechanical simulation. The resulting geometry is reported in Figure 3.23. The new thinner annular region for the fluid was simulated, resulting in a decrease of the maximum temperature on the inner wall from $\sim 220°C$ to $\sim 202°C$, as effect of the higher fluid velocity and increased heat removal capability. That also leads to a decrease in the maximum radial displacement, showing that the feedback mechanism leads to a stabilization of the cavity dimension. On the same time, however, a consistent increasing in the pressure drop is experienced from ~ 3 bar to ~ 7 bar.

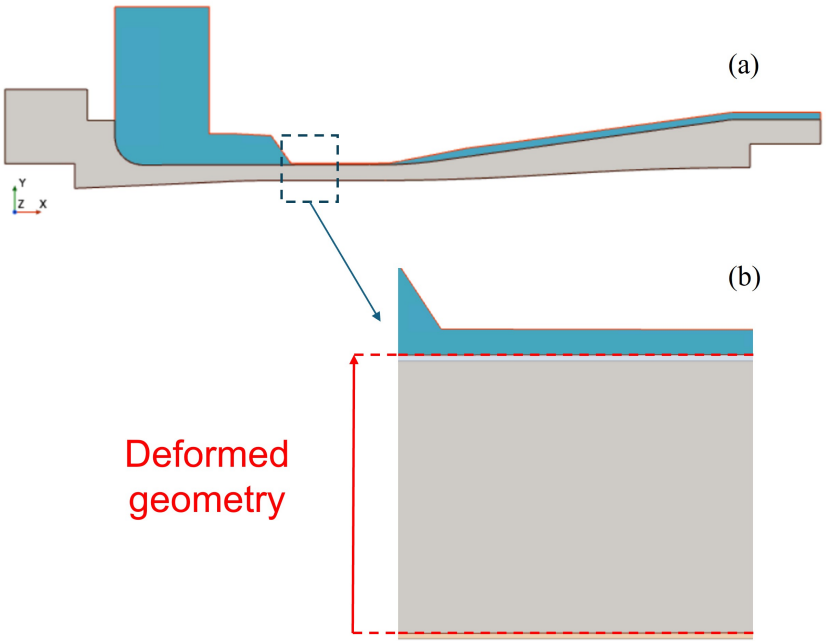

Fig. 3.23 (a) Section of the deformed geometry of the cavity cooled with annular configuration. In (b) a zoom is reported, where in light gray we can notice the displacement of the solid-fluid interface, causing the reduction of the flow passage area for the fluid.

3.2 Longitudinal cooling through mini-channels

If a annular cooling configuration has been considered and optimized in the previous section, here the longitudinal cooling direction is explored considering the adoption of ducts, in particular mini-channels, for the diameter dimension in the order of the millimeter. MCs make exploitation of the high speed of the water to increase the HTC and currently consitute the most viable alternative to RR in European gyrotrons.

This section is dedicated to a design improvement work conducted on a mini-channel cooling system, that is currently under experimental investigation.

3.2.1 Mini-channels design improvement

A design improvement study has been conducted on the cooling configuration based on longitudinal MCs. The starting point was already existing MCs design for the European gyrotrons, which showed promising cooling performances with respect to

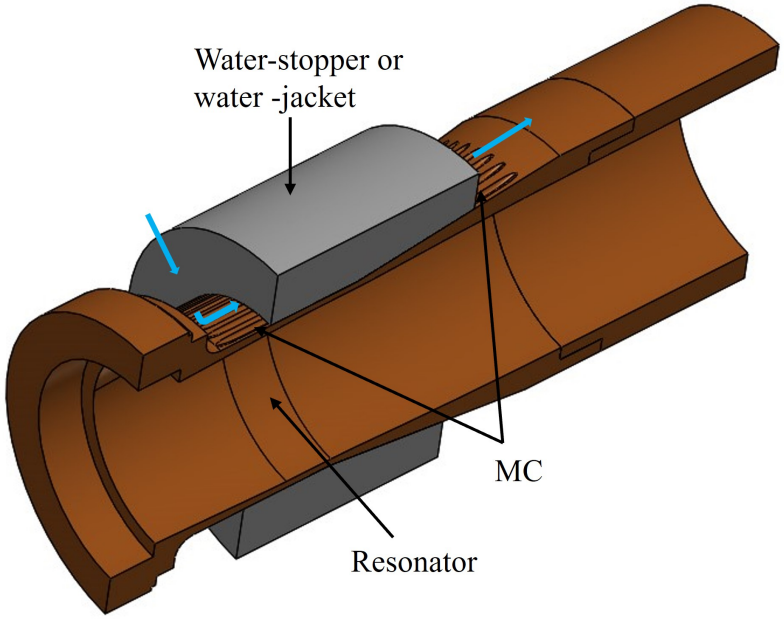

Fig. 3.24 CAD view of old mini-channels design with main components and the fluid path in light blue

RR, with the disadvantage of larger pressure drops [107]. In Figure 3.24 a traditional MC design is shown, with the MCs drilled in the resonator and the water-stopper (or water-jacket) used to force the water to flow in the MCs. To reduce the thermal stresses an "empty" WS was already proposed in [108] as well as a tapering of the WS at the channels inlet for decreasing the pressure drops (see Figure 3.25).

One of the drawbacks of the MCs configuration is the inhomogeneity of the cooling in the azimuthal direction, due to the inhomogeneous distribution of the flow rate in the MCs. To improve the flow distribution, the flow inlet pipe has been shifted axially, as shown in Figure 3.25 with the red dashed line. This allows the fluid to distribute azimuthally after entering the cooling circuit along the path preceding the channels inlet, hence the flow rates in the different channels will have smaller dispersion around the expected value (total flow rate divided by the number of channels). In Figure 3.26.a the maximum velocity in each channel computed in the middle section of the cavity is reported. The red circle represent the velocity, and hence the flow rate distribution in the MCs with the original inlet location, where a peak in the flow rates in the channels near the fluid inlet can be noticed. This is smoothed in the configuration with shifted inlet, as we can see from the velocity distribution given by the blue circles. In Figure 3.26.b the corresponding azimuthal

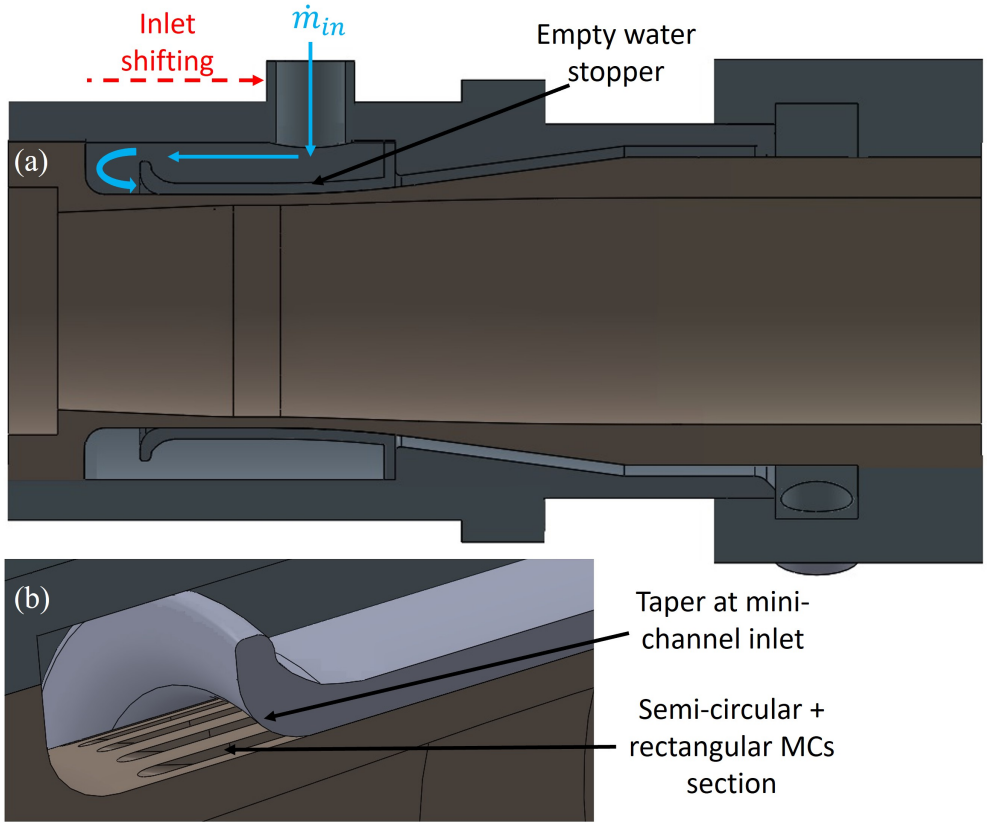

Fig. 3.25 a) longitudinal viw section of the MCs design with shifted inlet, showed with the red dashed line. The configuration is also equipped with the empty WS and the tapering at the channels inlet. b) A zoom on the MCs inlet.

temperature distribution is visible, showing a more homogeneous profile in the case of the shifted inlet (blue line).

A so-called short mini-channels design has also been proposed, by locating the channel entrance close to the area of the heat flux peak. In this way, a sort of jet effect is exploited, having the highest velocity at the abrupt section reduction where the maximum heat flux is expected. This is visible in Figure 3.27. A axial temperature profile comparison between long and short MCs, with same heat flux profile and flow rate, is given in Figure 3.27. A difference in the temperature peak of $\sim 14°C$ is observed, with a consequent reduction in the slopes of the profiles. This configuration also allows to erase the initial part of the channels, turning in a pressure drop reduction of $\sim 50\%$ (from 1.86 bar to 0.96 bar).

This analysis was conducted on the cavity for ITER 1509 gyrotrons. The resulting design has been adapted to the W7X 1507 gyrotron. The MCs section is built from

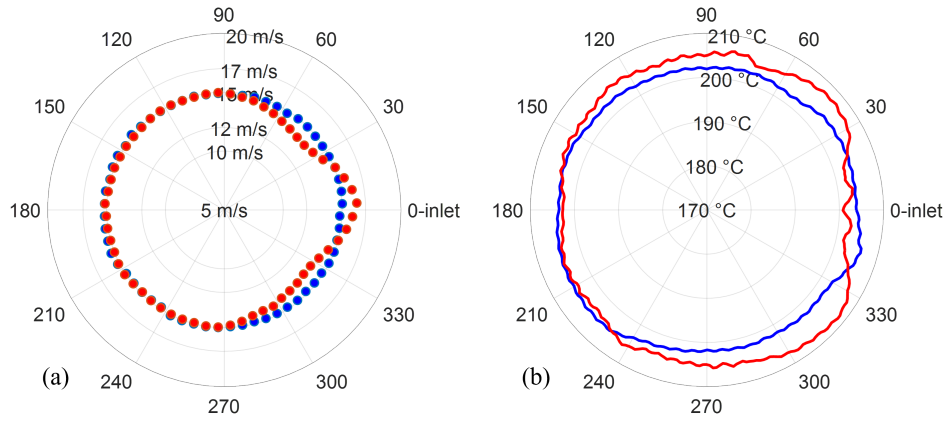

Fig. 3.26 In (a) the velocity distribution in the MCs and in (b) the azimuthal temperature profile at the midlle section of the cavity with old inlet in red and new shifted inlet in blu.

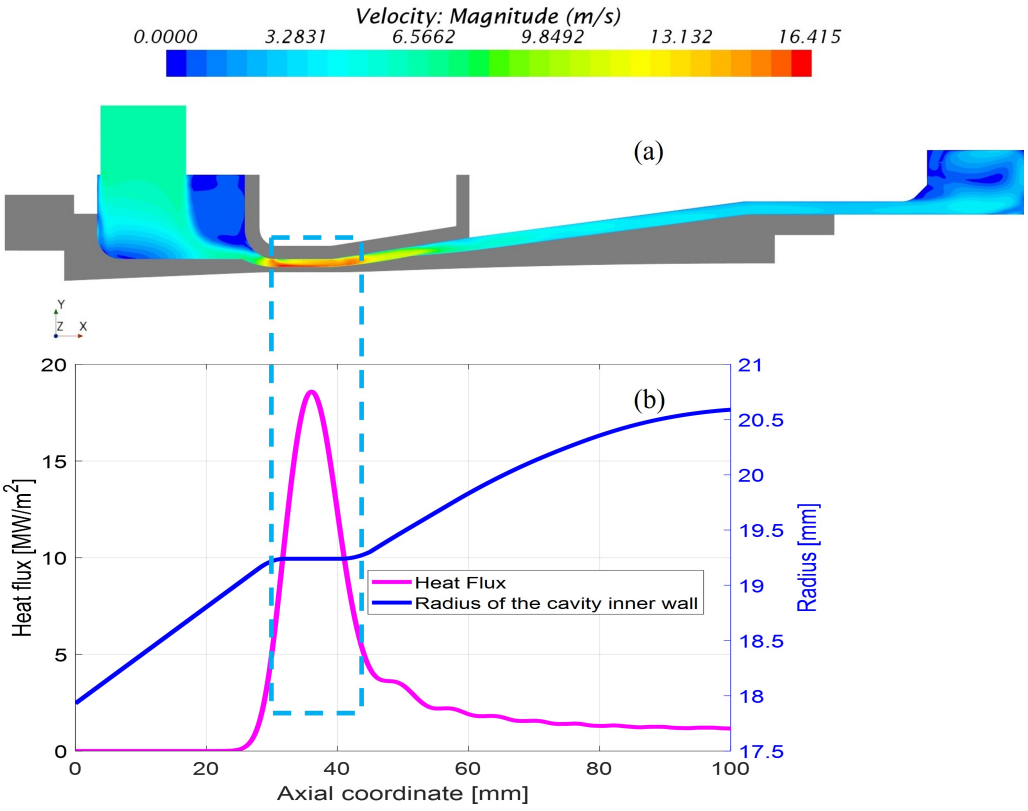

Fig. 3.27 (a) Velocity map in the short-MCs configuration. In (b) the heat flux profile used for the simulation and the radius of the cavity inner wall.

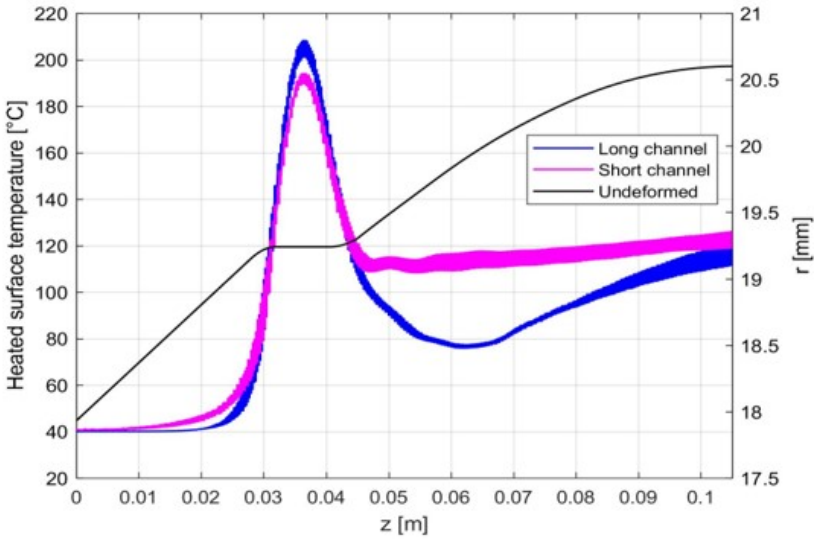

Fig. 3.28 Comparison of axial temperature profile for long and short MCs configurations.

a semicircular and rectangular section. This allows to have a small flow passage area but also reduce the distance between the channel and the heated surface (with respect to simple semicircular sections). A parametric investigation on the channel configuration and the flow rate was carried on. In particular three MCs configurations were analyzed with the following characteristics:

- C1 with 1 mm distance of MCs from the heated surface and 1 mm of MCs diameter;
- C2 with 0.8 mm distance of MCs from the heated surface and 1 mm of MCs diameter;
- C3 with 0.8 mm distance of MCs from the heated surface and 0.8 mm of MCs diameter.

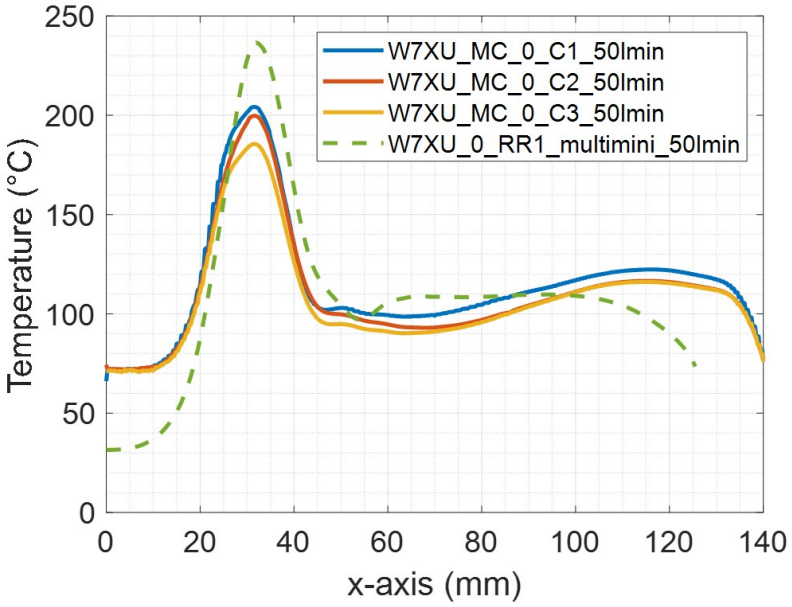

Fig. 3.29 Comparison of axial temperature profile for different MCs configurations and RR.

Both the reduction of the distance from the heated surface and the diameter are expected to go in the direction of a cooling capability improvement. The obtained axial temperature profiles of the three configurations are compared to the RR solution in Figure 3.29. A general better cooling behavior is evident for the MCs solutions. The C3 solution presents the best results and a larger improvement from C2 than C2 from C1. This suggests that the high fluid speed, giving the high HTC, plays a major role in the cooling with respect to the distance from the heated surface. Also concerning the thermo-mechanical analysis (see Figure 3.29), lower displacements and stresses are found in the two MCs configurations than the RRs one, with a better behavior of C3, following the thermal-hydraulic analysis. This study led to the realization of a mock-up equipped with MCs with C3 (Figure 3.31). Moreover, a gap of $\sim 60\ \mu m$ between the resonator and the WS was included, to reduce the thermal stresses. The mock-up is currently under experimental investigation for the hydraulic characterization.

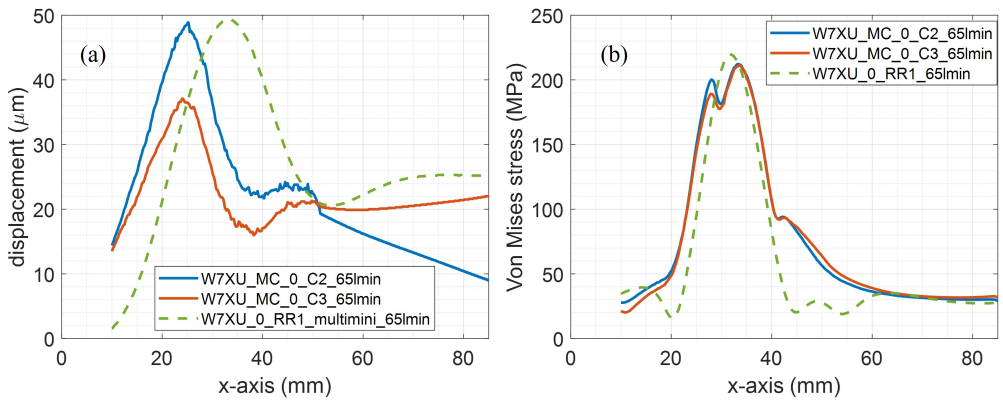

Fig. 3.30 Radial displacements and stresses axial profile for different MCs configurations and RR.

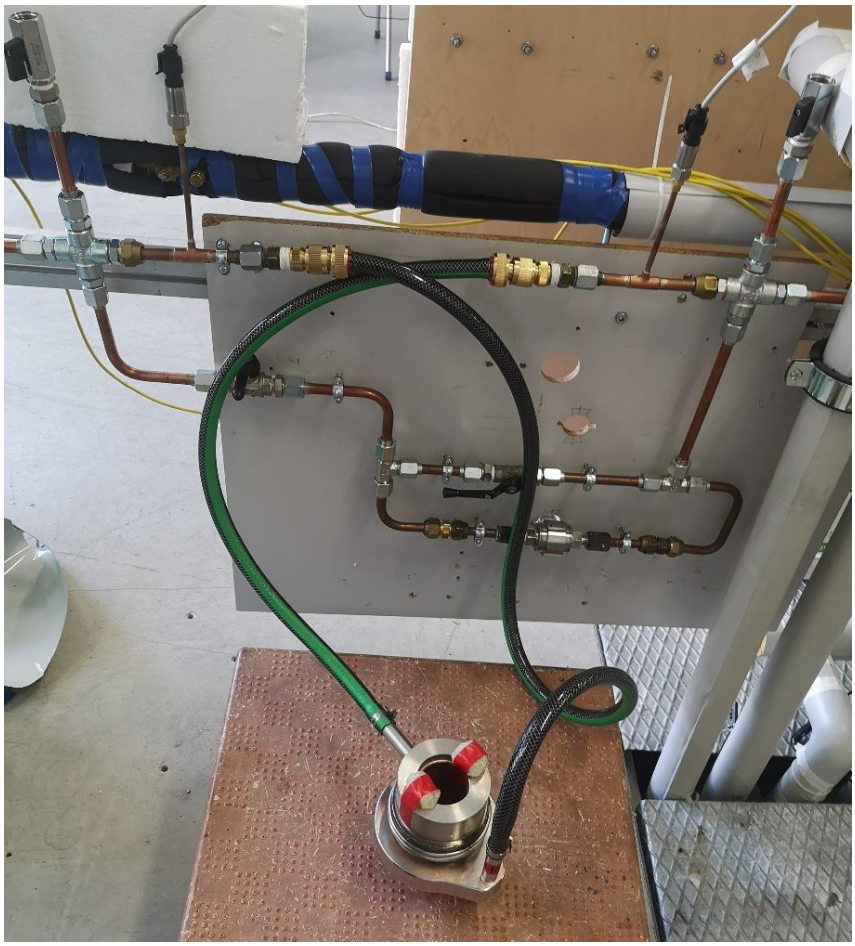

Fig. 3.31 Thales mock-up with new short MCs design installed in the hydraulic loop at PoliMI.

Chapter 4

Analysis and optimization of cooling techniques with azimuthal flow direction

In the current chapter, cooling solutions that exploit mainly the azimuthal direction of the flow, are investigates. the use of azimuthal flow of the coolant aims to circumferentially homogenize the cooling and reduce pressure drops. The discussion is devoted to the anlysis of an "experienced based" design, and optimization based designs.

Portions of the present chapter were already published in the following scientific papers:

- R. Difonzo, A. Allio, A. Cammi and L. Savoldi, "Comparative analysis of different strategies exploiting the adjoint topology optimization method for enhancing the performance of a cooling device equipped with micro-channels.", *In Proceedings of the 16th International Conference on Heat Transfer, Fluid Mechanics and Thermodynam-ics*, 2022. [109]
- R. Difonzo, A. Cammi, N. Galanos, K.C. Giannakoglou, E.M. Papoutsis Kiachagias and L. Savoldi, "Design of the Cooling System of the cavity of the European Gyrotron Using Adjoint-based Topology Optimization Exploiting the Azimuthal Flow Direction", to appear *In Proceedings of the 14th International Conference on Computational Heat and Mass Transfer* [110].

Part of the work of this chapter has been carried out within the framework of the EUROfusion Consortium, founded by the European Union via the Euratom Research and Training Programme, (Grant Agreement No 101052200 — EUROfusion), within the Work Package W7X. The views and opinions expressed are those of the authors' only and do not necessarily reflect those of the European Union or the European Commission. Neither the European Union nor the European Commission can be held responsible for them.

4.1 Azimuthal micro-channels analysis and optimization

A design proposed by the IPP that aims to exploit azimuthal flow of the coolant is based on azimuthal micro-channels surrounding the cavity. As shown in Figure 4.1.a, the cooling strategy is organized in several parallel micro-channels arrays. The micro-channels in each array are fed by longitudinal inlet manifolds, and in a Z-type arrangement [111], the water is re-collected in longitudinal outlet manifolds. For better clarity on the fluid path in the longitudinal manifolds and the azimuthal microchannels see the zoom in Figure 4.1.b. It is known from experimental and preliminary numerical investigations (performed on the slice in Figure 4.2.a) that in such manifold configuration the flow is larger in the channels near the outlet [112], in the case the manifold has a constant cross section along its length, as the case at hand (see Figure 4.2.b). As a consequence, the heat removal is lower at the location of the heat flux peak and much more effective downstream of the peak, leading to temperature gradients. However, from previous studies we learnt that the flattest the temperature axial profile along the cavity is, the lowest the stresses are. For that reason, it is important to have a cooling capability of the cavity which follows the heat flux shape, with the consequent need for the optimization of the flow distribution among the micro-channel along the cavity. The shaping of the manifold has been already identified as an efficient way to balance the flow distribution among the parallel channels. In [112], for instance, a linear tapering of the manifolds was demonstrated to allow an almost uniform flow repartition among a series of equally-spaced channels. A similar effect is achieved in [113] using triangular manifolds.

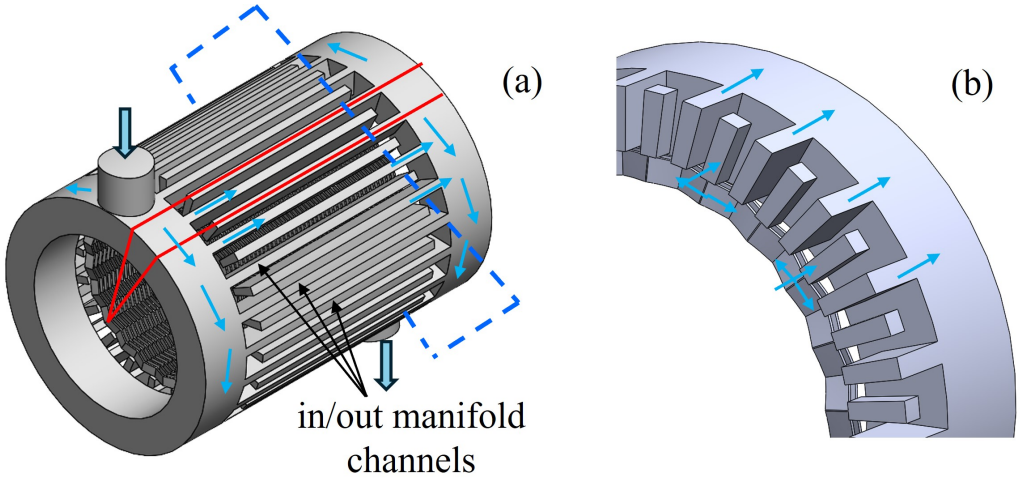

Fig. 4.1 a) Pre-conceptual design of cavity cooling concept by parallel flow distribution through micro-channels and b) Zoom on a transversal section (dashed blue lines on the entire geometry) of the fluid path in the microchannels and their respective inlet and outlet manifolds

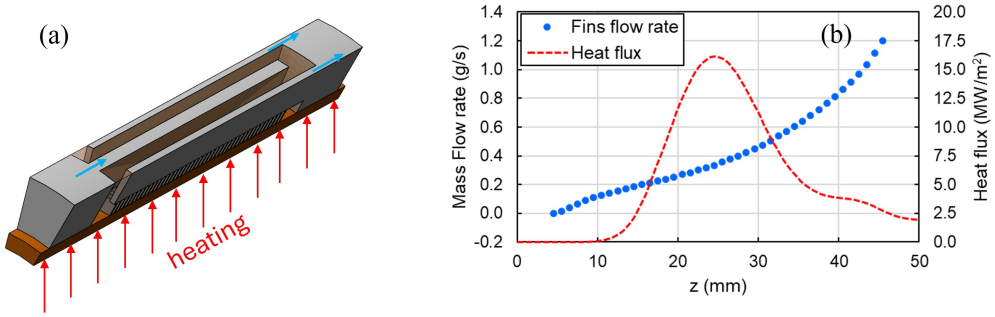

Fig. 4.2 a) Periodic slice of the mirochannels configuration, corresponding to the red lines confined region in Figure 4.1 b) flow rate distribution in the azimuthal microchannels

In the case at hand, however, the flow within the micro-channels in parallel should be non-uniform if equally-spaced channels are used, in view of the strongly non-homogeneous heat flux the coolant should remove. If a uniform flow distribution among channels is targeted, then the channel density should be adapted to the heat flux shape. Simply tapered or triangular manifolds as those used in [12] and [13] cannot comply then with the flow rate or channel distribution for the case at hand, requiring a dedicated optimization of the inlet and outlet manifold geometry. The optimization itself is performed on the manifold geometry, using adjoint-based topology method, in order to control the flow rate distribution in the micro-channels.

Two different strategies are adopted. In the first one, the channels density along the manifold is modified according to the heat flux shape (Case A, "equally-loaded channels" see Figure 4.3.a), while the manifold geometry is optimized in order to have a homogeneous distribution of the flow rate in the channels. In the second strategy, a homogeneous distribution of the micro-channels along the manifolds is retained (Case B, "equally-spaced channels", see Figure 4.3.b), and the manifold geometry is optimized to get a flow rate distribution suitable to cope with the heat flux shape. The aim of this comparative study is first the assessment of the best optimization procedure that, using the adjoint topology optimization and the whished flow rate distribution in the micro-channels as the target function, allows reaching the desired results in terms of cooling. Second, the comparative analysis of the two strategies aims at identifying the solution which could be more suitable to be manufactured with additive manufacturing technologies.

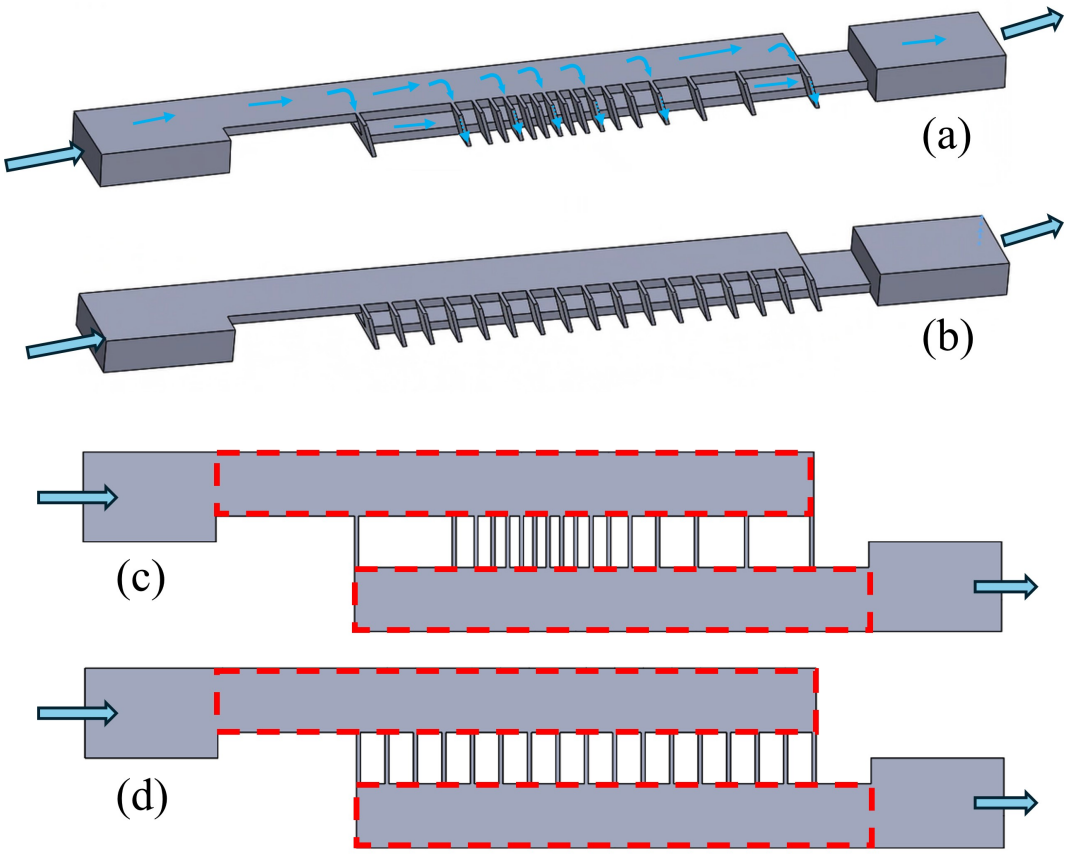

Fig. 4.3 3D sector of the initial geometry for (a) Case A and (b) case B and 2D computational domain used for the topology optimization for (c) case A and (d) case B. The red dashed lines in (c) and (d) indicates the design space where solid can be added in order to minimize the cost function. Taken from [109].

4.1.1 Methodology

The optimization work presented here starts from an initial design equipped with azimuthal micro-channels, hence the use of ducts is present here. The optimization method used is the ATO implemented in the commercial software STAR-CCM+. The optimization is based on advancing a level set of equation [114] as in eq. 4.1

$$\frac{\partial \Phi}{\partial \tau} + \mathscr{F}||\nabla|| = \mathscr{S} \tag{4.1}$$

where τ is the pseudo time, $\mathscr{F}$ is the interface velocity between two phases and $\mathscr{S}$ is the source term of the level set function. Φ is the level set variable, which varies

between -1 (secondary phase - solid) and 1 (primary phase - fluid). The associated material distribution $\in [0,1]$ is defined using the hyperbolic tangent of the level set function variable, as reported in eq. 4.2

$$\chi = 0.5 * \left(1 + tanh\left(\frac{\Phi}{\iota}\right)\right) \tag{4.2}$$

where ι controls the thickness of the interface and is set to 0.1 in the code. The material distribution will take 0 value in solid region and 1 in fluid region.

In order to simulate the effect of the solid material, hence provide a design model as in Figure 2.3, the blockage of the flow is modeled using the Brinkman Penalization. A source term is added to the momentum equation to force the velocity to zero in case of solid material regions.

In Figure 4.4 the work-flow of the ATO algorithm is shown. The initial computational domain (filled only by the fluid phase) is first analysed numerically and a first flow field is computed with a coarse grid. Then the objectives and constraints sensitivities are computed using the adjoint method. The design variable (in this case the material distribution) is updated using a gradient-based optimizer (the Generalized Minimal Residual Method is used in STAR-CCM+) and the new problem is solved computing again the flow field. The procedure is repeated for a number of iterations, until the value of the objective function stabilizes. Then the geometry is cleaned (manually) from the portion of the domain that has been attribute to the solid, a CFD simulation is run to check the global performance of the new geometry with respect to the target, and the ATO procedure is restarted if needed.

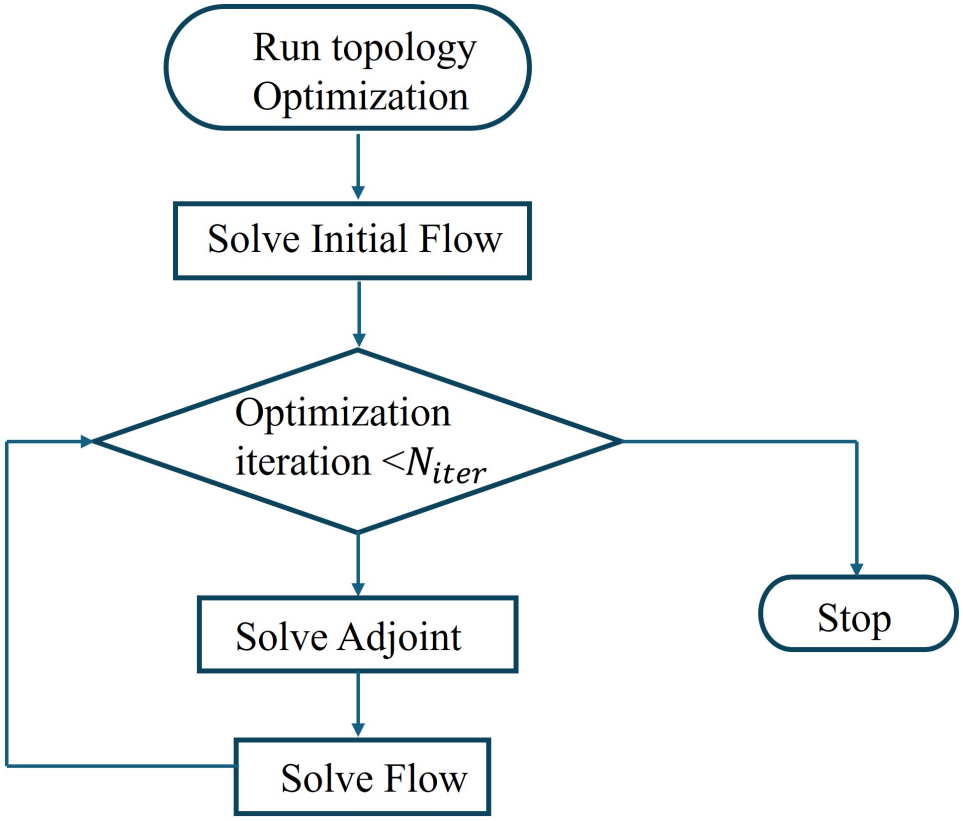

Fig. 4.4 Work-flow of the adjoint topology optimization algorithm.

4.1.2 The optimization problem

The computational domain is shown in Figure 4.3.c-d. To reduce the computational cost of the optimization process, the study is performed on a 2D model. Moreover, this choice allows to eliminate a degree of freedom in the azimuthal direction, which means that the final optimized solution is forced to be axisymmetric to reduce complexity in terms of manufacturability. The manifolds constitute the design space of our optimization problem. More precisely that region is individuated by the red dashed lines in Figure 4.3.c-d. The solid phase is allowed to grow only from the boundaries, i.e. near already existing solid spots. The aim of the optimization is to obtain a target flow rate distribution by varying the geometry of the manifolds, constituting the design space of the optimization problem. By using topology optimization, the number of design variable is equal to the number of cells. Moreover, the target flow rate distribution should be obtained while keeping the pressure drop as low as possible. The cost function J of the optimization problem

has been built in order to meet both these requests and is defined with Eq. 4.3. In the equation $\dot{m}_{dev}$ is defined as the sum of all the differences between the target flow rate $\dot{m}_{target,i}$ and the obtained one with the optimization $\dot{m}_i$, in each $i-th$ channel. This is explicited in Eq. 4.4, where N_{ch} is the total number of channels . The coefficient w is used to weight the importance of the flow deviation in the cost function and has been set to 10^{-6} from preliminary analysis.

$$J = \Delta p + w * \dot{m}_{dev} \tag{4.3}$$

$$\dot{m}_{dev} = \sum_{i=1}^{N_{ch}} (abs(\dot{m}_i - \dot{m}_{dev,i})) \tag{4.4}$$

Case A: equally-loaded channels

A first optimization study has been performed in the case the distance among the 17 channels is adjusted to guarantee that each channel removes in principle the same heat, with the same temperature increase at the outlet. The resulting channel density is shown in Figure 4.3.a, where the minimum distance between adjacent channels is kept at 1 mm, assumed as the minimum distance that can be manufactured using Additive Manufacturing techniques.

Case B: equally-spaced channels

The second optimization study has been performed in the case of 17 equally-spaced channels, imposing the target flow rate distribution such as to give the same temperature increase at the channel outlet. The target flow rate values have been obtained starting from the heat flux $\ddot{Q}$ integrated on the longitudinal portion of the cavity cooled by each channel, according to Eq. 3. The desired HTC in the different microchannels (see 4.5) is assume to depend on the Dittus-Boelter , see Eq. 4.6, to link the flow rate distribution to the HTC. The resulting target flow rate distribution is shown in Figure 4.5, where the trend of the target flow rate coming from Eq. 4.7 is retrieved.

$$\dot{Q}_i = \int \ddot{Q} dl \sim \sum_{i=1}^{17} HTC_i (T_{out} - T_{in}) \Delta l_i \tag{4.5}$$

$$HTC_i = 0.023 \frac{k}{D} Re^{\frac{4}{5}} Pr^n \propto \dot{m}_i^{\frac{4}{5}} \tag{4.6}$$

$$\dot{m}_i \propto \dot{Q}_i^{\frac{5}{4}} \tag{4.7}$$

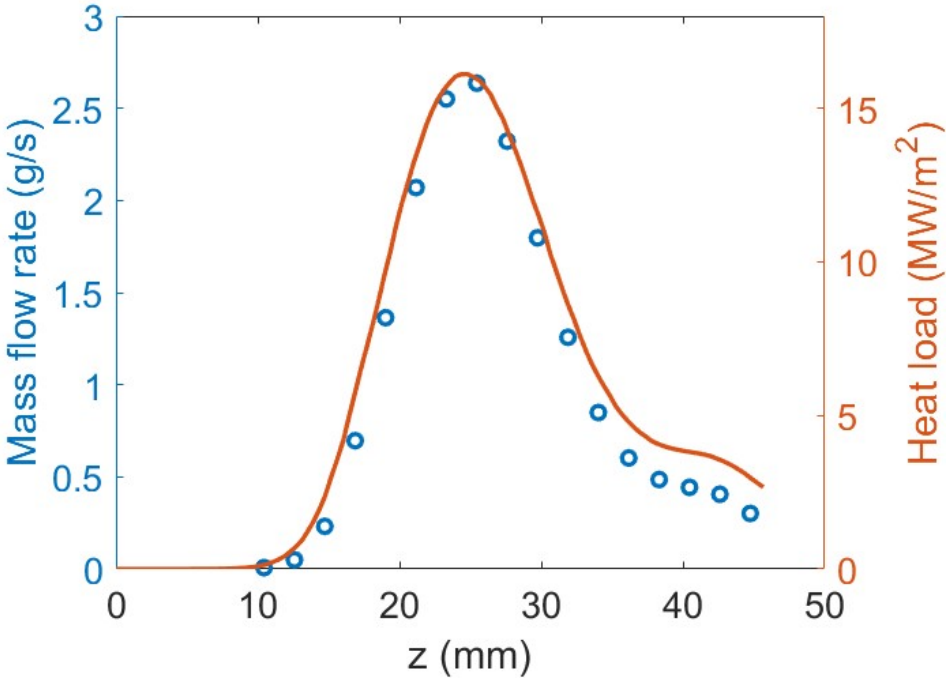

Fig. 4.5 Target flow rate distribution in the different micro-channels, for the equally-spaced configuration, represented with blue circles. The desired flow rate distribution is evaluated based on the heat flux axial profile (red solid line). Taken from [109].

4.1.3 Optimization results

Both configurations have been optimized using the 2D simplified geometry in 4.3.c-d. Laminar flow is considered in the micro-channels, as resulting from preliminary simulations with the nominal mass flow rate of 1.3×10^{-3} kg/s (corresponding to 0.0181 kg/s in the 3D geometry) of subcooled water with constant thermophysical

properties. To allow for transition regime in the manifolds, the $\kappa-\omega$ SST $\gamma-$ $transition$ model has been adopted in the simulations. In both cases, a reference CFD simulation has been performed for the initial configurations, to evaluate distance between the non-optimized mass flow rate distribution and the target one. A Key Performance Indicator (KPI) has been defined to measure the performance of the optimization procedure, defined as in Eq. 4.8.

$$KPI = \sqrt{\frac{\sum_{i=1}^{N}(\dot{m}_i - \dot{m}_{target,i})^2}{N}} \tag{4.8}$$

In order to check if the optimization is forcing the flow where it is expected, according to the target, a second set of simulations has been performed on the two manifolds separately, imposing as boundary condition exactly the target mass flow rate distribution in the middle of the micro-channels, and identifying the resulting streamlines.

Case A: equally-loaded channels

For case A, the first two steps of the optimization are reported in terms of "*material indicator*" χ in Figure 6a-b. The region of the manifolds filled with solid after the first optimization (Figure 4.6.a) are used as a guideline to reduce the optimization region in the second optimization step, which highlights the need for a careful shaping of the tapering of the inlet manifold. The result of the second optimization presents some porous zones (intermediate values of the impermeability field) among the channels in the outer manifold, which makes a direct engineering design not straightforward. By lessons learned from literature and by the comparison with the streamlines computed in the inlet manifold when the target flow rate is imposed as boundary condition (Figure 4.7) the final geometry shown in Figure 4.6.c has been drawn. Note that the inlet manifold tapering, beginning at the axial location of the first channel show a variable slope, the closer the channels the bigger the slope. The final thickness of the inlet manifold is reduced to a value comparable to the channel width, to ensure manufacturability. Also, in the outer manifold the large recirculation zone between the first and the second channel is somewhat corresponding to the area that is already removed after the first optimization.

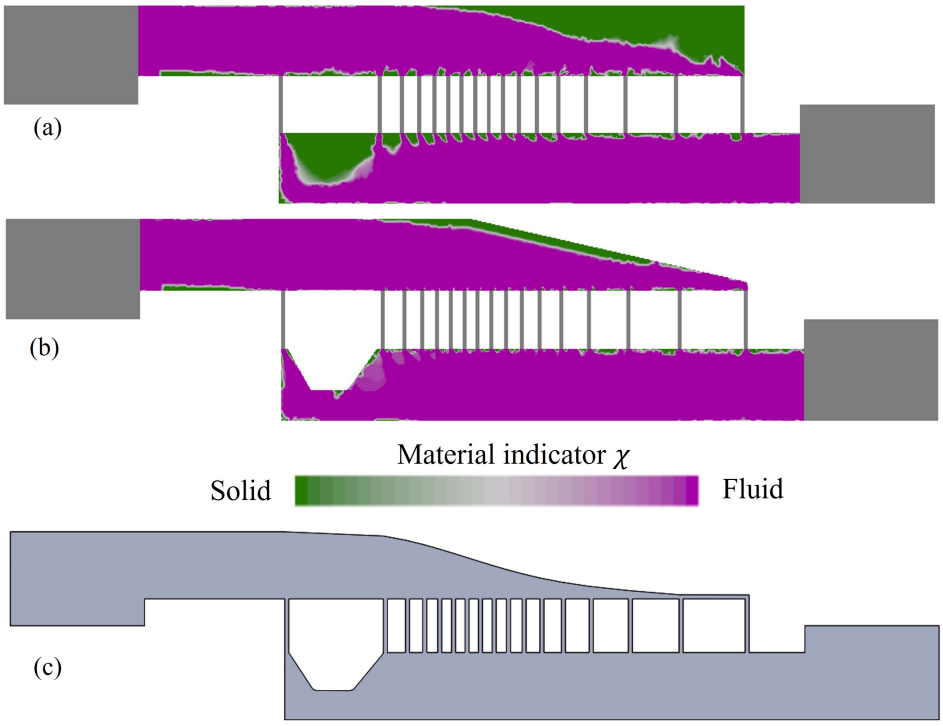

Fig. 4.6 Case A: topology optimization results: (a) first iteration, (b) second iteration, (c) final configuration. The flow in all figures is from left to right. Taken from [109].

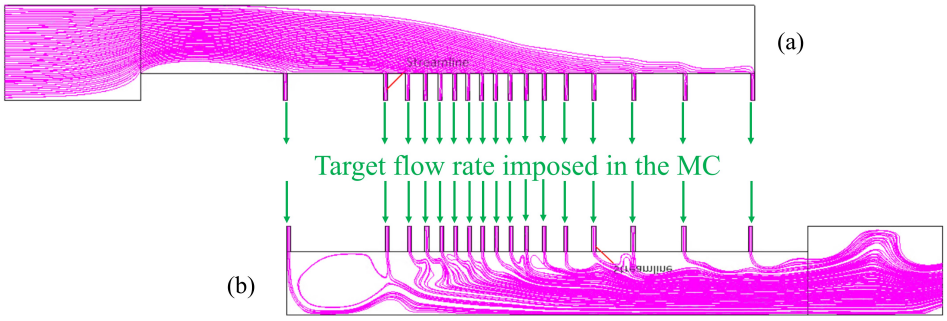

Fig. 4.7 Case A: streamlines computed in the original geometrical configuration, separately for the inner (a) and outer (b) manifold, imposing a uniform flow rate in the micro-channels. The flow is from left to right. Taken from [109].

The effect of the optimization on the flow rate distribution is shown comparatively for the non-optimized and final configurations in Figure 4.8.a, after computing the fields on a body-fitted mesh, with the exact boundary conditions. A significant improvement toward the target distribution is shown, with a maximum relative difference between the actual value and the target reducing from 40% to 20%. The

efficacy of the new optimized configuration is verified on a 3D geometry and the flow rate distribution is shown in Figure 4.8.b, where a behaviour similar to the 2D one can be observed, demonstrating the validity of the method where the optimization is conducted on a 2D geometry.

The *KPI* for the final configuration is 1.32×10^{-4}) kg/s, while the value for the non-optimized configuration was 2.3310^{-4} kg/s. The total pressure drop is 0.027 bar for the initial configuration and 0.03 bar for the final one.

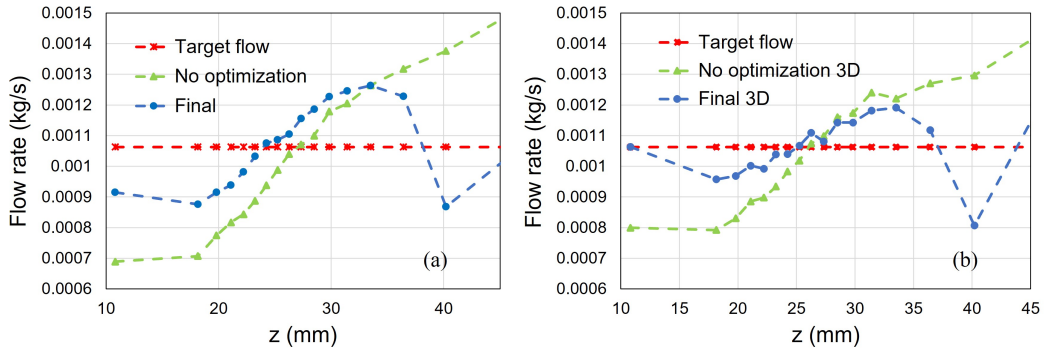

Fig. 4.8 Case A: flow rate distribution computed for the non-optimized and final configuration in the 2D (a) and 3D geometry. Taken from [109].

Case B: equally-spaced channels

For case B, the first two steps of the optimization, reported in terms of the material indicator χ in Figure 4.9.a-b, show the formation of very thin passages for the fluid in the outlet manifold. In the second configuration (Figure 4.9.b) the first channel is not even directly connected to the rest of the fluid domain but through a very small porosity. This is an effect of the very uneven flow distribution requested by the cost function (Figure 4.5) where the first and last channels should allow the passage of a very small flow rate. The geometry after the first two optimization steps is shown in Figure 4.9.c, showing this time a significant difference with respect to what was obtained from the separate analysis of the two manifolds, imposing the target flow rate as boundary condition (Figure 4.10).

From the analysis of the flow path connecting the first and last channels to the manifold main stream in Figure 4.10 it appears clear that the low flow rate there requires a tortuous fluid path, with narrow channels, which develops however in regions that the ATO tends to fill with solid.

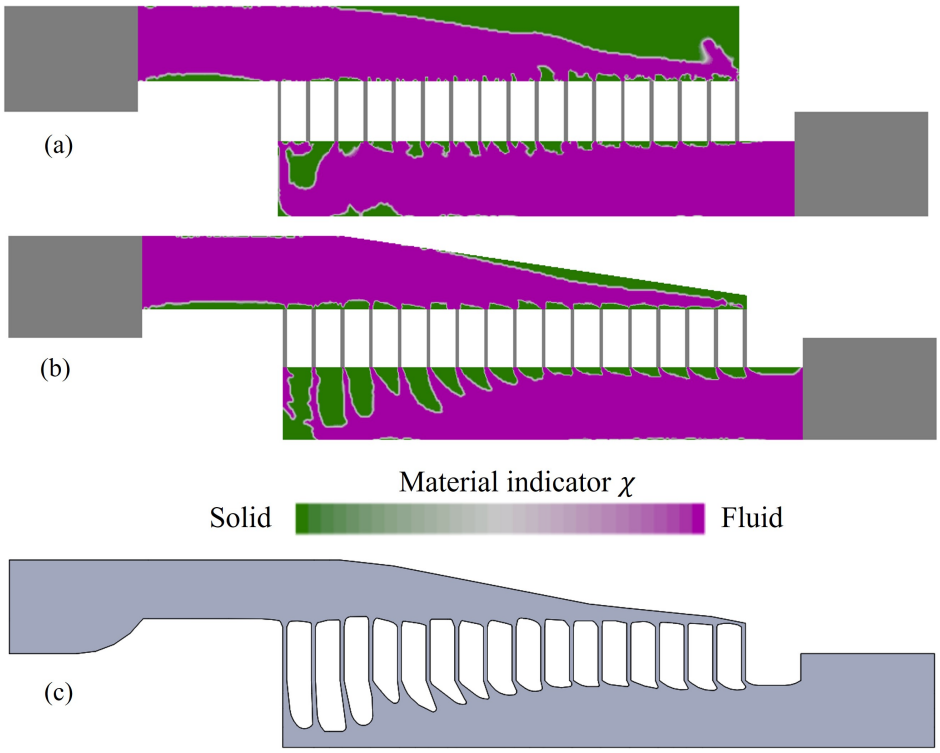

Fig. 4.9 Case B: topology optimization results: (a) first iteration, (b) second iteration, (c) final configuration. The flow in all figures is from left to right. Taken from [109].

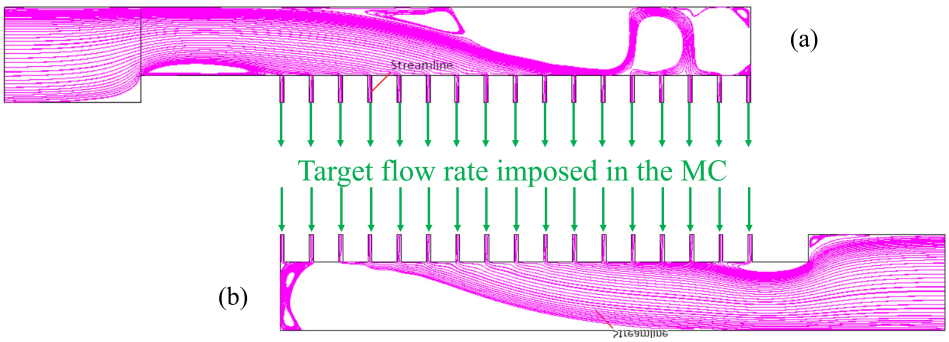

Fig. 4.10 Case B: streamlines computed in the original geometrical configuration, separately for the inner (a) and outer (b) manifold, imposing the flow rate distribution proportional to the heat load in the micro-channels. The flow is from left to right. Taken from [109].

The result of the optimization in terms of flow repartition in the channels for Case B is reported in Figure 4.11. While the non-optimized configuration shows the typical increasing trend expected form the Z-manifold configuration, in the optimized configuration the flow in the first and last channels tends to be lower than

in the middle of the array. However, the flow reduction at both ends is far from being comparable to the target values, and that affects the flow rate in the central channels, which is much lower ($\sim 50\%$) than the target. Note that both geometries (the one coming from the result of the optimization and the one which could be drawn following the streamlines) appear very hard to by manufactured in view of the very articulated and thin flow passages. The *KPI* for the final configuration is 7.95×10^{-4} kg/s, while the value for the non-optimized configuration was 9.36×10^{-4} kg/s. The total pressure drop varies from a value of 0.027 bar in the initial configuration to 0.023 bar in the final optimized one.

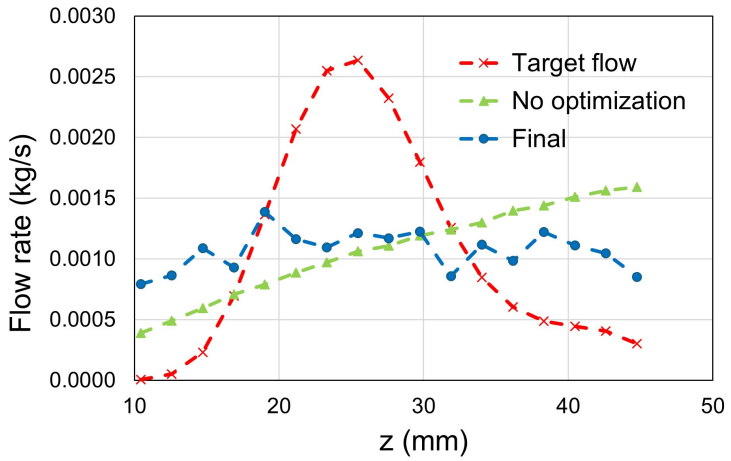

Fig. 4.11 Case B: flow rate distribution computed for the non-optimized and final configuration. Taken from [109].

Results comparison

The comparison between the two configurations analysed here shows how a uniform flow repartition among a series of micro-channels connected in parallel to Z-manifold is easier to be addressed than an uneven one using the Adjoint Topology Optimization technique, notwithstanding despite the non-uniform spacing of the channels. When a non-uniform flow distribution is targeted, indeed, the flow streams at the inlet and outlet of the channels become very narrow and difficult to be drawn out of the optimization process. From another side, they also would become very hard to be manufactured. In the case of uniform flow distribution target, on the contrary, the optimized geometry of the manifolds appears relatively easy, and in line with the expectations from simple CFD analysis. The microchannels cooling concept is also

under consideration for the divertor modules for W7X [115]. The optimization study conducted here led to the adoption of a simile-triangular shape for the manifold adopted for the divertor modules [116].

4.2 No-duct azimuthal flow cooling optimization

In this section, an optimized design of the cavity cooling strategy that exploits azimuthal flow direction is searched. The idea here, differently from the previous section, is to start from an initial domain with no ducts in the azimuthal direction.

4.2.1 Methodology

The work presented here adopts the adjoint-based topology optimization s/w developed in OpenFOAM by the Parallel CFD & Optimization Unit of the National Technical University of Athens [117]. The method used for the design model is the density approach described in subsection 2.1.2. To solve the coupled fluid and thermal problem, the energy equation is solved over Ω_d to compute the temperature field, by appropriately interpolating the thermal conductivity of the fluid and solid. Within each cycle of the optimization algorithm, the flow field of the current configuration is initially computed. Then, the sensitivities of objectives and constraints are computed by the continuous adjoint method [54] at a cost which does not depend on the number of design variables . The Method of Moving Asymptotes (MMA) [118] makes use of the so-computed gradients to update the impermeability field at cell-centers, considering that α should be bounded between 0 and 1.

4.2.2 Optimization problem setup

The computational domain used in the optimization is just a portion (1/23) of the gyrotron cavity, taking advantage of the periodicity of the geometry, and it is reported in Figure 4.12. The fluid enters the domain and is distributed in the two halves of the inlet longitudinal manifolds, from where it then flows in the azimuthal direction, towards the central longitudinal outlet manifold. Two fixed impermeability regions are set: the fluid one with impermeability equal to 0, colored in blue in the figure, and the solid one, with fixed impermeability equal to 1, in red in the figure. The

design space is initially filled by fluid, indicated in magenta in the figure. Constant water properties are used and the thermal conductivity is interpolated between water (0.62 W/m/K) and Glidcop (351 W/m/K) values. Periodic conditions were imposed at the periodic boundaries and the heat load is imposed through a thermal gradient profile boundary condition on the solid inner wall. An inlet velocity of ∼0.904 m/s is imposed as the inlet condition, derived from the nominal value of 50 l/min for the whole circular geometry, and 0 bar of (reference) pressure as the outlet condition. An initial hexahedral mesh of $\sim 6 \times 10^6$ cells is generated, with a refined zone in the fluid area below the manifold, with an average cell size of ∼0.05 mm in each direction.

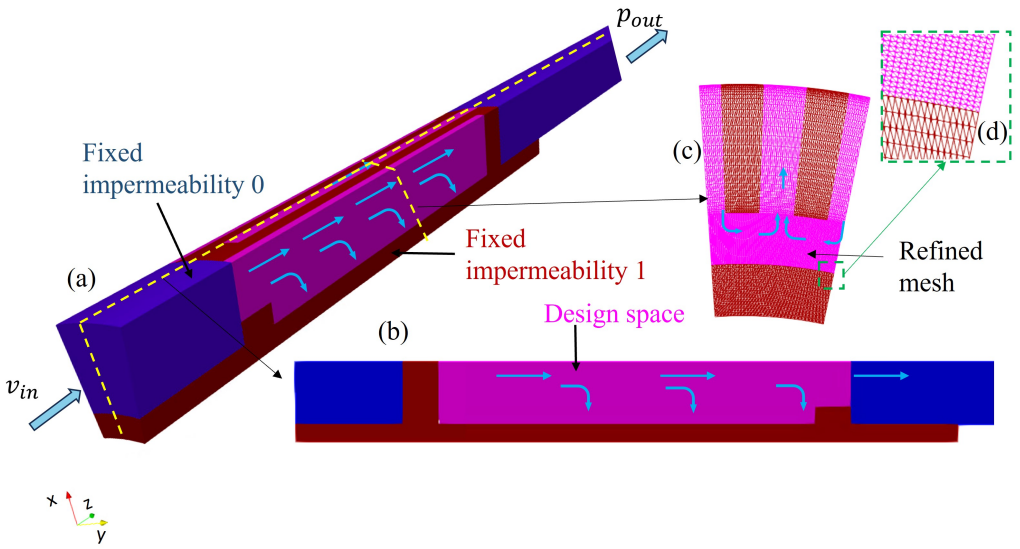

Fig. 4.12 (a) Computational domain for the optimization: in red the solid constant impermeability region, in blue the fluid constant impermeabilty region, in magenta the design space with (b) a longitudinal section of the outlet manifold and (c) a cross section in the middle of the designspace and cavity and (d) a zoom on the refined mesh. Taken from [110].

In order to reduce the number of design variables, a volumetric NURBS lattice was used and this introduced control points (CPs) [119]. The impermeability field is now updated in the CPs, constituting the new design variables. Having the α^{ijk} values at the lattice nodes available, the ones at the cell centers are computed as in Eq. 4.9

$$\alpha = \sum_{i=1}^{NX-1} \sum_{j=0}^{NY-1} \sum_{k=1}^{NZ-1} U_{i,pu}(u) V_{j,pv}(v) W_{k,pw}(w) \alpha^{ijk} \tag{4.9}$$

where u, v, $w \in [0,1]$ are the parametric coordinates evaluated at cell P and U_i, V_j, W_k are the polynomial basis functions of degree $pu = 3$, $pv = 3$ and $pw = 2$ respectively. One control point per 5 cells (i.e., spaced by 0.25 mm) has been defined in each direction of the domain, giving rise to a control grid of $NXxNYxNZCPs$ (14 x 16 x 180 in the present study) in the radial, azimuthal and longitudinal directions, respectively.

The optimization problem has been defined to account not only for the minimization of the mean temperature (to minimize displacements) but, also, of temperature gradients to control stresses. To do that, a weighed cost function with two contributions, the normalized values of the mean temperature T_{mean} and its standard deviation $stdev(T)$, both evaluated on the heated surface, was defined. The weighted cost function is reported in Eq. 4.10

$$J = w_1 T_{mean} + w_2 stdev(T) \tag{4.10}$$

where w_1 and w_2 are the weights of the two contributions to J. In the present optimization, the weights take on the values: w_1=0.15 and w_2=0.85.

To limit the total pressure drop, a constraint was imposed. The total pressure drop should be below 0.46 bar (obtained from previous evaluations on the azimuthal micro-channels cooling solution in [13]). The constraint on total pressure losses is imposed with Eq. 4.11

$$G_p = \frac{J_p - J_{p,target}}{NormFactor} < 0 \tag{4.11}$$

where J_p is the evaluated value of total pressure drop at the optimization cycle, while $J_{p,target}$ is the target value and $NormFactor$ is a normalization factor.

A constraint on the fluid volume ratio was also imposed which should be less or equal to 0.63, to have at least 50% of the design space filled with solid. The constraint on the volume ratio is imposed with Eq. 4.12

$$G_v = \frac{r_f}{r_{f,target}} - 1 < 0 \tag{4.12}$$

where $r_f = \frac{V_f}{V_{total}}$ is the ratio of the volume of fluid and the total volume of the computational domain, while $r_{f,target}$ is the target fluid volume ratio, here equal to 0.63. The Spalart-Allmaras turbulence model and its adjoint were used here. No boiling is accounted for. The α field is regularized through a Helmholtz-type filter [120] and then sharpened with a smooth Heaviside function [121], resulting in the so-called β field.

4.2.3 Optimization results

The results of the optimization in terms of evolution of the normalized objectives and the weighted one, as a function of the optimization cycles, are reported in Figure 4.13a. Both cost functions are decreasing rapidly in the first few optimization cycles. The behavior of the weighted cost function results from the higher weight of $stdev(T)$, compared to the one used for T_{mean} in Eq. 4.10, and shows a very slow decrease after the first optimization cycles, despite a decrease in T_{mean} is still appreciable up to 60 cycles. In Figure 4.13b, the evolution of the constraints throughout the optimization is reported. It is shown that the constraints are satisfied after 50 cycles, since all the computed values after that cycle are negative for the fluid volume ratio, while the obtained value is oscillating around 0 for the pressure drop.

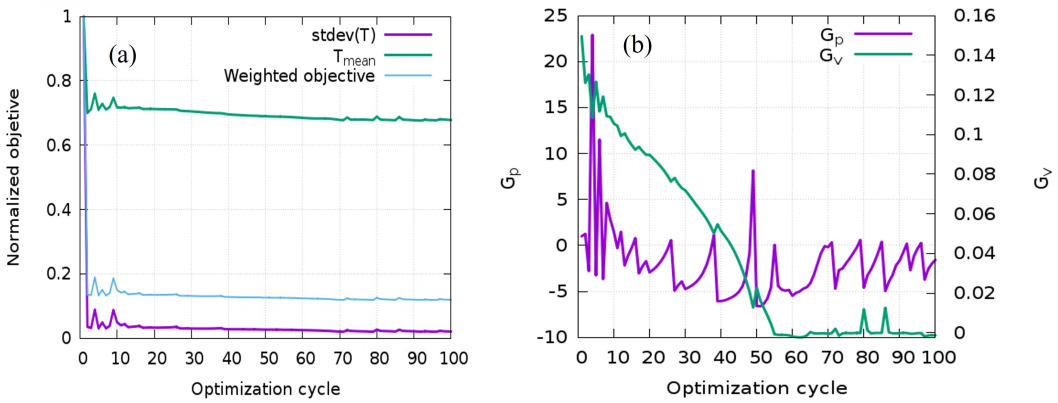

Fig. 4.13 (a) Evolution of the normalized objective functions and weighted normalized objective function with the optimization cycles. (b) Evolution of the constraints on the pressure drop (left axis) and fluid volume ratio (right axis) with the optimization cycles. Taken from [110].

The fluid domain computed at the end of 100 optimization cycles is shown in Figure 4.14. It is constituted by the domain in which the β field has values between 0 and 0.5. The fluid behaves almost symmetrically in the two inlet manifolds, as expected (the small asymmetries in the result could be attributed to lack of machine-accurate convergence of the flow solver due to small-scale oscillations). The azimuthal flow to the outlet manifold is mainly concentrated in the middle of the heated zone, corresponding to the heat flux peak.

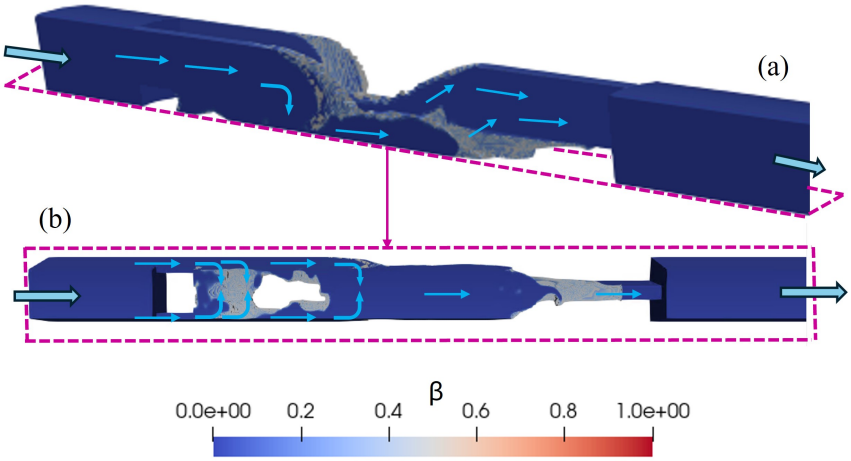

Fig. 4.14 Result of the adjoint topology optimization of after 100 cycles: (a) perspective views; (b) bottom view. Only the region with β field from 0 to 0.5 is represented, and it is the starting geometry for the fluid region after a proper separation from the solid part using isosurface method. The solid is the complementary. Taken from [110].

4.2.4 Flow fields and thermal analysis with a body-fitted mesh

The fluid and solid computational domains resulting from the optimization procedure have been extracted using the β=0.5 isosurface, allowing to obtain a final smooth geometry. Then, a conjugate heat transfer (CHT) simulation has been performed with a body-fitted mesh, allowing to have the actual boundary conditions at the solid-fluid interface, using again the Spalart-Allmaras turbulence model. The computed fluid flow fields are represented in Figure 4.15. In Figure 4.15.a 4.15.b the streamlines of the velocity field are reported, for a transversal and bottom view respectively, where a maximum velocity of 7.5 m/s is observed. This value is still far from the one evaluated in annular configuration of the BBO (described in subsection 3.1.2, which reaches maximum values of $\sim$30 m/s. The total pressure fields in Figure

4.15.c highlight the localized pressure drop at the level of the longitudinal manifold inlet/outlet from/to the main manifolds.

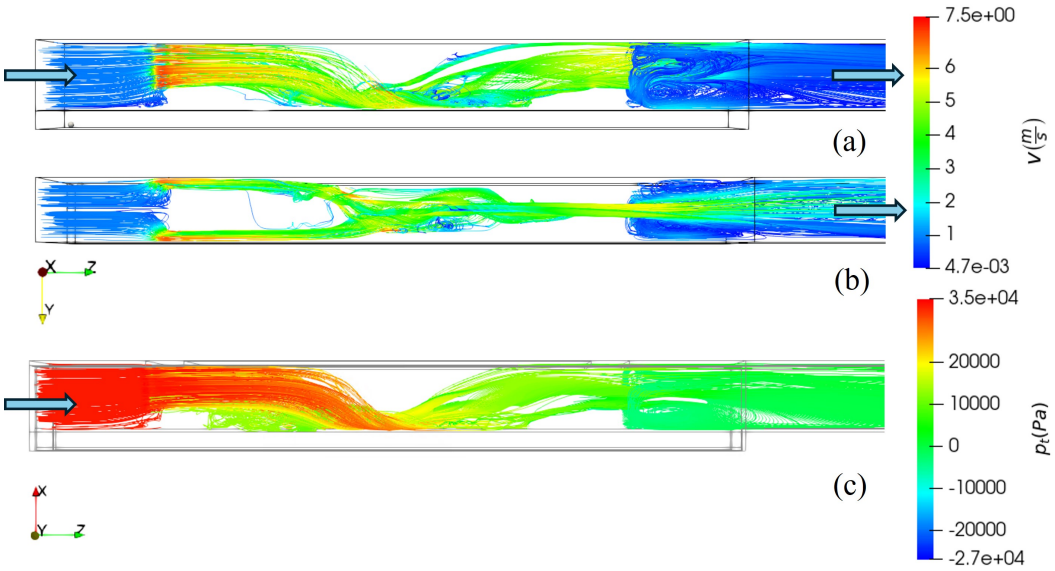

Fig. 4.15 Computed velocity field, in a) transversal and b) bottom view and total pressure field c) for the CHT problem solved in the optimized geometry with a body-fitted mesh. Taken from [110].

The effect of the optimization on the computed temperature profile of the heated surface in the longitudinal direction is shown in Figure 4.16.a, compared to the distribution obtained before the optimization (both normalized to the peak value of the latter). The reduction in temperature peak is $\sim 70\%$.

If the result of the optimization performed here is compared to that performed using a BBO, the max. temperature obtained in the current study is $\sim$30% higher than that in [98] (see Figure 4.16 7b). Notice, however, that here the computed total pressure drop along the geometry is only 0.33 bar, in contrast to [98] where it is $\sim$3 bar as it was not set as a constraint; hence, the larger heat transfer obtained in [98] comes at the cost of a much higher total pressure drop. If the optimization here was performed with a less strict constraint on the pressure drop, the temperature peak would have been closer to that in [98]. As far as the manufacturability of the two solutions is concerned, the large heat transfer in [98] is obtained by the engineering solution of a very small duct width, that could be difficult to manufacture.

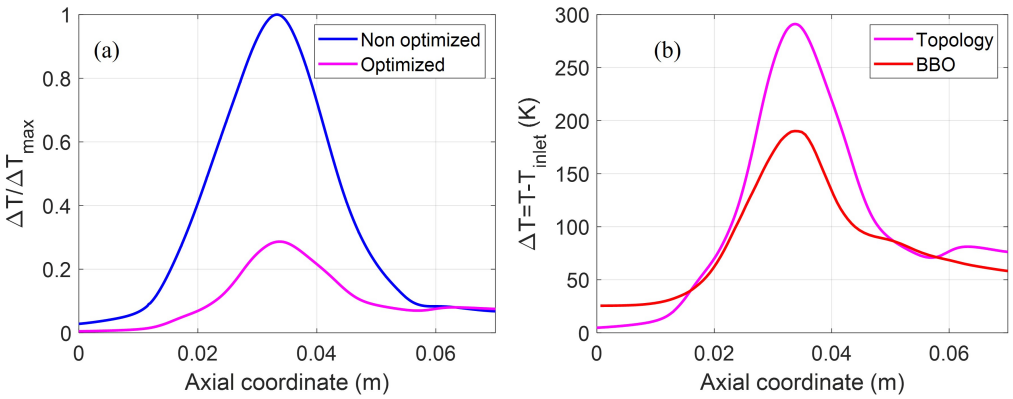

Fig. 4.16 Temperature difference in the heated surface with respect to fluid inlet, averaged in the azimuthal direction, (a) computed for the non-optimized (blue line) and optimized (magenta line) geometries, both normalized to the peak value of the former; (b) computed after the optimization by adjoint and BBO [98]. Taken from [110].

Chapter 5

Experimental activities and model validation

Another important branch of the research activity conducted during the PhD concerns experimental campaigns on different cavity mock-ups and the comparison of measurements with simulations results. The MCs cooling solution is the actual preferred one as an alternative to the RRs solution, with advances made in the last years on the design and technological processes for the manufacturing. For this reason testing mock-ups equipped with a MC cooling system is of great importance for Thales and the European research community working on gyrotrons, aiming to improve the tube characteristics. Hence, all the experimental analysis proposed here involve cavity mock-ups equipped with MCs.

The evaluation of the performance of such MC cooling system is a combined fluid dynamics and heat transfer phenomenon which seeks more attention to a highly accurate computational analysis. This is needed not only in view of a performance prediction, but also for design and optimization of future gyrotron cavities. In this chapter, hence, sections 5.1 and 5.3 discuss the validation of the pure hydraulic and the thermal-hydraulic parts respectively, for the numerical model used in this dissertation. Section 5.2 presents the hydraulic performance verification of the improved MC design described in section 3.2.1, using the validate model of section 5.1, but a different test facility. Furthermore, a detailed uncertainty quantification is reported regarding the measurements and the numerical results.

Portions of the present chapter were already published in the following scientific papers:

- A. Allio, R., Difonzo, A. Leggieri, F. Legrand, R. Marchesin and L. Savoldi, "Test and Modeling of the Hydraulic Performance of High-Efficiency Cooling Configurations for Gyrotron Resonance Cavities", *Energies*, vol. 13(5), 2020. [49]
- R. Difonzo, E. Gajetti, L. Savoldi and N. Fathi, "Assessment of different RANS turbulence models in mini-channels for the cooling of MW-class gyrotron resonators", *International Journal of Heat and Mass Transfer*, vol. 193,pp. 122922, 2022. [50]
- S. Stanculovic, R. Difonzo, A. Allio, K.A. Avramidis, P. Brücker, G. Gantenbein, S. Illy, J. Jelonnek, P.C. Kalaria, M. Misko, T. Rzesnicki, L. Savoldi, "Calibration of the KIT test setup for the cooling tests of a gyrotron cavity full-size mock-up equipped with mini-channels", *Fusion Engineering and Design*, vol. 172, pp. 112744, 2021. [51]

Part of the work of this chapter has been carried out within the framework of the EUROfusion Consortium, founded by the European Union via the Euratom Research and Training Programme, (Grant Agreement No 101052200 — EUROfusion), within the Work Package HCD. The views and opinions expressed are those of the authors' only and do not necessarily reflect those of the European Union or the European Commission. Neither the European Union nor the European Commission can be held responsible for them.

5.1 Hydraulic model validation on straight MC mock-up

For cooling applications, where the high speed of the fluid is utilized to enhance and ameliorate the heat transfer, hydro-dynamic phenomena play a key role and a reliable modeling and simulation of the fluid-dynamics is required to accurately predict the cooling efficiency, especially when turbulence is experienced in the system. Since a wide range of turbulence models is available, a careful selection of the turbulence

closure to be used in the simulations is very important to achieve more reliable results. This becomes even more significant when the numerical models are used not only to interpret the experimental results, but also as design tools. This is exactly the case of the application at hand here, for which several numerical analyses are ongoing [37] [122] [123], in order to optimize the MC cooling configuration for the gyrotron cavities. The choice of a reliable turbulence model is here the first step toward a robust model in terms of evaluation of the hydraulic behaviour of the cavity, that is in turn the basis for a reliable evaluation of its thermal and mechanical behaviour. For a component with water turbulent flow in circular mm-size channels, no studies are currently available that compare the performance of different turbulence models to experimental data, and allow a well-educated selection among them. In order to experimentally validate the MC cooling concept, a mock-up with the cavity equipped with mini-channels has been manufactured by Thales, the leading manufacturer of gyrotrons in Europe. The mock-up, shown in Figure 5.1.a has been tested at the Thales premises in summer 2019 to measure and evaluate its hydraulic characteristics [49].

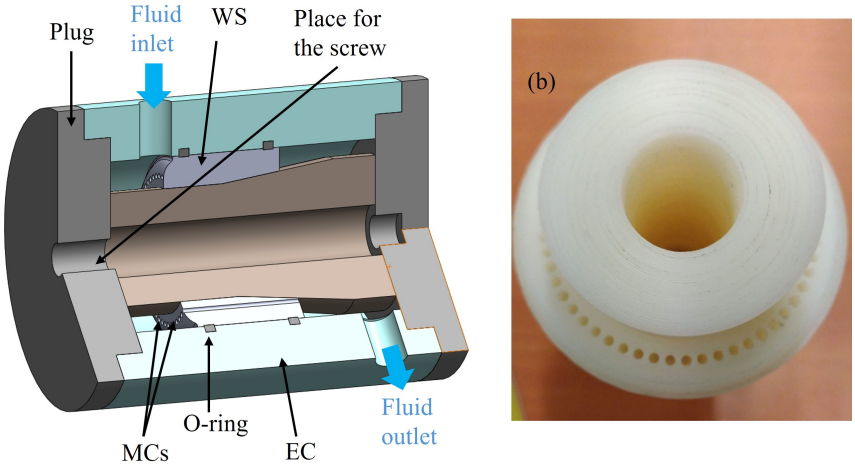

Fig. 5.1 (a) CAD sections of the mock-up of the cavity resonator in brown with straigth MCs drilled in the water stopper in light gray and(b) picure of the nylon cavity and water-stopper with straight MCs

The aim of the investigation presented in this section is therefore to compare the performance of various types of Reynolds-average Navier Stokes (RANS) turbulence models to evaluate the pressure drops along the gyrotron cavity equipped with a MC cooling system. Among the RANS available models in standard CFD commercial

software packages such as STAR-CCM+, specific models are selected as the more suitable models and approaches for the analysis of the case at hand, and namely the cavity mock-up previously mentioned. The computational results from the models applied in this work are validated against the experimental data measured on the MC mock-up tested at Thales. The validation is performed using a multivariate metric which allows accounting for the correlation among different set points, according to the approach proposed by the American Society of Mechanical Engineering (ASME) V&V20 Committee [124]. The comparison of the different models against the experimental results allows the selection of the most suitable model, in terms of accuracy of the results, for the simulation of the cavity equipped with MC, at least as far as the pure hydraulic problem is concerned. To further validate the adopted methodology, the same multivariate study was preliminary performed on a smooth pipe, comparing numerical results with correlations [50].

5.1.1 Selection of RANS turbulence models

The hydraulic simulations of the MC cooling system are performed using the commercial software Star-CCM+. Among the many RANS models available in the software, the selection of the most suitable RANS turbulence closures for the simulation of the gyrotron cavity equipped with MCs boils down to three models: *Realizable* $\kappa-\varepsilon$, $\kappa-\omega$ *SST* and *Lag Elliptic Blending* (*EB*) $\kappa-\varepsilon$. The choice has been taken by selecting the most new and performative model out of the two main classes of RANS, leading to select the *Realizable* $\kappa-\varepsilon$ [125], more suitable for application that contains multiple recirculation zones or large streamline curvature than standard version [126], for the $\kappa-\varepsilon$ family, and the $\kappa-\omega$ *SST* [127] out of the $\kappa-\omega$ family, capable to capture not only the near-wall behaviour, but also the core fluid flow. The *Lag EB* $\kappa-\varepsilon$ [128], which is a four equations extension of the $\kappa-\varepsilon$ was selected since it is more recent and with promising prediction for heat transfer problems.

In the general turbulence modelling framework, it is useful to define some invariants related to velocity gradients before proceeding to the description of the characteristic equations: those are the strain rate tensor and the vorticity tensor, defined respectively in Eq. 5.1 and Eq. 5.2. In the following their moduli will be referred to as s and w.

Table 5.1 Turbulent time scale τ for the different models.

Turbulence model	τ
Relizable $\kappa-\varepsilon$	$\frac{\kappa}{\varepsilon}$
$\kappa-\omega$ *SST Menter*	$min\left(\frac{1}{max\left(\frac{\omega}{a^*},\frac{SF_2}{a_1}\right)},\frac{C_t}{\sqrt{3}S}\right)$
Lag EB $\kappa-\varepsilon$	$\sqrt{\left(\frac{\kappa}{\varepsilon}\right)^2+\frac{C_t^2\nu}{\varepsilon}}$

$$s=\frac{1}{2}(\nabla\overline{v}+\nabla\overline{v}^T) \tag{5.1}$$

$$w=\frac{1}{2}(\nabla\overline{v}-\nabla\overline{v}^T) \tag{5.2}$$

More specifically, the two transport equations added to the standard *RANS* equations have the form of Eq. 5.3, where Γ is the transported quantity, i.e. the turbulent kinetic energy κ and the turbulent dissipation rate ε for the $\kappa-\varepsilon$ models, or turbulent specific dissipation rate ω for the $\kappa-\omega$ models. P_Γ and Ω_Γ are production and source terms, whereas Λ is an additional contribution, specific for each model and transported quantity and ζ_Γ is a model coefficient (σ in STAR-CCM+).

$$\frac{\partial(\rho\Gamma)}{\partial t}+\nabla\cdot(\rho\Gamma\overline{v})=\nabla\cdot\left[\left(\mu+\frac{mu_t}{\zeta_\Gamma}\right)\nabla\Gamma\right]+P_\Gamma+\Lambda+\Omega_\Gamma \tag{5.3}$$

In the *Realizable* $\kappa-\varepsilon$ model the turbulent eddy viscosity μ_t is defined as function of the density, of the turbulent kinetic energy and of the turbulent time scale (τ) (turbulent time scales for the three models can be found in Table 5.1), multiplied by a coefficient C_μ and a variable damping function F_μ, which simulates the turbulence decrease near wall. The damping function embeds also the strain rate tensor, the vorticity tensor, κ and ε.

The extra term Λ is depicted in Table 5.2 for the *Realizable* $\kappa-\varepsilon$ model, as well as for the other models used in this analysis. Therein, ε_0, κ_0, ω_0 are ambient turbulent values counteracting turbulent decay while definition of the specific time scale t_0 depends on them. The model coefficients are reported in Table 5.3 (notice that the coefficient Υ is usually indicate with β in the literature).

Table 5.2 Λ for the different models.

Turbulence model	Γ	Λ
Relizable $\kappa-\varepsilon$	κ	$-\rho(\varepsilon-\varepsilon_0)$
	ε	$\frac{\varepsilon}{\kappa}C_{\varepsilon 1}P_\varepsilon - C_{\varepsilon 2}\frac{\kappa}{\kappa+\sqrt{\nu\varepsilon}}\rho\left(\kappa-\frac{\varepsilon_0}{t_0}\right)$
$\kappa-\omega$ *SST Menter*	κ	$-\rho\Upsilon^*(\omega\kappa-\omega_0\kappa_0)$
	ω	$-\rho\Upsilon(\omega^2-\omega_0^2)$
Lag EB $\kappa-\varepsilon$	κ	$-\rho(\varepsilon-\varepsilon_0)$
	ε	$\frac{\varepsilon}{\kappa}C_{\varepsilon 3}P_\varepsilon - C_{\varepsilon 4}\rho\left(\kappa-\frac{\varepsilon_0}{t_0}\right)$

The production terms P_ε and P_κ depend only on the turbulent production, mean strain rate and turbulent kinetic energy, as neither the buoyancy production neither the compressibility modification are relevant for this problem. Both production terms also contain a curvature correction factor, which could help accounting, in the problem at hand, for the curvature of the fluid moving in the manifold orthogonal to the mini-channels before entering them.

The *Shear* $-$ *Stress Transport* (*SST*) $\kappa-\omega$ model [21] is a two-equations eddy-viscosity model which combines the $\kappa-\varepsilon$ and the $\kappa-\omega$ models through a blending function that activates the first one in the free stream and the second one near the wall. It offers good performance typically when the accurate simulation of the viscous sub-layer comes with the need for accurately predicting the flow behavior in regions away from the wall [20]. Eq. 5.3 is thus defined for both κ and ω, for which the production terms P_κ and P_ω are composed by turbulent production, non-linear production, specific dissipation production and cross diffusion. Similar to the $\kappa-\varepsilon$ case, the turbulent viscosity depends just on density, turbulent kinetic energy and on $\kappa-\omega$ model-specific turbulent time scale (see Table 5.1). In the definition of τ, F_2 is a blending function embedding in its formulation, beside ω and κ, the distance to the wall, that enables the switching between the two different models, which is peculiar of the *SST* $\kappa-\omega$ model. The model coefficients a^*,a_1 and C_T are defined in Table 5.4, where F_1 is another blending function behaving similarly to F_2 with the addition of a cross diffusion coefficient between κ and ω.

In the *Lag EB* $\kappa-\varepsilon$ model [22] a transport equation for the reduced normal stress ϕ is added to the transport equations for κ and ε, which allows the misalignment of the principal axes of the strain-rate and the Reynolds-stress (the "lag" between

Table 5.3 *Realizable* $\kappa-\varepsilon$ Two-layer model coefficients in Star-CCM+

C_t	1
$C_{\varepsilon 1}$	$max\left(0.43, \frac{\frac{S\kappa}{\varepsilon}}{5+\frac{S\kappa}{\varepsilon}}\right)$
$C_{\varepsilon 2}$	1.9
C_μ	0.09
ζ_ε	1.2
ζ_κ	1

Table 5.4 $\kappa-\omega$ *SST* model coefficients in Star-CCM+

a^*	$F_1+(1+f_1)$
β	$0.075F_1+0.0828(1-F_1)$
β^*	$0.09[F_1+(1-F_1)]$
$\zeta_{\kappa 2}$	$F_1+0.85(1-F_1)$
ζ_ω	$0.5F_1+0.856(1-F_1)$
a_1	0.31
C_t	0.6

stress and strain) while still using a linear eddy-viscosity model, depending not only on ρ, κ and τ but also on ϕ and s. It is suitable for incorporating curvature and rotation effects. A small correction to the diffusive term in Eq. 5.3 leads to the general formulation of transport equations for this specific model as in Eq. 5.4.

$$\frac{\partial(\rho\Gamma)}{\partial t}+\nabla\cdot(\rho\Gamma\overline{v})=\nabla\cdot\left[\left(\frac{\mu}{2}+\frac{mu_t}{\zeta_\Gamma}\right)\nabla\Gamma\right]+P_\Gamma+\Lambda+\Omega_\Gamma \tag{5.4}$$

In Eq. 5.3, the only contribution to P_ε and P_κ is the turbulent production while P_ϕ also contain the Reynolds-stress anisotropy tensor. The latter combines the strain rate tensor and a modified vorticity tensor (Eq. 5.5) to account for anisotropy, that on the contrary is not considered in the pure 2-equations models such as $\kappa-\varepsilon$ and $\kappa-\omega$.

$$\hat{w}=w-\frac{1}{s^2}\left(s\frac{D_s}{D_t}-\frac{D_s}{D_t s}\right) \tag{5.5}$$

A further diffusion equation for the elliptic blending factor φ is included to the set of equations of the Lag Elliptic Blending $\kappa-\varepsilon$ model, as reported in Eq. 5.6, where l_t is the turbulent scale.

Table 5.5 *Lag EB* $\kappa-\varepsilon$ model coefficients in Star-CCM+

$C_{\varepsilon 3}$	1.44
$C_{\varepsilon 4}$	1.9
ζ_{ε}	1.2
ζ_{κ}	1
ζ_{φ}	1

$$\nabla \cdot (l_t^2 \nabla \varphi) = \varphi - 1 \tag{5.6}$$

The coefficients for the *Lag EB* $\kappa-\varepsilon$ model are reported in Table 5.5.

5.1.2 Validation approach

In order to compare various types of turbulence models, the quantification of the uncertainties was performed to characterize the numerical results and their errors using the ASME V&V 20-2009 Standard [129]. The first uncertainty is the numerical one due to the mesh size, u_{num}, which is quantified by performing a convergence study. The second uncertainty, u_{input}, represents the effect of the input uncertainties on the computed results. The input uncertainty, u_{input}, is evaluated by mean of a local method which means that the sensitivity coefficients of each parameter affected by uncertainty are evaluated and combined for the computation of u_{input} as explained in [129]. The last uncertainty u_D comes from the experimental data. Once these quantities are computed, it is possible to compare simulations and experimental results, each with its own uncertainties, at each set point. Here all the uncertainties of all the set points are combined in a multivariate metric, namely E_{mv}, allowing to compare the three turbulence models using a single index. According to [124], E_{mv} is obtained from Eq. 5.7.

$$E_{mv}^2 = E^T V_{val}^{-1} E \tag{5.7}$$

Here E is the vector of the comparison errors of the n set points considered in the analysis, see Eq. 5.8, and V_{val} is the covariance matrix, which is used to characterize the correlation structure between the estimated uncertainties.

$$E = \begin{bmatrix} S_1 - D_1 \\ \vdots \\ S_n - D_n \end{bmatrix} \tag{5.8}$$

In Eq. 5.8, S_j and D_j are the simulation results and experimental data of the j-th set point, respectively. The covariance matrix, V_{val}, contains the numerical uncertainties, simulation input uncertainties and uncertainties in the measured data. As proposed in [124], when simulation and measurement data are independent, i.e. sharing no error sources, V_{val} is evaluated using Eq. 5.9, where V_{num}, V_{input} and V_D are the covariance matrices due to numerical uncertainties, simulation input uncertainties and uncertainties in the measured data, respectively.

$$V_{val} = V_{num} + V_{input} + V_D \tag{5.9}$$

The diagonal elements of V_{num}, V_{input} and V_D are the square of u^2_{num} ,u^2_{input} and u^2_D obtained for each set point, while the off-diagonal elements represent the correlation between the estimated numerical / input/ data uncertainties and are illustrated below.

5.1.3 Experimental results and their uncertainty quantification

The test loop for the mock-up hydraulic measurements is constituted by a pump, connecting pipes, a filter for the water and the mock-up, see Figure 5.1.a for a sketch of the loop. The mock-up includes a nylon prototype of the gyrotron resonator equipped with mini-channels including the so called water-stopper (WS) (Figure 5.1.b), an external rigid cylindrical envelope (EC) , two plugs to close the envelope at top and bottom, one screw, and two hydraulic connectors to link the mock-up to the test loop, see Figure 5.1. The resonator and water-stopper were made using a lathe machine in a single piece of nylon. The MCs were realized using a high-precision drilling machine. Because of the use of traditional machining methods, the MCs had a more conventional circular section, with a diameter of 1.9 mm and a pitch of $\sim$3 mm. They did not follow the profile of the external wall of the cavity, resulting axially straight, as shown in Figure 5.1. The EC was made of Plexiglass, and its internal radius was slightly larger than the external one of the water-stopper in order to allow

the insertion of the cavity. Two O-rings were inserted into two slots drilled into the Plexiglass, according to the WS position, in order to lock the cavity in the mock-up and prevent the water from going into the empty space between the WS and the EC, as shown in Figure 2a. Two cylindrical holes were realized in the EC, where the two hydraulic connectors were inserted, to insert the mock-up in the test loop used for the hydraulic measurements. The two aluminum plugs were realized to hold the cylinder, and they were tightly connected by the screw which traversed the entire mock-up (see Figure 5.1), in order to ensure that no water could flow inside the inner volume.

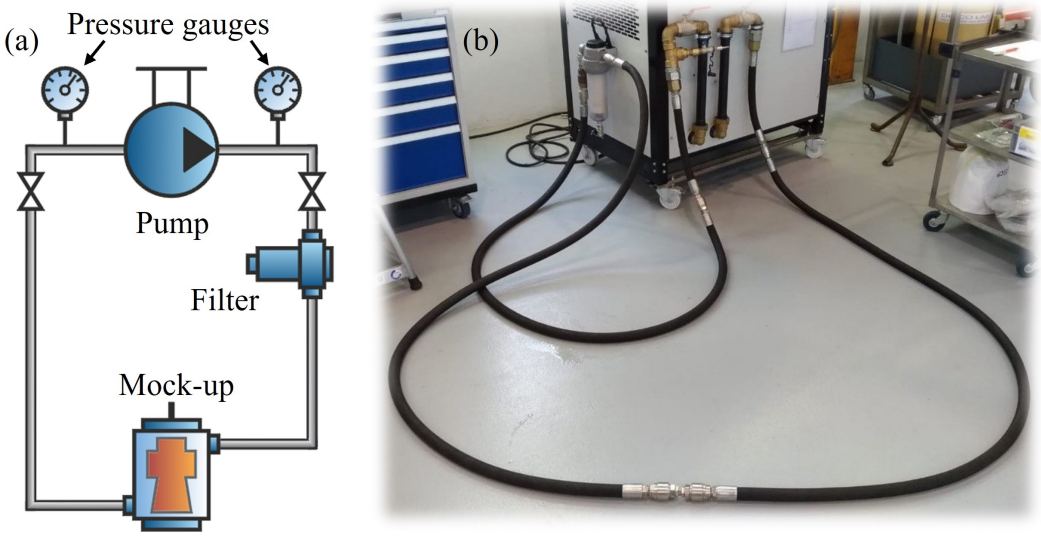

Fig. 5.2 (a) Sketch of the circuit for the hydraulic tests of the resonator mock-up and (b) loop configuration for the calibration tests: the pipes are connected with an hydraulic connector. Taken from [50].

The loop instrumentation consisted of two absolute pressure gauge, located upstream and downstream of the pump, and a flow meter, located downstream of the mock-up. During the experimental measurements, the water flow rate was varied from 30 to 80 l/min (to give turbulent flow in the MCs) and the pressure drop of the loop piping, filter, and the mock-up all together (Δp_{tot}) was measured at each flow rate as the difference of the pressure read-outs measured by the two absolute pressure gauge. After that, in order to calibrate the loop, the mock-up was removed, and the pressure drop of the short-circuited loop only (Δp_{loop}) was measured again as the difference between the two manometer read-outs, in the configuration shown in the picture in Figure 5.2.b. In order to obtain the hydraulic characteristic of the mock-up

(Figure 5.3), for any value of the flow rate the loop pressure drop was subtracted from overall pressure drop following Eq. 5.10

$$\Delta p = \Delta p_{tot} - \Delta p_{loop} = (p_{tot,in} - p_{tot,out}) - (p_{loop,in} - p_{loop,out}) \tag{5.10}$$

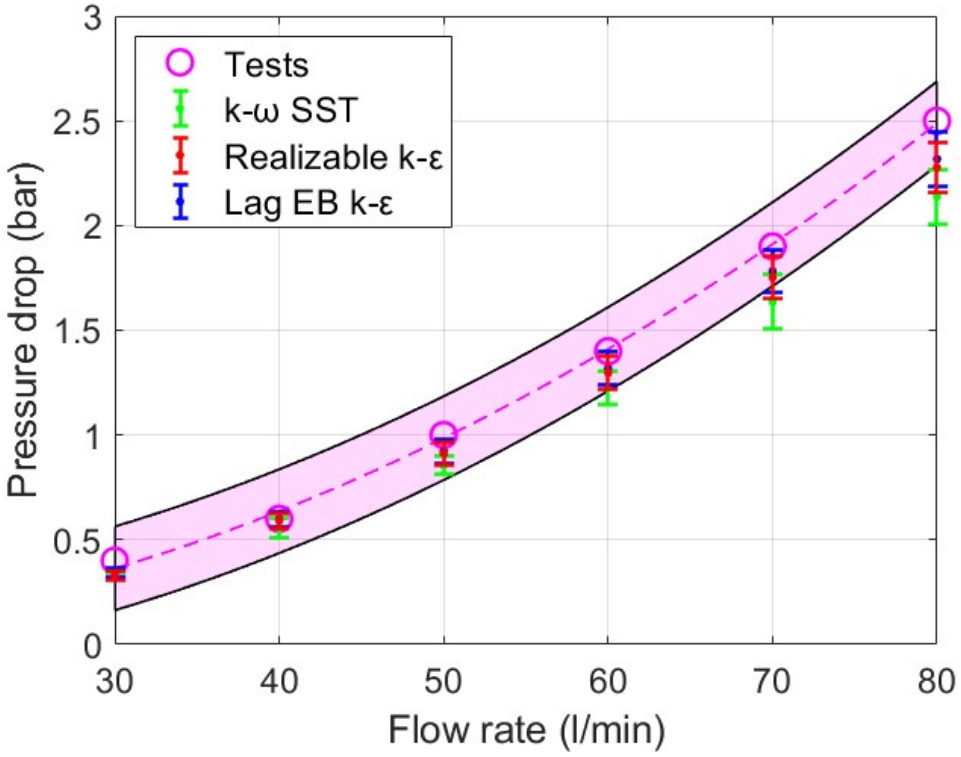

Fig. 5.3 Measured hydraulic characteristic of the mock-up (dashed line), Compared to the computed results obtained using the different turbulence models. The uncertainties are reported for both the measurement data and the computed points.

The uncertainty of the experimental data has been evaluated by combining the uncertainties of all the measured variables contributing to the mock-up pressure drop calculation in the data reduction equation Eq. 5.10. The pressure gauge uncertainty, given by the manufacturer, is $u_{X_i} = 0.1bar$. The uncertainties of each pressure measurement fo each set point are considered uncorrelated, giving the experimental pressure drop uncertainty u_D as the square root of Eq. 5.11, obtained using the uncertainty propagation law of all the measurement constituting the data

reduction equation. The resulting pressure drops and their uncertainties are reported in Figure 5.3

$$u_D^2 = \sum_{i+1}^{n} \left(\frac{\partial \Delta p}{\partial X_i} u_{X_i} \right) = \left(\frac{\partial \Delta p}{\partial p_{tot,in}} u_{p_{tot,in}} \right)^2 + \left(\frac{\partial \Delta p}{\partial p_{tot,out}} u_{p_{tot,out}} \right)^2 + \\ + \left(\frac{\partial \Delta p}{\partial p_{loop,in}} u_{p_{loop,in}} \right)^2 + \left(\frac{\partial \Delta p}{\partial p_{loop,out}} u_{p_{loop,out}} \right)^2 \tag{5.11}$$

5.1.4 Simulation set-up, its uncertainty quantification and computed results

A 3D, steady-state computational model was adopted. Taking advantage of symmetry of the geometry, only half domain of the mock-up was simulated (see Figure 5.4.a), to reduce the computational cost. Constant properties for the fluid (water) at room temperature have been considered since in the test conditions the fluid temperature remains almost constant. A mass flow rate boundary condition was imposed on the fluid inlet (see Figure 5.4.a), using the values measured with the flow meter during the experiments. The boundary condition is translated in a constant velocity all over the inlet boundary. Also for the inlet temperature, an averaged value from the ones measured during the experiments, is used: 27 ^{o}C. At the outlet boundary face the relative pressure is specified. On the symmetry planes (in green in Figure 5.4.a) a symmetry boundary condition is imposed, which means that the normal velocity and the normal gradients of all other variables are zero. Concerning the turbulent variables, for all the selected turbulence closures, constant values were imposed on the inlet while zero gradient condition is imposed on the outlet.

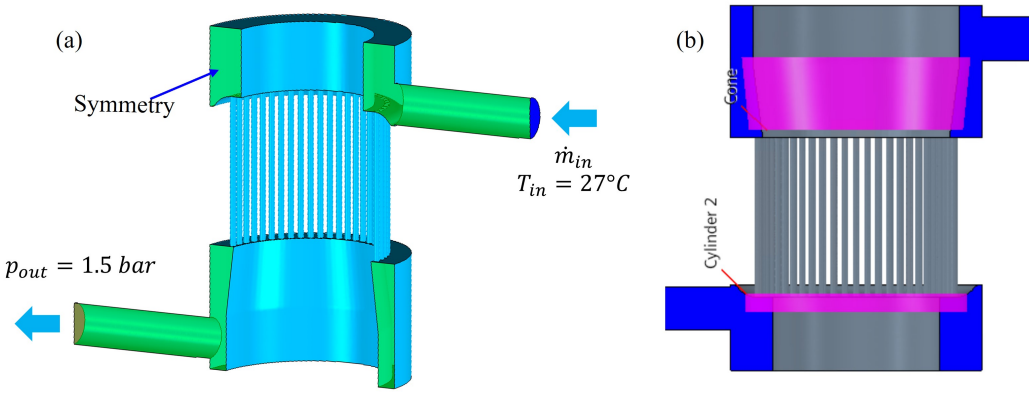

Fig. 5.4 (a) Computational domain and boundary conditions for the fluid domain under investigation. Cyan surfaces are walls. (b) Subdivision of the three different zones of mesh refinement of the computational domain. The pink areas are characterized by the middle base size.

The polyhedral mesh was used for the simulations by subdividing the domain in three zones of refinement, as shown in Figure 5.4.b. The first zone includes the inlet and outlet pipes and the two manifolds and is characterized by the largest base size, equal to 0.6 mm, and 6 prism layers with a total thickness of the prism layer of 0.4 mm. The first refinement affects the two zones upstream and downstream of the MCs and is characterized by a base size of 0.5 mm. The third area is that of the MCs, characterized by the smallest cell size as it is shown in Figure Figure 5.5.b, with a base size of 0.12 mm and 12 prism layers with a total thickness of 0.2 mm. Prism layers have been used for the wall treatment and the thickness of the first layer has been chosen to give $y^+ \sim 1$ to cover the highest flow rate. A 3D representation of the finest mesh for the entire domain is reported in Figure 5.5.

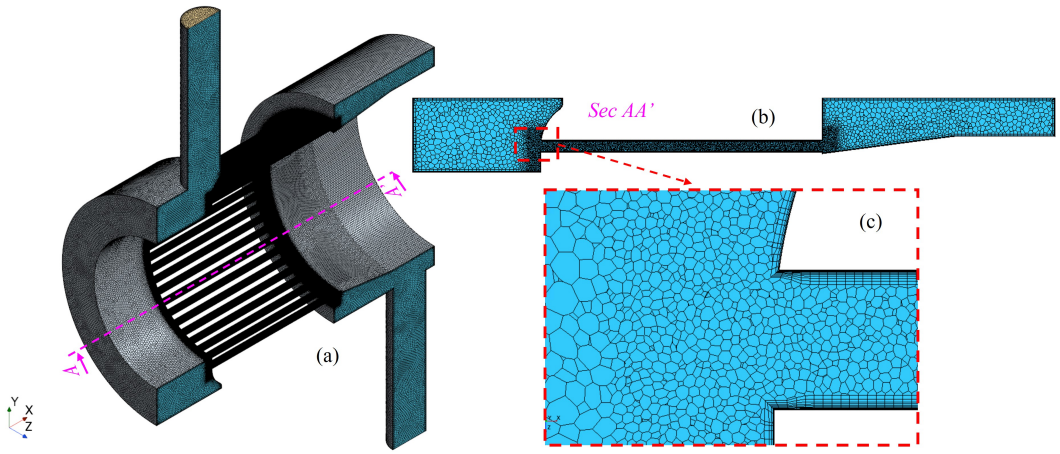

Fig. 5.5 (a) 3D finest mesh (b) transversal section of the mesh and (c) zoom on the mini-channel inlet. Taken from [50].

In Figure 5.6 the velocity maps in a longitudinal section of the mock-up are reported for the three turbulence models analyzed in this study, at 50 l/min of flow rate, being the nominal flow rate. With respect to the others, the $\kappa - \omega$ SST model presents on the longitudinal cross sections, taken at 90^o from the inlet (Sec. BB' in Figure 5.6) a higher velocity near the manifold wall, also corroborated with the velocity maps on the transverse section (Sec. AA' in Figure 5.6). At the same time, it shows a larger inlet effect in the MCs with the tendency to a swirl flow within the channels that is not so evident in the $\kappa - \varepsilon$ models. At the channel outlet, the $\kappa - \omega$ SST model presents a faster exit of the velocity with larger re-circulation loops in the outlet manifold.

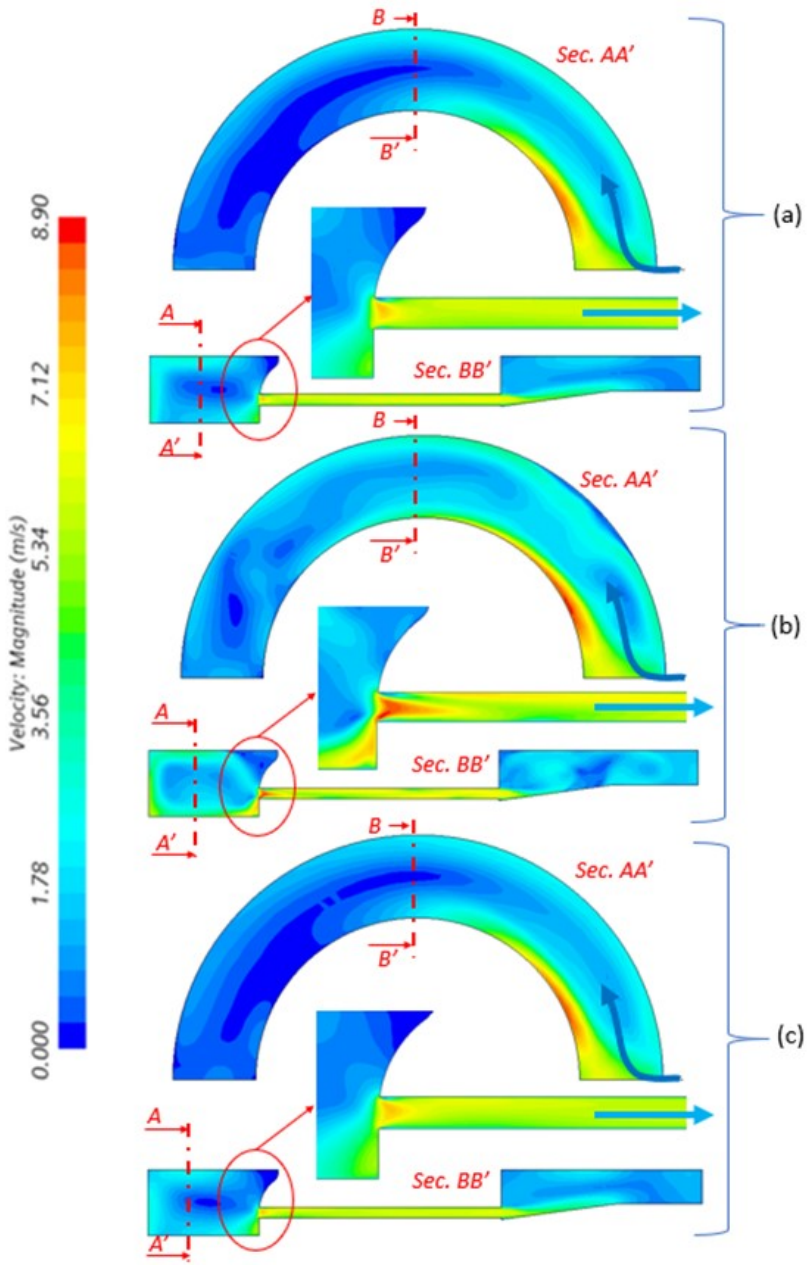

Fig. 5.6 Velocity maps on one longitudinal and transverse section of the mock-up, for the three turbulence models: (a) Realizable $\kappa - \varepsilon$, (b)$\kappa - \omega$ SST and (c) Lag EB $\kappa - \varepsilon$. Taken from [50].

.

The mock-up pressure drop values are reported in Figure 5.3 comparing the simulations and experimental results with their associated uncertainties at each set point. While the results obtained from the Realizable $\kappa - \varepsilon$ and *LagEB* $\kappa - \varepsilon$ models

Table 5.6 Mesh parameters for GCI evaluation of the cavity mock-up pressure drops analysis.

Name	Entire Domain	Mini Channels		
	# of millions cells	# of millions	h (mm)	r_{i1}
1	9.75	6.05	0.152	1
2	6.31	3.726	0.179	1.12
3	3.56	2.05	0.219	1.37
4	2.77	1.63	0.236	1.47
5	1.97	1.04	0.274	1.71

fall within the experimental uncertainty for almost the entire flow rate range, the values coming from the $\kappa-\omega$ *SST* model show a consistent underestimation of the experimental vales. This mismatch grows in the $\kappa-\omega$ *SST* simulation results as the flow rate increases.

To evaluate the numerical uncertainty due to domain discretization, a grid convergence study was performed by progressively refining the area of the mini-channels only. Note that the mesh in the rest of the fluid was kept constant and previously defined in order to obtain mesh independent results. The characteristics of the meshes used in the numerical uncertainty assessment are listed in 5.6. The observed order of convergence of the results was evaluated by mean of a Least Square method according to Eqs. 5.12-5.16, considering only the pressure drop characterizing the area interested by the mesh refinement. To evaluate the Grid Convergence Index (GCI) and the numerical uncertainties of each set point, the observed order of convergence for the simulation of the entire the mock-up was assumed the same of the MCs.

It is assumed that the discretization error generated in this analysis can be expanded with respect to the exact value of the pressure drop in a one-term form in Eq. 5.12:

$$\Delta p_i - \Delta p_\infty \approx \gamma h_i^\theta \tag{5.12}$$

where Δp_i is the pressure drop computed using the $i-th$ mesh, Δp_∞ is the extrapolated value, θ is the observed order of convergence and γ is just a coefficient. Note that h_i is the average cell size computed as the cubic root of the ratio between the volume of the domain and the number of cells of the $i-th$ mesh, see Eq. 5.13.

$$h_i^{\theta} = \left(\frac{Volume}{N_{cells,i}} \right)^{\frac{1}{3}} \tag{5.13}$$

The terms Δp_{∞}, γ, θ can be found by minimizing the least squares function $\mathscr{L}$ defined in Eq. 5.14, in which n should be at least equal to 5.

$$\mathscr{L}(\Delta p_{\infty}, \gamma, \theta) = \sqrt{\sum_{i=1}^{n} (\Delta p_i - (\Delta p_{\infty} + \gamma h_i^{\theta}))^2} \tag{5.14}$$

From the computed order of convergence θ, the Grid Convergence Index GCI_j for each set point, i.e. flow rate in this case study, can be computed as in 5.15, and finally $u_{num,j}$ is evaluated from Eq. 5.16.

$$GCI_j = \frac{1.25 * er_{a,j}^{21}}{r_{21,j}^{\theta} - 1} \tag{5.15}$$

$$u_{num,j} = \frac{GCI_j}{1.15} \tag{5.16}$$

In Eq. 5.15, $er_{a,j}^{21}$ is the absolute error between the results using the finest mesh and the second finest mesh. $r_{21,j}^{\theta}$ is the ratio between the cell sizes of the finest mesh and of the second finest mesh and the factor 1.25 is suggested in [129].

The effect of the input parameter uncertainty on the global simulation uncertainty has been evaluated with reference to the inlet flow rate used as boundary conditions to the simulations, the uncertainty of which is taken as 0.5 l/min from the flow meter accuracy, and the channels diameter, affected by an uncertainty of 0.0005 m due to the manufacturing process, as shown in Figure 5.7. In order to quantify the effects of these two parameters, the sensitivity coefficients have been evaluated by adding and subtracting the uncertainty affecting each parameter in the different simulations, by following the local method procedure.

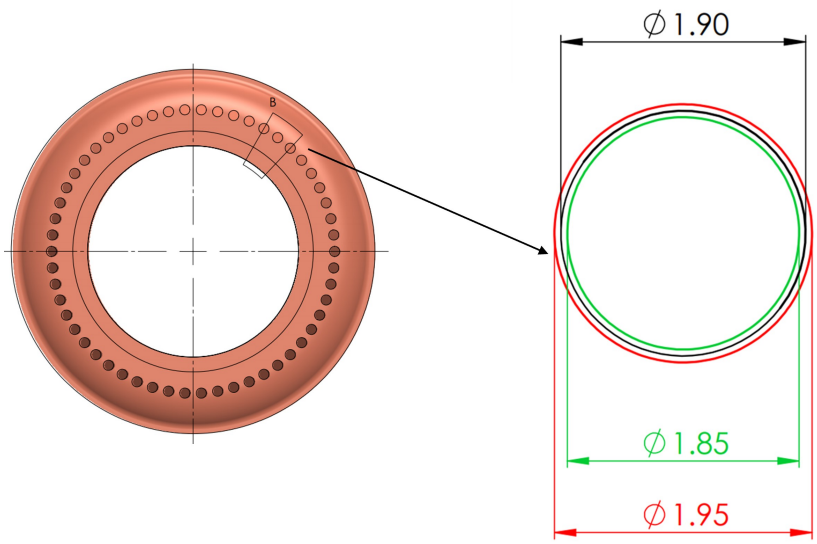

Fig. 5.7 : Channels diameters: in black the design diameter, in red and green the diameter obtained by adding and subtracting respectively the uncertainty, given by the manufacturing tolerance.This diameters are used to drive the simulation input uncertainty. Taken from [50].

5.1.5 Multivariate metric assessment

To check the effect of the correlation among different uncertainties on the final performance of the turbulence models, the multivariate metric assessment was performed as well, trying to identify how the uncertainties coming from the different sources interact. Here the validation variable of the study is the pressure drop along the mock-up, which is the result of a data reduction equation of the actual measured pressures, see Eq. 5.10. None of the pressure measurements, however, is affecting as an input the simulations, where constant water properties are used. In order to analyze the contribution of the correlations of the uncertainty among the different set points (i.e., the pressured drops evaluated at different water flow rates) on the final result, two cases are considered:

- *Case a)* in which the set points share no identical error source, and
- *Case b)* in which all set points share identical error source and the correlation among the different set point uncertainty is accounted for.

In *Case a*, the contribution of input simulation uncertainties and experimental uncertainties is evaluated neglecting any possible correlations as in Eq. 5.17, while for Case b Eq. 5.18 is used.

$$V_{input,D} = \begin{bmatrix} (X_{s,1} - X_{D,1}) V_{x,1} (X_{s,1} - X_{D,1})^T & 0 & 0 \\ 0 & \ddots & 0 \\ 0 & 0 & (X_{s,n} - X_{D,n}) V_{x,n} (X_{s,n} - X_{D,n})^T \end{bmatrix} \tag{5.17}$$

$$V_{input+D} = (X_s - X_D) V_X (X_s - X_D)^T \tag{5.18}$$

In Eq. 5.17 (*Case a*), $X_{s,j}$ is a vector containing the m sensitivity coefficients for the simulations corresponding to each parameter affected by uncertainty for the j-th set point. It is evaluated with Eq. 5.19 where the derivatives of the data reduction equation with respect to the different pressure measurements of the tests are null. $X_{D,j}$ is a vector containing the sensitivity coefficients for the data reduction equation for the j-th set point and is evaluated with Eq. 5.20. In this case the sensitivity coefficients evaluated for the flow rate and channels diameter uncertainty are null. $V_{x,j}$ is the covariance matrix of the $j-th$ set point containing the m uncertainties of each parameter affected by uncertainty where all the off-diagonal terms are zero since no measured variables share an error source (Eq. 5.21).

$$X_{S,j} = \begin{bmatrix} \frac{\partial S_j}{\partial x_1} & \cdots & \frac{\partial S_j}{\partial x_m} \end{bmatrix} = \begin{bmatrix} \frac{\partial \Delta p}{\partial \dot{m}} & \frac{\partial \Delta p}{\partial \Delta d} & \frac{\partial \Delta p}{\partial p_{out,tot}} & \frac{\partial \Delta p}{\partial p_{in,tot}} & \frac{\partial \Delta p}{\partial p_{out,loop}} & \frac{\partial \Delta p}{\partial p_{in,loop}} \end{bmatrix} \tag{5.19}$$

$$X_{D,j} = \begin{bmatrix} \frac{\partial D_j}{\partial x_1} & \cdots & \frac{\partial D_j}{\partial x_m} \end{bmatrix} = \begin{bmatrix} \frac{\partial \Delta p}{\partial \dot{m}} & \frac{\partial \Delta p}{\partial d} & \frac{\partial \Delta p}{\partial p_{out,tot}} & \frac{\partial \Delta p}{\partial p_{in,tot}} & \frac{\partial \Delta p}{\partial p_{out,loop}} & \frac{\partial \Delta p}{\partial p_{in,loop}} \end{bmatrix} \tag{5.20}$$

$$V_{x,j} = \begin{bmatrix} (u_{x,1}^2 & 0 & \dots & \\ 0 & u_{x,2}^2 & \dots & \\ \vdots & & \ddots & 0 \\ 0 & & & u_{num,m}^2 \end{bmatrix} \tag{5.21}$$

Considering *Case b)* the covariance of the inputs at the multiple set points is identical to *Case a)*. Therefore $V_{x,1} = \cdots = V_{x,n}$ and the covariance is evaluated using Eq. 5.21. The sensitivity matrixes are in turn defined by Eq. 5.22 and Eq. 5.23 where $X_{s,j}$ and $X_{D,j}$ are evaluated respectively with Eq. 5.19 and Eq. 5.20. The result of Eq. 5.18 is then a full matrix.

$$X_s = \begin{bmatrix} X_{s,1} \\ \vdots \\ X_{s,n} \end{bmatrix} \tag{5.22}$$

$$X_D = \begin{bmatrix} X_{D,1} \\ \vdots \\ X_{D,n} \end{bmatrix} \tag{5.23}$$

Further relevant values to be defined are the expected value $\sqrt{< E_{mv}^2 >}$ and the reference value E_{ref}. The latter allows estimating the mismatch between simulations and the experimental data. Considering the uncertainties of the applied turbulence models can be represented by normal distributions, E_{mv}^2 will be distributed as Chi-squared, $\chi^2(df)$, with the degrees of freedom, df, equal to the rank of V_{val}, which is 6 for the case under study, as stated in Eq. 5.24.

$$< E_{mv}^2 >= \chi^2(df) = df \tag{5.24}$$

For what concerns E_{ref}^2, it is defined in Eq. 5.25 as the sum of the expected value $< E_{mv}^2 >$ and its uncertainty range, represented by the standard uncertainty of the $\chi^2(df)$ distribution [124]:

$$< E_{ref}^2 >=< E_{mv}^2 > +\sqrt{var(E_{mv}^2)} = df + \sqrt{2df} \tag{5.25}$$

The values of the multivariate metric, E_{mv}, resulting from 5.7 for the three turbulence models are reported in Figure 5.8, together with E_{ref} and $\sqrt{< E_{mv}^2 >}$.

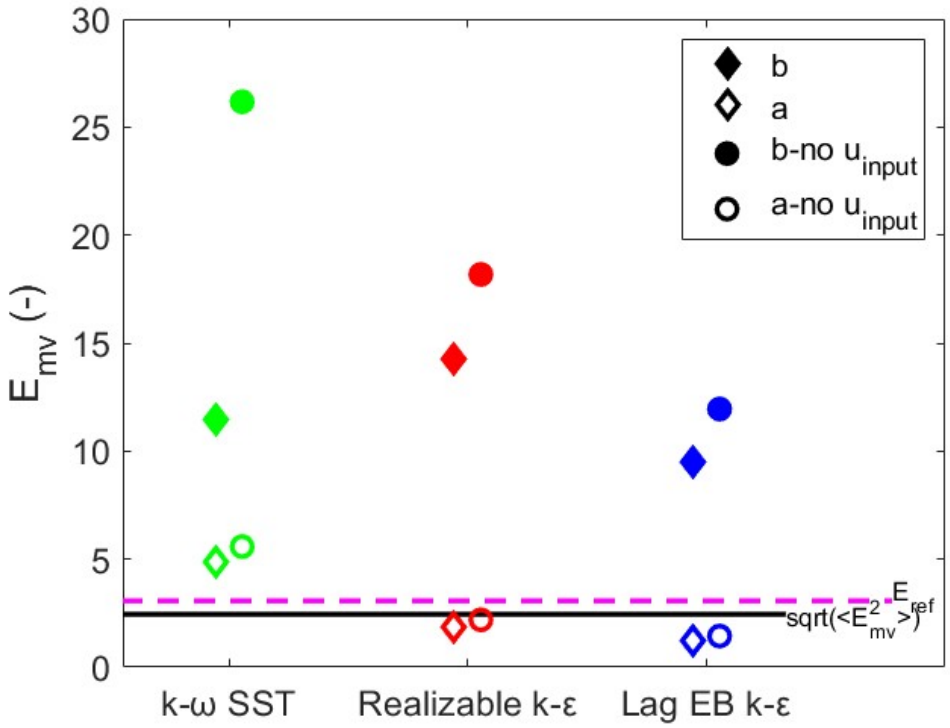

Fig. 5.8 Results of the multivariate analysis on the MC mock-up for the four cases consierad. Taken from [50].

5.1.6 Results and discussion

Looking at the results of the multivariate assessment of the three RANS models against the mock-up experimental outcome, in Figure 5.8, again a qualitative effect coming from the assumption on the common error source for the experimental data is clear. Observing the results for *Case a*, in which no identical error sources are considered, the E_{mv} evaluated for the two $\kappa - \varepsilon$ models is lower than the reference value E_{ref} represented with the dashed line, while for the $\kappa - \omega$ SST model it is above, ruling it out from the list of the recommended models for the investigated

case study. This agrees with the results reported in Figure 5.3 where at high flow rate the error bar of the simulation results with $\kappa-\omega$ SST does not lie in the error area of the experimental results. In *Case b*, i.e., accounting for the uncertainty correlation among the set points, for none of the selected models the discrepancy between simulated and experimental pressure drop can be justified only by the experimental data, input uncertainties as well as numerical uncertainties, and must be attributed to the adequacy / inadequacy of the model. However, Lag EB $\kappa-\varepsilon$ turbulence model has the best performance to simulate pressure drop with a lower E_{mv} value with respect to the Realizable $\kappa-\varepsilon$ models. Note that if the uncertainty due to simulation input parameters was neglected, taking also the first derivatives of Eq. 5.19 as null, the E_{mv} would have increased for all models with a much larger effect on the $\kappa-\omega$ SST model. However, the ranking of the three models remains the same even in that case.

5.2 Hydraulic verification of the improved MC design and uncertainty quantification on the pressure drop

Based on the design improvements reported in section 3.2.1, a cavity mock-up equipped with so called "short MCs" has been manufactured by Thales. Two test campaigns have been conducted on the mentioned mock-up: a thermal-hydraulic test at KIT, comparing the measured performances with other cavity mock-up, and a pure hydraulic test at PoliMI. The results of the measurements at KIT showed good performances of the mock-up if compared to straight MCs mock-up, but the test conditions and the available results are not good enough for model validation purpose. Test set-up improvements are currently under discussion. The present section only report the work done in the test campaign at PoliMI, where I personally took part in both the building of the hydraulic circuit and the measurements.

5.2.1 Test set-up and uncertainty quantification

As mentioned, an hydraulic circuit was built and implemented in an already existing test facility at PoliMI. In figure 5.9.a a picture of the test loop with the mock-up

is reported. The facility is equipped with two different ways to measure pressure drop: a differential pressure gauge, that can measure until 1 bar of pressure drop, and two relative pressure gauges, installed near the inlet and outlet of the mock-up. In the configuration in Figure 5.9.a the total pressure drop Δp_{tot} can be evaluated, as a measurement of the differential pressure gauge or as in Eq. 5.26. The test has been repeated for different values of mass flow rate.

$$\Delta p_{tot} = p_{in,tot} - p_{out,tot} \tag{5.26}$$

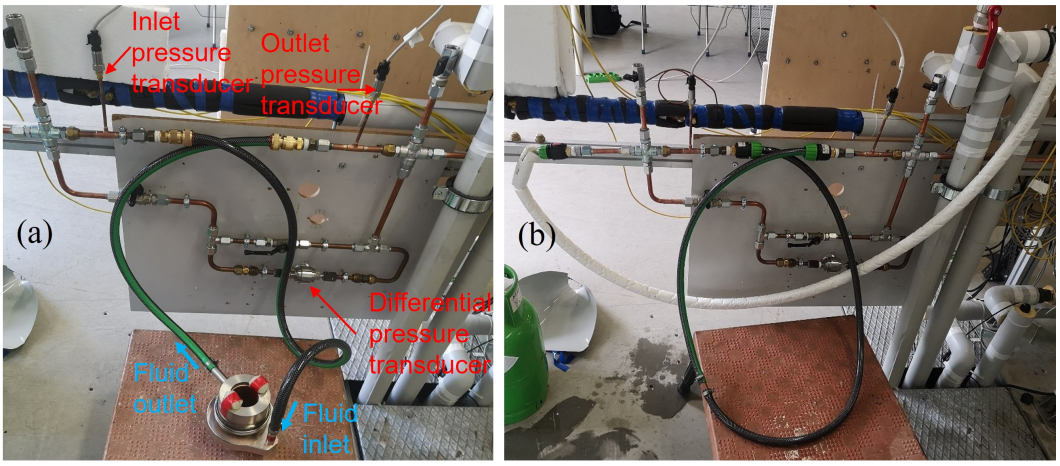

Fig. 5.9 a) Hydraulic loop and mock-up. b) Hydraulic loop for circuit calibration measurements

In order to evaluate the pressure drop characterizing only the mock-up, a loop calibration has been performed. The green pipes connecting the copper pipes of the loop to the mock-up have been connected with a short smooth pipe, as shown in Figure 5.9.b. The measurement have been repeated for similar values of the different mass flow rate considered in he previously described measurements. A new pressure drop, named Δp_{loop} is found, again a measurement of the differential pressure gauge and as in Eq. 5.27.

$$\Delta p_{loop} = p_{in,loop} - p_{out,loop} \tag{5.27}$$

The quantity of interest is the mock-up pressure drop ($\Delta p_{mock-up}$). It is needed, in fact to build the hydraulic characteristic of the short MCs design and to validate

the hydraulic part of the analysis model. It is obtained as the difference of the two previously mentioned pressure drops, as in Eq. 5.28.

$$\Delta p_{mock-up} = \Delta p_{tot} - \Delta p_{loop} \tag{5.28}$$

The pressure drops in Eq. 5.28 should be evaluated at the exact same mass flow rate. This was not possible, due to the manual change of the mass flow rate and its oscillations during the test. For this reason, the loop pressure drops measured, are used to evaluate a fitting curve. The obtained fitting curve is then used to evaluate the pressure drop at the exact averaged mass flow rates obtained in the Δp_{tot} measurements. The final data reduction equation adopted for the evaluation of the $\Delta p_{mock-up}$ is reported in Eq. 5.29

$$\Delta p_{mock-up} = \Delta p_{tot} - \Delta p_{loop,fit} = \Delta p_{tot} - a \times \dot{m}^2 \tag{5.29}$$

where $a = 1.694 \times 10^5$ (1/m^2). The results of the two values obtained with the available measurements instrument are represented in Figure 5.10

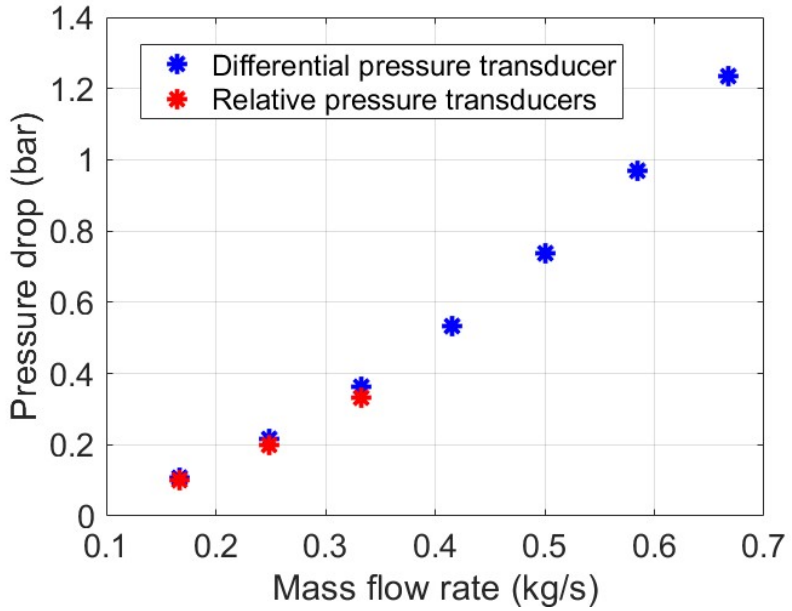

Fig. 5.10 Test results of the PoliMI test campaign

Concerning the uncertainties quantification (UQ) for the measurement results, the quadratic evaluation proposed by the "guide to the expression of Uncertainty in Measurement" (GUM) is adopted here [130]. Moreover, the classification of measurements uncertainties proposed by the GUM divides them in *TypeA* and *TypeB*. *TypeA* are the statistical uncertainties while *TypeB* are all the others, such as the accuracy of the instrumentation, that is considered in this study. Considering the uncertainty propagation law for the data reduction equation used for the evaluation of $\Delta p_{mock-up}$ in Eq. 5.29, the general form of the measurement uncertainty is reported in Eq. 5.30

$$u_D^2 = \sum_{i=1} \left(\frac{\partial \Delta p_{mock-up}}{\partial X_i} \right)^2 u_{X_i}^2 = \sum_{i=1} \left(\frac{\partial (p_{in} - p_{out} - a \times \dot{m}^2))}{\partial X_i} \right)^2 u_{X_i}^2 \tag{5.30}$$

where X_i is the generic i-th variable of the data reduction equation affected by uncertainty. Type A and B uncertainty equations are reported in Eq. 5.31 and Eq. 5.32.

$$\begin{aligned} u_{D,A}^2 &= \sum_{i=1} \left(\frac{\partial \Delta p_{mock-up}}{\partial X_i} \right)^2 u_{X_{i,A}}^2 = \\ &1 \times u_{p_{in,tot,A}}^2 + 1 \times u_{p_{out,tot,A}}^2 + (-2a\dot{m})^2 u_{\dot{m}_A}^2 + (-\dot{m})^2 u_{a_A}^2 \end{aligned} \tag{5.31}$$

$$\begin{aligned} u_{D,A}^2 &= \sum_{i=1} \left(\frac{\partial \Delta p_{mock-up}}{\partial X_i} \right)^2 u_{X_{i,B}}^2 = \\ &1 \times u_{p_{in,tot,B}}^2 + 1 \times u_{p_{out,tot,B}}^2 + (-2a\dot{m})^2 u_{\dot{m}_B}^2 + (-\dot{m})^2 u_{a_B}^2 \end{aligned} \tag{5.32}$$

The *typeA* uncertainties are evaluated as the standard deviation of the mean value. For example, for p_{in_A} the formula to evaluate the mean value is reported in Eq. 5.33 and the evaluation of the square of the uncertainty is given by Eq. 5.34. This evaluation is used for the uncertainties of p_{in} and p_{out}, while the uncertainties of $\dot{m}$ cannot be evaluated, because of missing statistical information, and a are considered negligible.

$$\overline{p}_{in} = \frac{1}{n}\sum_{k=1}^{n} p_{in,k} \tag{5.33}$$

$$u^2_{p_{in,A}} = stdv^2(\overline{p}_{in}) = \frac{1}{n(n-1)}\sum_{k=1}^{n}(p_{in,k} - \overline{p}_{in})^2 \tag{5.34}$$

The *TypeB* uncertainties are evaluated assuming a uniform distribution and that the upper and lower bounds are equal and of the same value of the instrument uncertainty given by the supplier ($b^+ = b^- = b$). Eq. 5.35 report the formula for the *typeB* uncertainty for the p_{in}.

$$u^2_{p_{in,B}} = \frac{b^2}{3} \tag{5.35}$$

the value of b for the pressure measurement is 0.075 bar while for the mass flow rate is 3% of the measured value.

5.2.2 Simulation set-up and uncertainty quantification

A 3D, steady-state pure hydraulic model is built in the commercial software STAR-CCM+ for the numerical estimations. Constant water properties at the test temperature and pressure are used in the simulations. The Lag EB κ-ε turbulence model is used, being the one with best performance in the work presented in Section 5.1. the computational domain with the BCs are shown in Figure 5.11. Making advantage of the symmetry of the geometry, only half of the fluid domain flowing in the mock-up is simulated. The inlet mass flow rate and the pressure outlet are imposed. figure 5.11 also gives the streamlines of the velocity field, showing an abrupt increase of the velocity at the entrance of the MCs (from $\sim$7 m/S to $\sim$12 m/s).

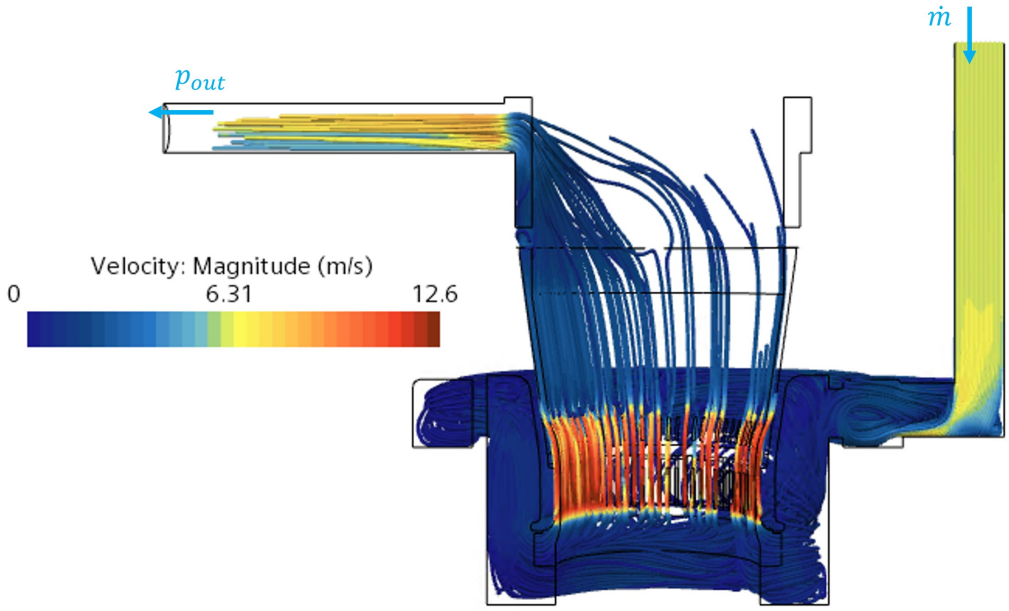

Fig. 5.11 Computational domain, BCs and velocity streamlines of the cavity mock-up equipped with new MC design, tested at PoliMI

The numerical uncertainty u_{num} is evaluated with a convergence study, refining only the area of the MCs and the area before and after the MCs (the orange area in Figure 5.12.a). The progressive refinement interested both the mash base size and the number of prism layers, keeping constant the thickness of the first prism layer and the total prism layers thickness. The method used for the evaluation of the observed order of convergence θ is the same of Subsection 5.1.4. The finest mesh is represented on an axial section f the computational domain in Figure 5.12.b. A zoom on the MC is given in Figure 5.12.c.

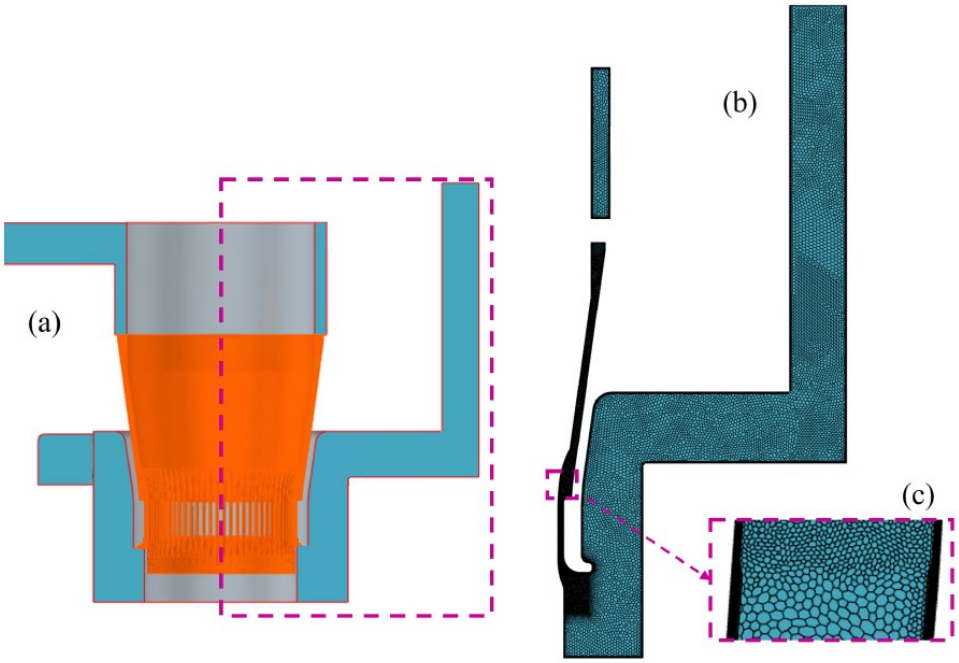

Fig. 5.12 a) computational domain with highlighted refinement area in orange, b) finest mesh used on an axial section of the computational domain, c) zoom on the MC refinement.

Fig. 5.12 a) computational domain with highlighted refinement area in orange, b) finest mesh used on an axial section of the computational domain, c) zoom on the MC refinement.

The possible influence on simulation uncertainty due to uncertainties in the input values (u_{input}) is also analyzed. The input values that may be affected by uncertainty are the geometry, the mass flow rate and fluid properties. The sensitivity of the simulation results to variation in the input properties is considered negligible and for its computational cost and the lack of information on the manufacturing tolerance on the MCs realization, the geometry uncertainty is not considered in this analysis. The local method is used also here for the evaluation of the u_{input} due to uncertainty in the mass flow rate. The values considered for the uncertainty in each simulation corresponds to the uncertainty of the flow meter.

5.2.3 Results

The results obtained from simulations and measurements, with their uncertainties, are reported in Figure 5.13.a. All the numerical results fall in the uncertainty bars of

the experimental results. Because of the dependence of the mass flow rate uncertainty on the measured values (being a percentage of it), the experiments uncertainty bars are bigger at higher mass flow rate. A zoom on the highest mass flow rate considered is given in Figure 5.13.b. A comparison of different RANS turbulence models is offered in the zoom for the highest mass flow rate considered (given by the limit of the hydraulic circuit characteristic and the pump). For all the models considered, the simulation results fall in the experimental uncertainty bar. This does not allow to state if one model is working better than the others for this case study. One reason could be the relatively low range of mass flow rate (∼10-40 l/min) considered with respect to the study presented in Section 5.1, where discrepancy was found between the κ-ω SST model and the measurement results for the highest mass flow rate considered (80 l/min).

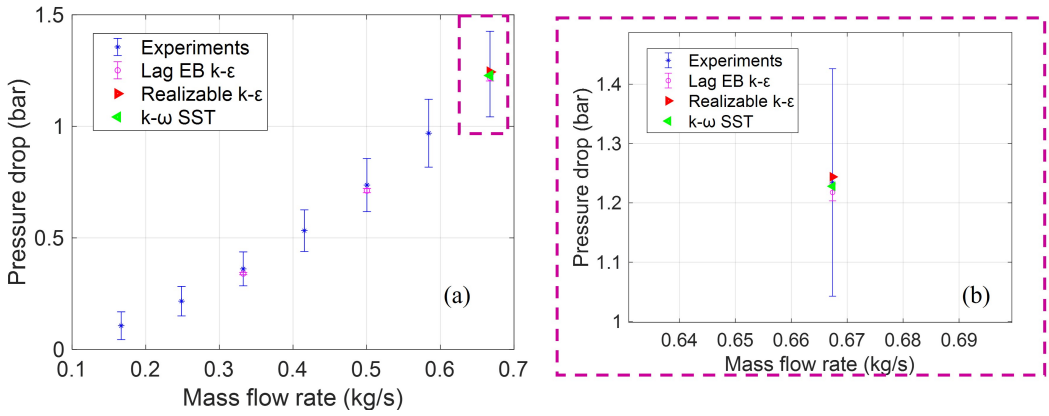

Fig. 5.13 a) Experimental and numerical hydraulic characteristic of the mock-up equipped with new MCs design, b) zoom on the highest measured mass flow rate, with turbulence models comparison.

5.3 Thermal-hydraulic model validation on straight MC mock-up

A first attempt of thermal-hydraulic model validation on a circular cavity mock-up is reported in this section. A cavity mock-up equipped with mini-channels has been realized and tested at KIT (see Figure 5.14) with the aim of studying the performance of the designed cooling system with cooling tests. The mock-up is equipped with 16 thermocouples (TC) all around the cavity and one temperature sensor at each one of

the two inlets and outlets. In the test campaign, the heat load on the cavity inner wall has been obtained thanks to the ohmic losses due to the eddy currents induced in the cavity by an inductive heater. At first, the mock-up has been tested without water flow with five different inductor powers (600, 1200, 1800, 2400 and 3000 W) for ten (first three cases) and five minutes (last two cases). The ohmic losses released by the inductive heater have been numerically evaluated with electro-magnetic (EM) simulations by KIT and used in a pure thermal model, developed by PoliTo, using the commercial software STAR-CCM+. Computed and experimentally evaluated temperatures with the different thermocouples have been compared, underlining the need for a heat load calibration since the evaluation of the real current of the inductive heater, used as input in the EM model, is affected by some uncertainties. The first part of this section is dedicated to the calibration of the input power.

Calorimetry tests have been conducted with different inductor powers and water flow rate, confirming the results obtained in the calibration study. The experimental results have been compared with computed results obtained with thermal-hydraulic (TH) simulations, using the commercial software STAR-CCM+, in which the calibrated heat load has been used as thermal driver, with the aim of validating the model.

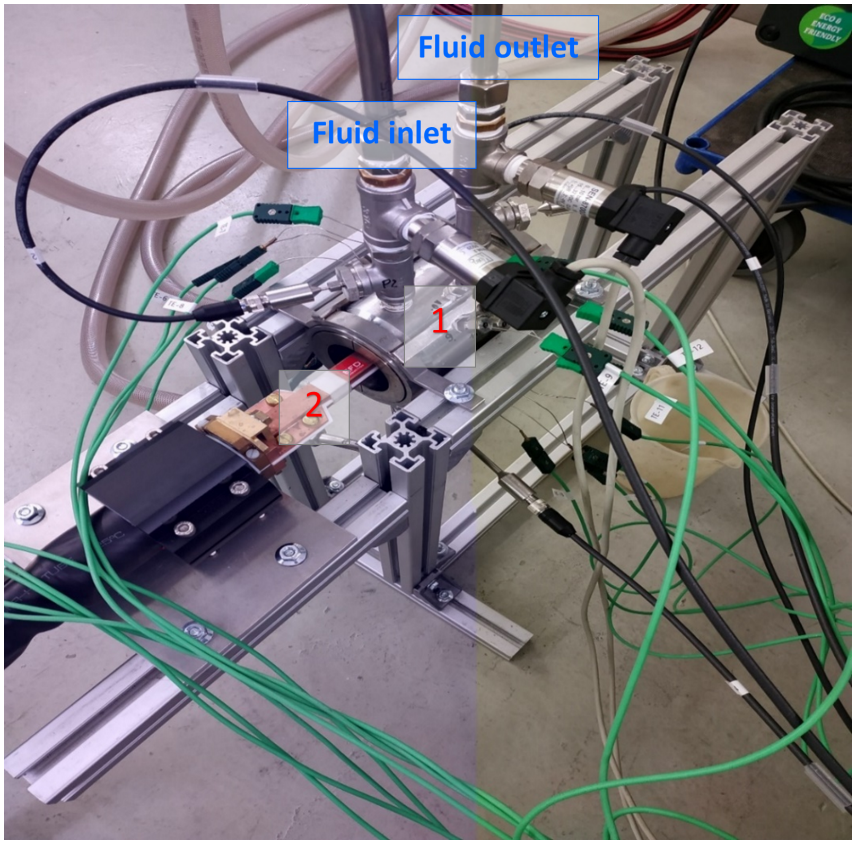

Fig. 5.14 A picture of the test facility at KIT: the mock-up of a MCs cooled cavity installed on the test stand, indicated with 1, and the inductive heater, indicated with 2. Taken from [51].

5.3.1 Thermal model for the inductive power calibration

In the test of the mock-up with the inductive heater, a crucial point is the precise evaluation of the power deposited by the heater in the sample. That evaluation has been performed using an Electro-Magnetic (EM) model developed at KIT and detailed in [51]. The integral values of the heat flux are summarized in Table 5.7. However, the uncertainties hidden in the EM model requires a calibration of the heating power, for which dedicated test campaign of the mock-up without active cooling has been performed [51]. A pure thermal transient 3D model for the cavity mock-up has been developed using the commercial software STAR-CCM+, based on the geometry shown in Figure 5.15, where the sample is assumed to be "floating" (no thermal bridges to the supports), and the holes drilled to insert the TCs have been ignored.

Table 5.7 Computed deposited heat load on the inner wall.

Nominal inductor power (W)	Computed deposited Q on the inner wall (W)
600	33
1200	131
1800	295
2400	524
3000	819

A polyhedral mesh has been used with a base size of 1.4 mm, refining the zone of the cavity and water-stopper near the high heat load region, where the TCs are located, respectively with a base size of 0.4 mm and 0.8 mm (see Figure 3). Temperature-dependent material properties have been used in the simulations for both the stainless-steel (SS) and the Glidcop. Thermal contact resistances have been conservatively imposed on the solid interfaces, equal to $1 * 10^4$ m^2 K/W for the Glidcop/Glidcop interface and $5 * 10^4$ m^2 K/W for the SS/SS interface, but the impact of these parameters has been checked afterward to be negligible on the calibration factor result, so that imposing no thermal resistance would return the same results. An implicit unsteady model with time step equal to 0.1 s and 15 inner iterations has been proved to give robust results, on a mesh with $\sim 1.6 \times 10^6$ cells, providing grid-independent results.

The heat load to the cavity wall computed with the EM model for different inductor power levels (in the range 600 W - 1800 W) has been applied to the inner wall of the cavity (red surface in Figure 5.15) while all the other walls have been considered adiabatic. The initial temperature (T_0) for the entire mock-up has been set equal to the measured ambient temperature (T_{amb}) of 24.3°C. All the simulations have been run up to 600 s.

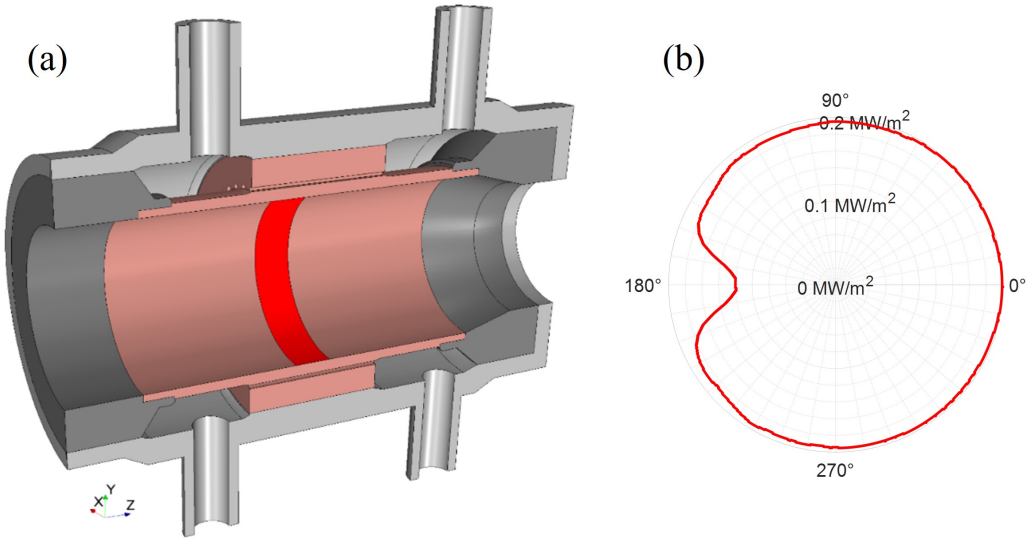

Fig. 5.15 (a) CAD geometry used for the mock-up thermal model. The grey solids refer to stainless-steel and the pink parts to Glidcop. (b) In the insert in red: azimuthal distribution of the heat flux on the cavity surface, as from the EM simulations with 1800 W of inductor power. Taken from [51].

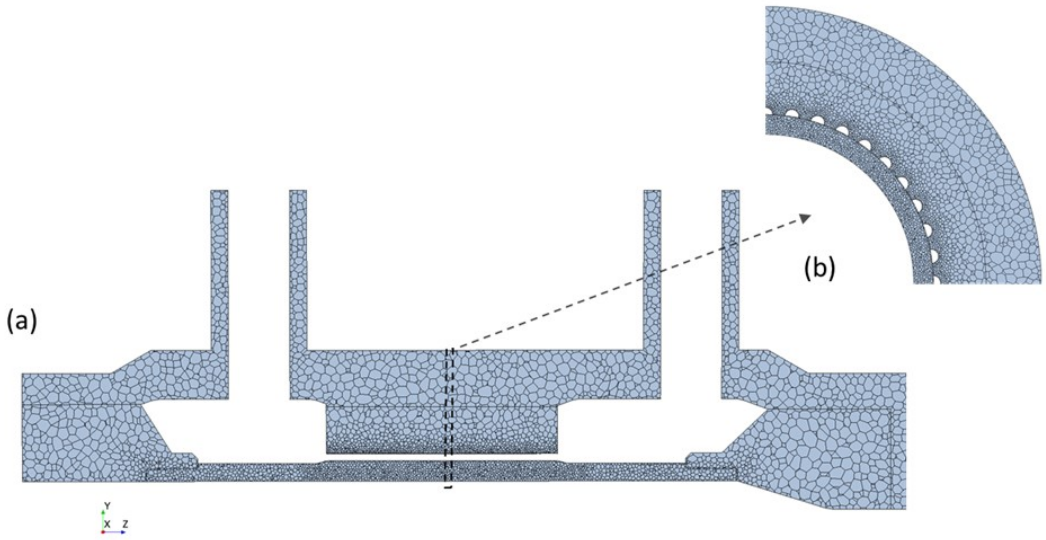

Fig. 5.16 (a) Polyhedral mesh on a longitudinal section of the upper half of the solid parts of the pure thermal model, and (b) zoomed in view on the transversal middle section. Taken from [51].

In the evaluation of the computed results, the temperature at the TCs has been computed as a surface average of a 1 mm diameter sphere positioned at the nominal

location of the TCs, assuming a perfect contact between the TC head and the Glidcop surface. The comparison between the computed and experimental evolution of the temperature increase at the TC locations shows, independently on the power level, a large underestimation in the simulations, see Figure 5.17.

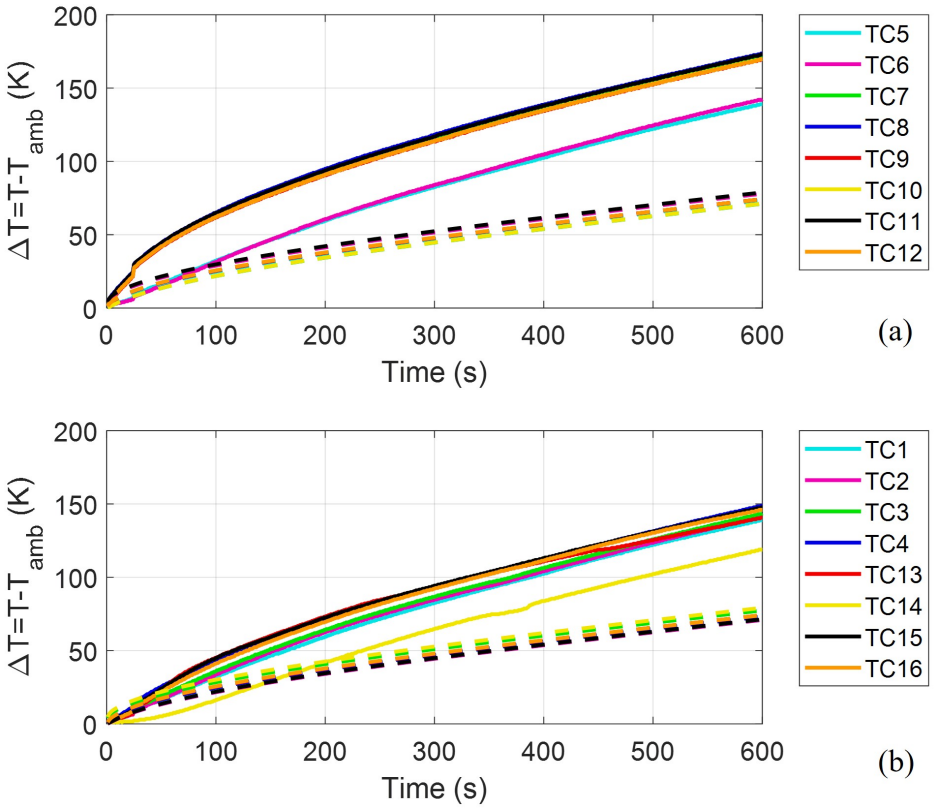

Fig. 5.17 Measured temperature evolution at the 16 thermocouples (solid lines) and corresponding computed values (dashed lines), at the Inductor power level of 1800 W at (a) the upper and (b) the lower part of the mock-up, using in input the HL as resulting from the EM model. Taken from [51].

A calibration procedure has been carried out in order to evaluate the correction factor to be applied to the EM results from the ratio between the experimental and computed traces. For this study, experimental and computed results for 600, 1200 and 1800 W of inductive nominal power have been considered. For each TC trace we first evaluate $r_i(t)$, which is the instantaneous ratio between the experimental (T_D) and the computed temperature T_S increases for the i-th TC, as in Eq. 5.36 (see

Figure 5.18). Note that the temperature increases are all evaluated with respect to the ambient temperature.

$$r_i(t) = \frac{dT_D(t)}{dT_S(t)} \tag{5.36}$$

The values of $r_i(t)$ are then averaged for the whole set of 16 TCs, returning $r_{gl}(t)$ as from Eq. 5.37.

$$r_{gl}(t) = \frac{\sum_{i=1}^{16} r_i(t)}{16} \tag{5.37}$$

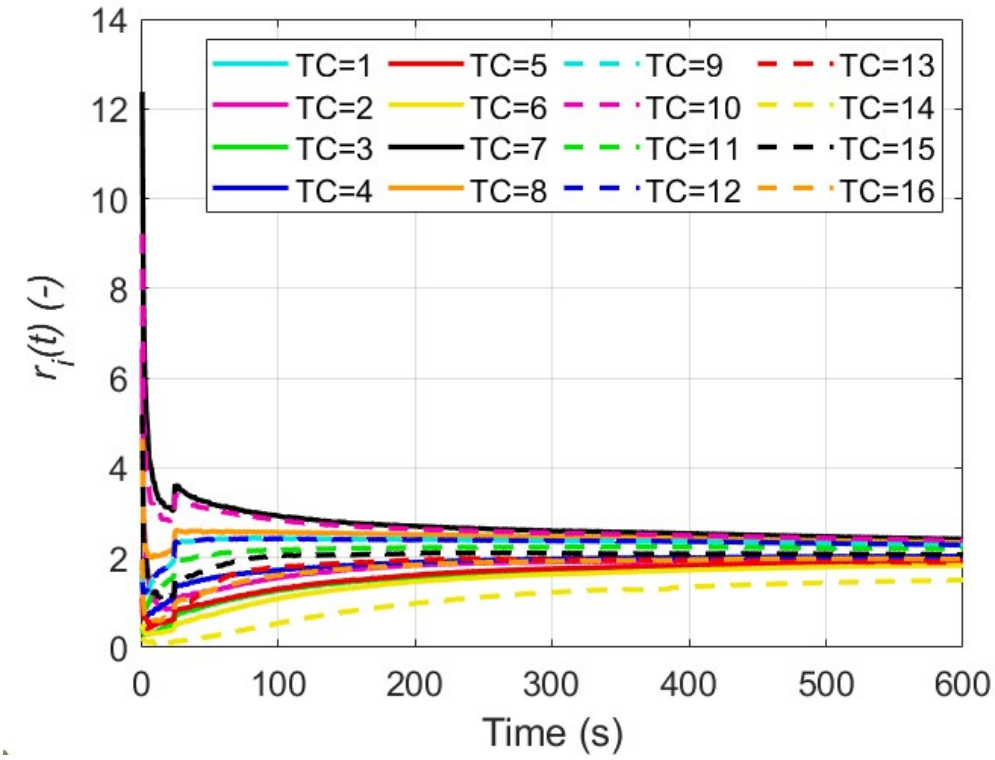

Fig. 5.18 $r_i(t)$ evaluated for each thermocouple at the inductor power level of 1800 W. Taken from [51].

The correction factor cal_Q has been computed at each heat load averaging $r_{gl}(t)$ on the time, starting from the time t_{start} as shown in Eq. 5.38.

$$cal_Q = \frac{\sum_{t_{start}}^{600s} r_{gl}(t_j)}{600 - t_{start}} \tag{5.38}$$

In Eq. 5.38, t_{start} has been diametrically increased to find values of cal_{HL} independent on its arbitrary choice, see Figure 5.19. Averaging the asymptotic values of cal_{HL} computed for the different power levels, a final calibration factor cal of ~ 2 is obtained, which is reported in Eq. 5.39 with its estimated accuracy.

$$cal = 2.04 \pm 0.04 \tag{5.39}$$

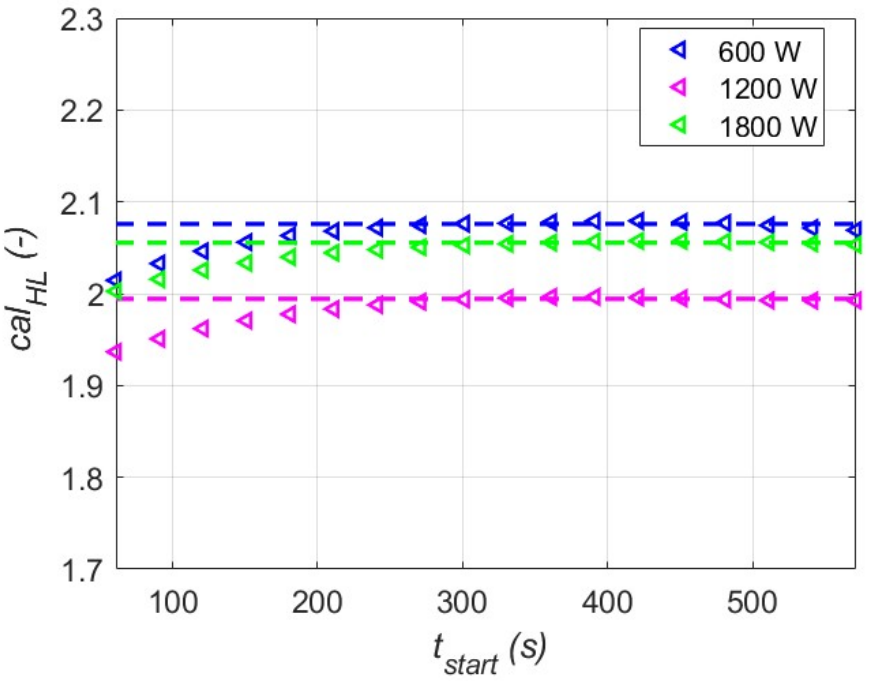

Fig. 5.19 Calibration factor computed as a function of the arbitrary choice of t_{start} (symbols) for the different Q values. The asymptotic values (dashed lines) used to evaluate the mean calibration factor cal are also reported.

5.3.2 Calorimetry results

The measurements from the preliminary experimental campaign, devoted to the calorimetric assessment of the heat load on the cavity have been carefully analysed to check the calibrated value of the heat load for the simulations. The calibration

tests were performed at different flow rates, varying the inductor power and, also, swapping the flow direction. A check of the robustness of the recipe adopted for the assessment of the heat load by the inductive heater is first carried out at a global level, cross-checking the calibrated heat load used in the simulations with the heat load computed from the experimental calorimetry, see Figure 5.20, following Eq. 5.40.

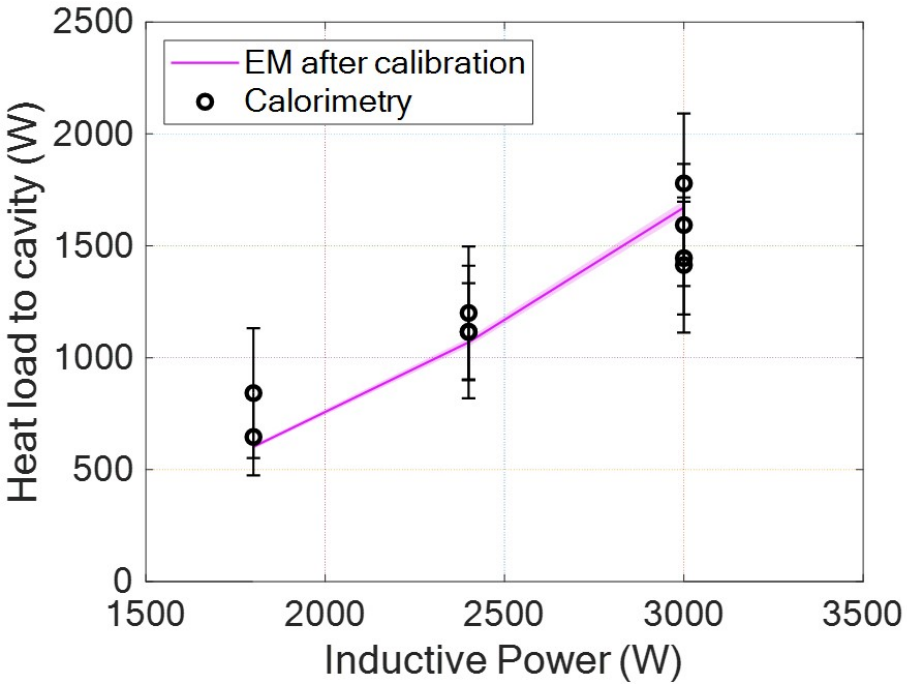

Fig. 5.20 Calorimetry check: heat load values from the EM model, after the calibration correction (solid line), compared to the measured values from calorimetry (open circles), with the respective uncertainty range. For the computed values, the uncertainty range is represented as a small red shaded area around the solid red line.

$$Q^D = \dot{m}^D \times c_p \times (T^D_{out} - T^D_{in}) \tag{5.40}$$

where Q^D is the heat load calculated from the experimental results, $\dot{m}^D$ is the total water mass flow rate measured in the cavity, c_p is the water specific heat, T^D_{out} and T^D_{in} are the outlet and inlet temperatures of the water, averaged on the two inlets and two outlets of the mock-up. The calorimetry check is reported in Figure 5.20, showing that the calibrated values of the total heat load on the cavity inner wall fall within the uncertainty range of the experimental points at all the power levels.

5.3.3 Thermal-hydraulic model

A 3D steady-state conjugate thermal-hydraulic model has been then developed, again using the commercial software STAR-CCM+ .Since the mock-up is cooled by subcooled water entering the cooling region by two different inlets in parallel, the model for the thermal-hydraulic simulations also includes T-junctions upstream and downstream of the mock-up (Figure 5.21) to allow the balance of the flow computed in the two branches.

The well-established $\kappa - \omega$ *SST* turbulence model [127], with all y^+ wall treatment, is adopted in the simulations since it is able to capture the flow detachment downstream of the mini-channels region. Calorimetry tests have been performed at 10 l/s and 20 l/min of total flow rate. In the first case, the flow in the mini-channels is in transition flow regime, therefore a gamma-transition model has been adopted. The mesh built in the fluid domain account for 12 millions cells, with a core-flow base size of 0.15 mm The thickness of the first wall prism layer has been defined in order to obtain a dimensionless wall distance $y^+ \sim 1$.

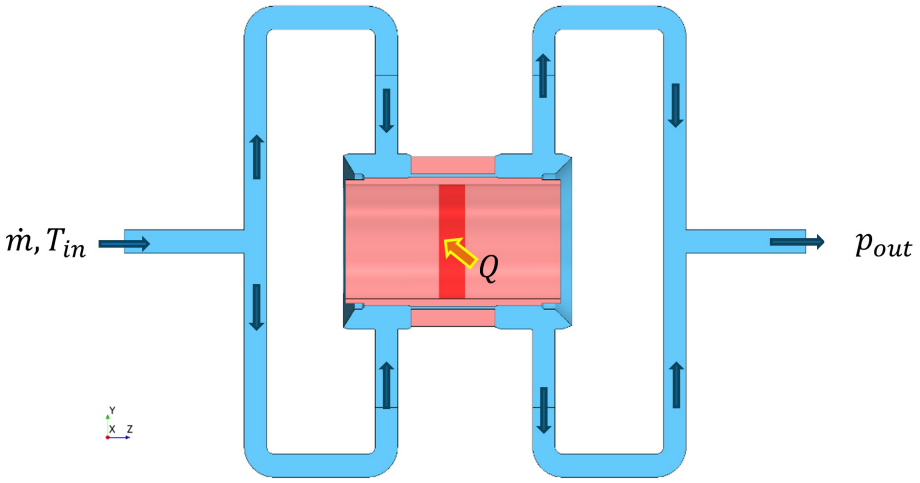

Fig. 5.21 Sketch of the reference geometry for the full 3D thermal-hydraulic simulations, including also the water domain (in light blue). Half of the computational domain is shown.

5.3.4 Validation of the thermal-hydraulic model

After a re-calibration of the thermocouples, performed as described in [131], several tests with water flow have been reconducted with reversed flow direction (from left

to right in Figure 2). Temperatures measured with the different 16 TCs are compared with those one computed in the TH simulations in Figure 5.22, Figure 5.23 for the inductor power of 2400 W and two different values of the mass flow rates, and in Figure 5.24 and Figure 5.25 for the inductor power of 2400 W and two different values of the mass flow rate. Note that also in the simulations the flow direction has been reversed.

In all the four cases, a general good agreement between measured and computed temperatures is observed. Notice that the TCs located in the middle section measure in all cases higher temperature differences than the ones located in upstream and downstream position, since they are nearer to the heat load pick (red surface with the label 2 in Figure 5.14). Moreover, the TCs marked with the label 'A' (11, 6 in the top row and 3, 14 in the bottom row) are located close to the inner wall of the cavity and measure the highest temperature increase in each case both in the experiment and in the simulations.

Everywhere, except for the downstream sensors, the computed values overestimate the measured ones: that is expected, since the TCs are not simulated as a separated material, with a finite contact resistance to the sample, as it is in the reality, so that an overestimation of the measured temperature is expected from the model.

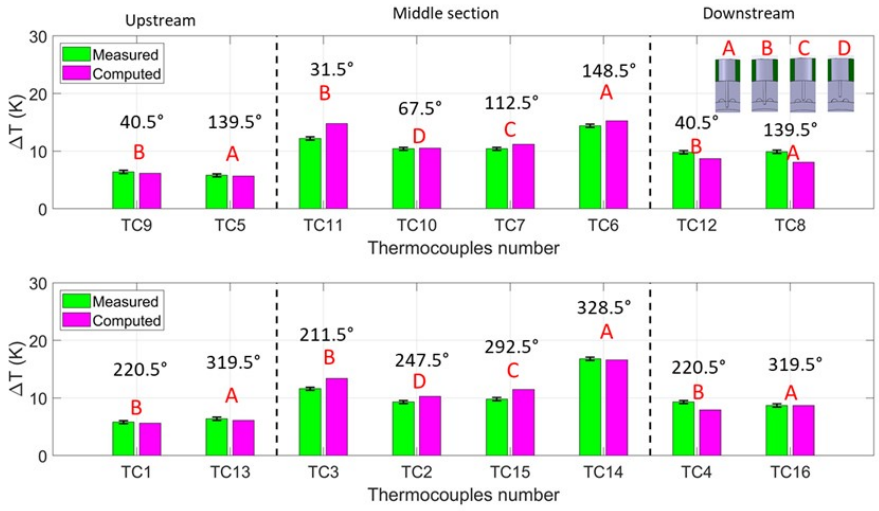

Fig. 5.22 Temperatures evaluated at the different positions of the 16 TCs for the inductor power of 2400 W and the water flow rate of 10 l/min. The different depths of the TC position are indicated in the insert on the right upper corner. For the angular position (written on top of the bar) see Figure 1(b).

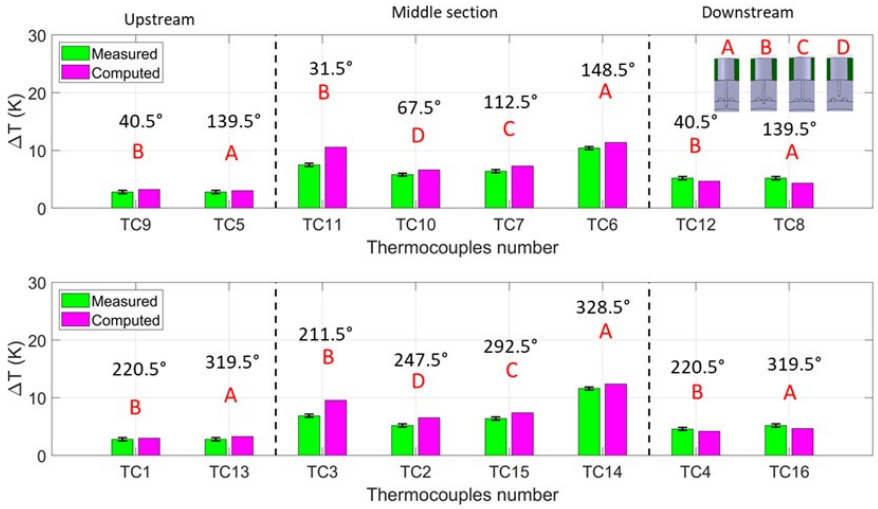

Fig. 5.23 Temperatures evaluated at the different positions of the 16 TCs for the inductor power of 2400 W and the water flow rate of 20 l/min. The different depths of the TC position are indicated in the insert on the right upper corner. For the angular position (written on top of the bar) see Figure 1(b).

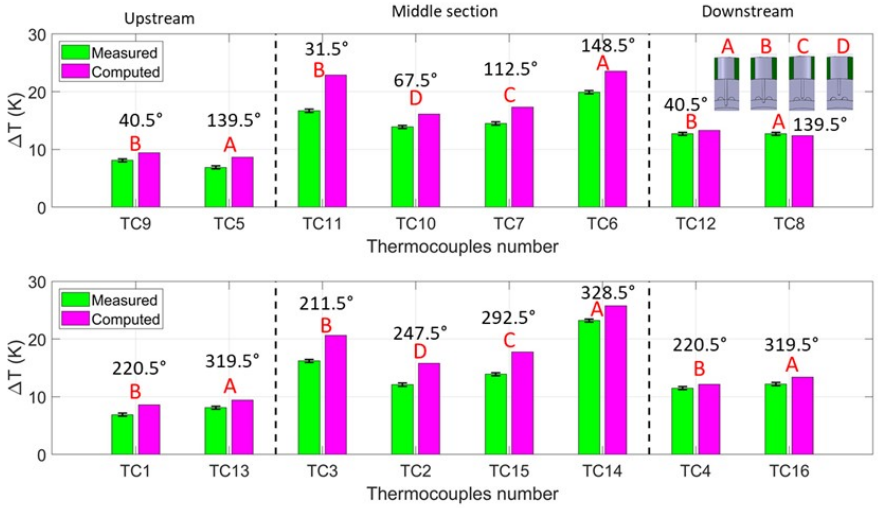

Fig. 5.24 Temperatures evaluated at the different positions of the 16 TCs for the inductor power of 3000 W and the water flow rate of 10 l/min. The different depths of the TC position are indicated in the insert on the right upper corner. For the angular position (written on top of the bar) see Figure 1(b).

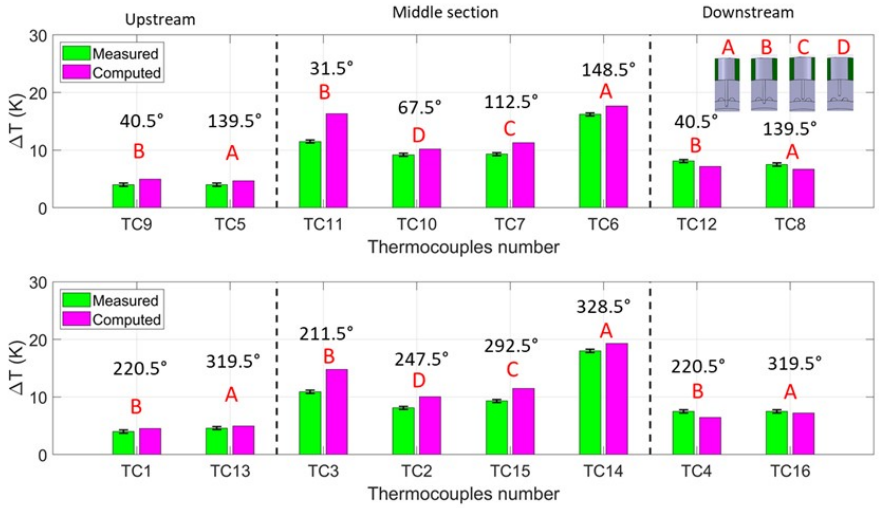

Fig. 5.25 Temperatures evaluated at the different positions of the 16 TCs for the inductor power of 3000 W and the water flow rate of 20 l/min. The different depths of the TC position are indicated in the insert on the right upper corner. For the angular position (written on top of the bar) see Figure 1(b).

In order to explore the effect of the modelling of the TCs, a parametric analysis on the thermal contact resistance R_{th} between the TCs and the solid parts (both simulated with the thermo-physical properties of Glidcop) of the mock-up has been carried out on a reduced domain extrapolated from the full-size mock-up. The R_{th} has been changed from 0 to 2×10^{-3} m^2 K/W, mimicking each of the four thermocouples (A, B, C and D) in the heated section. The maximum value of the R_{th} has been chosen taking into account air thermal conductivity (λ_{th}) equal to 0.026 W/m/K for the air layer between the thermocouple and the mock-up, which is 0.05 mm all around the TC. For the sake of simplicity, the same contact resistance has been considered for the TC head. When, instead, the value of R_{th} is considered null, the reduced domain is replicating the conditions of the full-size mock-up simulation. A slice of 27 ° C, with three mini-channels, of only solid parts (see Figure 5.26) has been simulated in steady state conditions, imposing at the interfaces between solid and water (light blue surfaces in Figure 5.26) the heat transfer coefficient (HTC) obtained in the previous CFD simulations for an inductor power of 3000 W and 10 l/min of water flow rate. Homogeneous Neuman condition has been imposed on the symmetry planes (dark blue surfaces in Figure 5.26) and the previous calibrated heat load has been imposed on the heated surface (red surface in Figure 5.26), again

in the case of the inductor power of 3000 W. All the other surfaces are considered adiabatic.

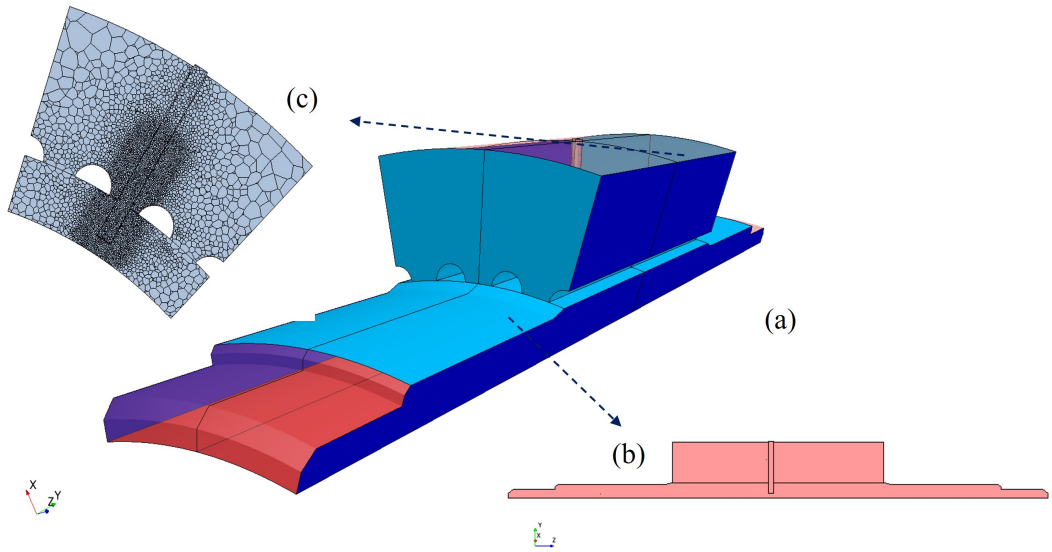

Fig. 5.26 (a) Overview and (b) longitudinal cross section of the reduced domain used to study the effect of a more detailed modeling of the TC. (c) Mesh detail on the transversal cross section of the reduced domain. The picture is taken for the case with TC type A.

Observing the results reported in Table 5.8, considering a finite value for the R_{th} between the TC and the mock-up, the computed temperature differences are ∼3-4 K lower than in the case with no thermal resistance for the TCs which are located in the resonator (type A and B, respectively), where the highest temperature gradient is experienced. The computed difference between the two cases decreases moving away from the heated wall, for the TCs of type C and D, located in the water stopper. This discrepancy in the computed temperature increase is due to the distortion of the temperature map of the cavity (see Figure 5.27), obtained considering or not the actual presence of the TCs in the model, which perturbs the heat transfer. In relative terms, the temperature increase computed neglecting any perturbation effect on the thermal field due to hole and insertion of the TC could lead to an overestimation of the temperature increase by $\sim$ 19% at the location of TC A, $\sim$ 16% at the location of TC B, $\sim$ 9% for TCs C and $\sim$ 5% for TCs D.

Table 5.8 Reduced model results: computed temperature increase (with respect to the reference value of 23 °C) for the different TCs types, varying the R_{th}.

R_{th} (m^2K/W)	ΔT_A (° C)	ΔT_B (° C)	ΔT_C (° C)	ΔT_D (° C)
2×10^{-3}	20.15	18.29	15.5	14.69
0	24.05	21.29	16.98	15.51

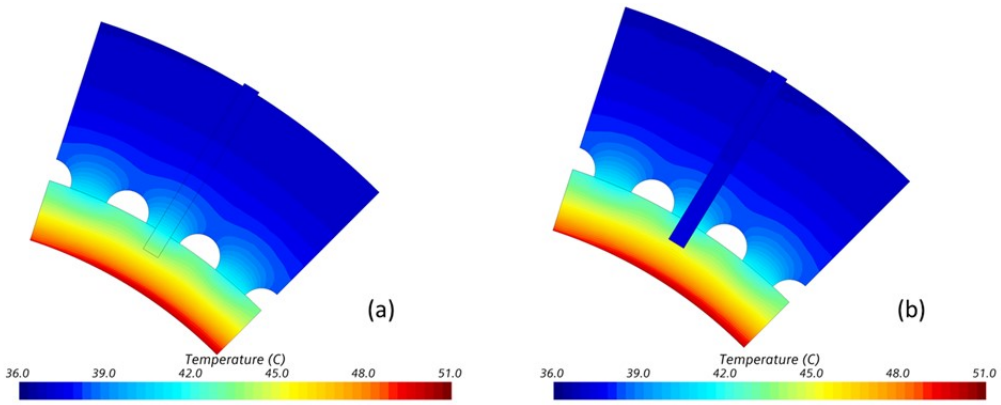

Fig. 5.27 Temperature distribution for TC of type B with R_{th}=0 (m^2 K)/W (a) and R_{th}=2.0*10^{-3} (m^2 K)/W (b).

The above mention caveats on the possible overestimations introduced in the simulated TC read-outs do not apply to the downstream sensor, where the simulated values underestimate the measured ones. The only plausible justification for the computed values, which are lower than the measured ones, is that the heat load deposition occurs on a slightly longer area, or is slightly displaced downstream, with respect to what is actually considered in the simulations. Note that the fact that higher errors are always observed for the TCs in the middle section, comparing TCs at same depth, goes in the same direction of some inaccuracy in the heat flux distribution computed along the cavity. The spatial distribution used in the simulations could not be anyhow validated by the calibration check, since, in fact, that gives only an indication of the integral value of the heat flux, without any hint on its distribution. If the calorimetry analysis showed an agreement between the measured and calibrated integral values of the heat loads, further studies are necessary to confirm the distribution along the axial coordinate.

In Figure 5.28, Figure 5.29, Figure 5.30 and Figure 5.31 the global relative errors, evaluated with respect to the measured temperature differences are reported for each

case. The relative errors on the different tests on all the TCs show that the largest discrepancy is computed on the TC of type B, especially in the heated zone – the TC of type A and B, in fact, have been demonstrated to be the most sensitive to the approximations in the TC modelling, see above. Overall, even considering these errors, in all simulations the average error on temperature increase remains below 20%.

According to the analysis of the computed and experimental results, both tests and simulations have proven the efficiency of the mini-channels cooling for the mock-up. During pure thermal tests without water flow, in fact, temperatures differences higher than 420 K have been measured for 1800 W of inductor power, while during tests with active cooling steady state conditions have been reached, registering maximum values of temperature below 303 K for 3000 W of inductor power and 10 l/min of water flow. A wide possibility of increasing the water flow rate is left to cool down the cavity in higher heat flux conditions.

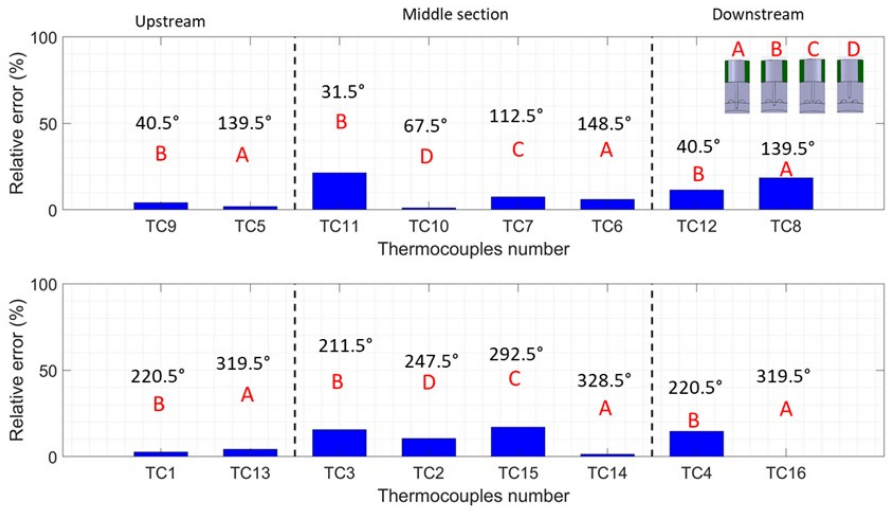

Fig. 5.28 Local relative error for 2400 W of inductor power with the water flow rate of 10 l/min. The different depths of the TC position are indicated in the insert on the right upper corner.

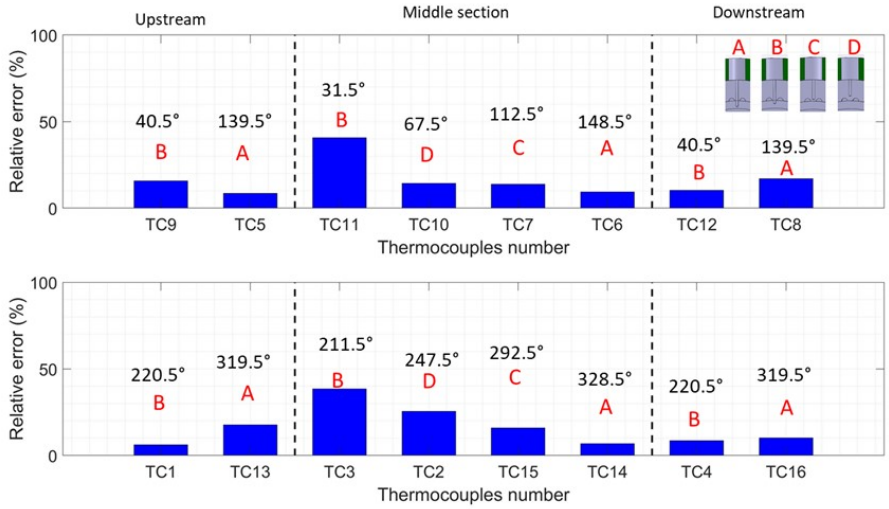

Fig. 5.29 Local relative error for 2400 W of inductor power with the water flow rate of 20 l/min. The different depths of the TC position are indicated in the insert on the right upper corner.

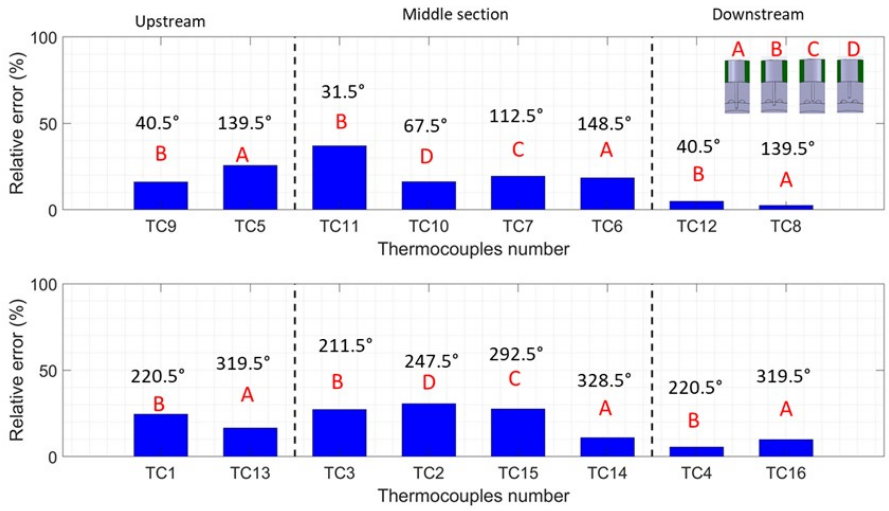

Fig. 5.30 Local relative error for 3000 W of inductor power with the water flow rate of 10 l/min. The different depths of the TC position are indicated in the insert on the right upper corner.

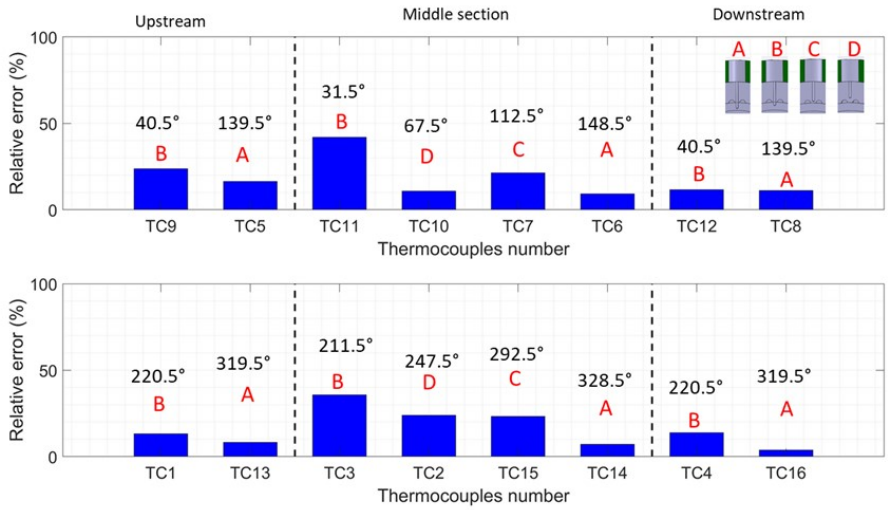

Fig. 5.31 Local relative error for 3000 W of inductor power with the water flow rate of 20 l/min. The different depths of the TC position are indicated in the insert on the right upper corner.

Chapter 6

Conclusions and future perspectives

The importance of an efficient cooling system for the resonator is due to the interconnections among the several physics interesting the problem. The resonant frequency of the RF wave produced by the vacuum tube strictly depends, in fact, on the cavity geometry and in particular on the dimension of the inner wall. A direct link can be found between the cavity expansion and the wave frequency down-shift, and consequent tube efficiency reduction. Similarly the cavity expansion is due to the high temperature peaks on the cavity inner wall, caused by the peaked heat flux released during the normal operations of the gyrotron. Moreover, the flux shape, with a strong peak in the cavity and low values in the down and up taper regions, leads to a similarly peaked axial temperature profile. This is the reason of high thermal stresses computed in numerical analysis. Moreover, as in all cooling configuration design, pressure drop plays also an important role, which in this case should be below 6 bar, from system requirements. Therefore, a cooling solution that, not only minimizes the frequency shift, by minimizing the radial displacements on the inner wall, but also reduces the thermal stresses below the yield strength of the cavity material, while keeping the pressure drop below the system restriction, is required.

The study carried out and presented in this thesis faces the problem of the cavity cooling through three branches: numerical, experimental and theoretical. The numerical methods are used for analysis of designs (already existing and new ones) and for the optimization processes to arrive to new designs. The experimental activity serves for model validation purposes, but also for a confirmation of the

design performances. The theoretical analysis is developed to verify the stability of an optimized cooling configuration.

Several optimization strategies have been explored, analyzing different physics of the problem. Making use of the BBO algorithm, an optimization work was performed directly on the thermo-mechanical problem. The optimization algorithm was, in fact, coupled to a finite element model, where the cooling was modeled as a convective boundary conditions. In this way the direct minimization of displacements, while controlling the stresses, was allowed. The aim of this work was indeed to find an optimized HTC profile, the values of which are the design variable of the optimization problem, and then a cooling solution reproducing that HTC profile was designed, exploiting the longitudinal direction of the flow. The use of an evolutionary algorithm coupled with a CFD model would have required more computational time, thus the choice of a thermo-mechanical model was preferred. Anyhow this didn't allow an optimization performed directly on the cooling system geometry to meet the cost function and constraint, hence a second step to produce a cooling configuration and check its performances with CtFD is needed. The comparison of the thermo-mechanical model and thermal-hydraulic model results validated the procedure, that can be used for future analysis and design of cooling systems of different cavities. Moreover, the obtained HTC profile can be a guide for more complex cooling strategies, giving information on where a more efficient cooling is needed in the axial direction. An example could be longitudinal the mini-channels configuration with smaller channel diameter where higher HTC is required.

Adjoint-based topology optimization was instead used on the thermal-hydraulic problem or on a pure hydraulic problem, by defining specific cost functions that could face the problem at hand. This method directly modifies the geometry, or topology (giving the name to the method), of the design, at the cost of a high computational effort. As some exotic solutions may be found, further smoothing and modification of the optimized solution are possibly needed, toward its manufacturability. In this case, it was not possible to define the optimization problem by the direct control of displacements and stresses. In one case, the thermal-hydraulic one, where the energy equation is solved and solid components are modeled in the optimization, the need of minimizing displacements was transformed in an average temperature minimization on the heated surface. The control on thermal constraint, which is linked to temperature gradients, was translated in the minimization of the standard deviation of the temperature on the heated surface. If from one hand, the use of

this method and the optimization carried out on the thermal-hydraulic model does not allow to control directly the mechanical aspects, a control on the pressure drop is still possible, treated as a constraint in this case. Moreover, there is no need of further steps of geometry design as in the previous case with BBO. Unfortunately, this optimization work didn't provide us with a competitive solution in terms of maximum temperature, and hence displacements, if compared to existing solutions and with the optimized one obtained with BBO. Further parametric studies could be conducted on the pressure drop constraint or the cost function wight, to obtain a better solution. Anyhow, as a first conclusion, the method is not robust enough at the moment and needs further improvements. If adjoint-based topology optimization method are demonstrated to produce interesting results in 2D, simple optimization problems, further studies are necessary for their application in 3D, complex problems.

Similarly to the thermal-hydraulic one, the optimization work on the pure-hydraulic model, reported in section 4.1, defines the optimization problem set-up based on the knowledge that an homogeneous temperature axial profile, will reduce thermal stresses. Hence it is needed to improve the heat removal in the HL peak area. To do so, the link between mass flow rate, which means velocity, which in turn means HTC, is exploited. In this case, the cost function is defined as a weighted function including the mass flow rate axial distribution in the azimuthal micro-channels and the pressure drop. An homogeneous mass flow rate distribution was the target in the case of micro-channels distributed with higher density in the heat flux peak area. In case of equally spaced micro-channels, a mass flow rate distribution was in turn the target, following the heat flux profile, with the use of the Dittus-Boelter correlation. Also in this case, there is no direct control on displacements and stresses, but the pressure drop is included in the optimization problem and the optimized geometry is already given by the optimizer, with no need of further steps. In this study, the strategy aiming at a homogeneous mass flow rate distribution gave better results both in terms of cost function values (compared with the definition of specific KPI) and manufacturability of the obtained topology/geometry. The equally spaced channels, in fact, presented a final topology which turned out very difficult to manufacture. Also here, the use of the topology method seems to suggests the difficulty in finding proper solutions for complex problems, involving heat transfer, especially for the equally spaced channels where a peaked mass flow rate distribution was targeted. In the equally loaded channels, instead, a more acceptable solution in terms of manufacturability was found.

Because of the complexity and the multi-physics nature of the problem at hand, the different optimization processes carried out faced the problem mainly from one or two physics, exploiting the links between them. In particular, as the frequency shift is strictly connected to the wall displacement, the multiphysics problem could be simplified by focusing on the displacements minimization, hence no optimization based directly on the minimization of the frequency shift, acting on the ED field, is considered here. The decision of directly including only some of the physics involved in the complex problem of the cavity cooling in the optimization process allows to drastically reduce the computational cost of the optimization work. On the other hand, it does not allow to control all the aspects of the problem. In the coupling of thermo-mechanical problem with BBO, for example, neither the pressure drop nor the geometry can be controlled directly. In order to account for all the physics characterizing this problem, future works can be done aimed at developing surrogate models for some of the physics, such as the electromagnetic part and its link to the thermo-mechanical behavior of the component. This could allow to include more or even all the physics in the optimization algorithm chosen, adding some cost to the computation and time, but not as high as including all the models of all the physics.

On the other hand, predictive modeling of the cavity behavior is useful, not only for design purpose, but also for the analysis of gyrotron operating conditions. We may need to analyze different operating points of the same gyrotron (such as different resonant frequency), or different gyrotrons performances, having similar cavity cooling configurations. Thus, models validation is crucial for both analysis and design. An experimental campaign at Thales was devoted to validation of the hydraulic model on longitudinal mini-channels cooling system, building and testing a cavity mock-up. A multivariate analysis is carried out exploiting the measurement results, allowed to compare different RANS turbulence models with the outcome that, among the considered ones, the Lag EB $\kappa-\varepsilon$ is the best one in terms of pressure drop prediction. Future sensitivity analysis could be necessary to compare RANS model with LES models. Moreover, a test facility built at KIT is being used for thermal-hydraulic tests on several cavity mock-ups. The aim of this tests is to compare experimentally different cooling strategies, material and manufacturing processes, but also to validate the thermal-hydraulic model used for analysis and design of gyrotron cavities. A validation study was performed in 2020-2021. After a calibration study on the heat load released on the cavity inner wall during the experiments, some discrepancies were still present between the TC measurements and the simulations,

that couldn't be explained by the available uncertainties information. More work is undergoing on this path, in particular some improvement on the test set-up are planned in order to increase the heat load released, which needs to be comparable to the one in real gyrotron cavities, and improve the measurement instruments to reduce their uncertainties.

References

[1] US Energy Information Administrative. International energy outlook 2023, October 2023. [Online; posted 11-October-2023].

[2] R. Lindsay and L. Dahlman. Climate change: Global temperature, January 2024. [Online; posted 18-January-2024].

[3] Environemental Defence Fund. 9 ways we know human caused climate change, May 2024. [Online; posted 09-May-2024].

[4] ITERorganization.

[5] T.J. Dolan. *Magnetic Fusion Technology*. Los Alamos Science, 2013.

[6] R.Buttery R. Pitts and S. Pinches. Fusion: The way ahead. *Phys. World*, 19:20.

[7] Plasma Science and fusion Center MIT.

[8] N.G. Sabri. Production of high power by using gyrotron device for electron cyclotron resonance heating in tokamak reactor. *Energy Procedia*, 18:944–953, 2012. Terragreen 2012: Clean Energy Solutions for Sustainable Environment (CESSE).

[9] A.R. Choudhury. *Investigations of After Cavity Interaction in Gyrotrons Including the Effect of Non-Uniform Magnetic Field*. Phd thesis, KIT, Karlsruhe, Germany, 2014.

[10] M.V. Kartikeyan, E. Borie, and M. Thumm. *Gyrotrons: high-power microwave and millimeter wave technology*. Springer Science & Business Media, 2013.

[11] S. Gold and G. Nusinovich. Review of high-power microwave source research. *Review of Scientific Instruments*, 68:3945–3974, 11 1997.

[12] AJ.R. Gilmore. Modeling and optimization of a low power 60ghz gyrotron collective Thomson scattering system. Master's thesis, MIT, USA, 1994.

[13] J. Ragini and M. Kartikeyan. Design of a 60 GHz, 100 kW CW gyrotron for plasma diagnostics: GDS-V.01 simulations. *Progress in Electromagnetics Research B*, 22:379–399, 01 2010.

[14] I. Ogawa, M. Iwata, T. Idehara, K. Kawahata, H. Iguchi, and A. Ejiri. Plasma scattering measurement using a submillimeter wave gyrotron (gyrotron FU-II) as a power source. *Fusion Engineering and Design*, 34-35:455–458, 1997. Fusion Plasma Diagnostics.

[15] G. Link, L. Feher, M. Thumm, H.J. Ritzhaupt-Kleissl, R. Bohme, and A. Weisenburger. Sintering of advanced ceramics using a 30-GHz, 10-kW, CW industrial gyrotron. *IEEE Transactions on Plasma Science*, 27(2):547–554, 1999.

[16] S. Miyake. Millimeter-wave materials processing in Japan by high-power gyrotron. *IEEE Transactions on Plasma Science*, 31(5):1010–1015, 2003.

[17] J.M. Osepchuk. A history of microwave heating applications. *IEEE Transactions on Microwave theory and Techniques*, 32(9):1200–1224, 1984.

[18] S. Mitsudo, H. Hoshizuki, T. Idehara, and T. Saito. Development of material processing system by using a 300 GHz CW gyrotron. *Journal of Physics: Conference Series*, 51(1):549, nov 2006.

[19] M. Thumm. Recent applications of millimeter and submillimeter wave gyrotrons. In *Proceedings of the 25th International Conference on Infrared and Millimeter Waves*, pages 99–102, Beijing, China, 2000. IEEE.

[20] Y. Makino et al. Fabrication of bulk ceramics by high-power millimeter-wave radiation. *Japanese Journal of Applied Physics*, 40(2S):1080, 2001.

[21] I. Toshitaka, S. Svilen Petrov, G. Mikhail, and M. Seitaro. The gyrotrons as promising radiation sources for THz sensing and imaging. *Applied Sciences*, 10(3), 2020.

[22] S. LeVine. The active denial system. a revolutionary, non-lethal weapon for today's battlefield. Technical report, Center for Technology and National Security Policy (National Defence University, Washington DC), National Defence University, Washington DC, 2009.

[23] W.M. Manheimer. On the possibility of high power gyrotrons for super range resolution radar and atmospheric sensing. *International journal of electronics*, 72(5-6):1165–1189, 1992.

[24] R.M. L'Hermitte. Cloud and precipitation remote sensing at 94 ghz. *IEEE transactions on geoscience and remote sensing*, 26(3):207–216, 1988.

[25] A.Y. Wong, J. Steinhauer, R. Close, and T. Fukuchi G.M. Milikh. Conservation of ozone in the upper atmosphere by selective ion removal. *Comments on Plasma Physics and Controlled Fusion*, 12(5):223–234, 1989.

[26] M. Garven, J.P. Calame, K. Nguyen, B. Danly, B. Levush, and F.N. Wood. Experimental studies of a four-cavity, 35 GHz gyroklystron amplifier. *Plasma Science, IEEE Transactions on*, 28:672 – 680, 07 2000.

[27] M. Lucente, V. Dainelli, C. Dionisio, and M. Noce. An innovative multimode millimeter wave radar for moon remote sensing. In *Proceedings of IEEE Aerospace conference*, pages 1–8, Big Sky, MT, USA, 2009.

[28] N. Kumar, U. Singh, T.P. Singh, and A.K. Sinha. A review on the applications of high power, high frequency microwave source: Gyrotron. *Journal of fusion energy*, 30:257–276, 2011.

[29] A.G. Litvak, G.G. Denisov, and M.Y Glyavin. Russian gyrotrons: Achievements and trends. *IEEE Journal of Microwaves*, 1(1):260–268, 2021.

[30] R. Ikeda et al. Progress on performance tests of ITER gyrotrons and design of dual-frequency gyrotrons for ITER staged operation plan. *Nuclear Fusion*, 61(10):106031, sep 2021.

[31] A. Leggieri et al. Progress of european industrial gyrotron developments for nuclear fusion. In *2023 24th International Vacuum Electronics Conference (IVEC)*, pages 1–2, 2023.

[32] F.H. Braunmüller et al. Results on the 1 MW CW 170 GHz gyrotron TH1509UA at the FALCON test stand. Presented at the 22nd workshop on ECE/ECRH, Danjeon, Republic of Korea, 2024.

[33] M.K.A. Thumm, G.G. Denisov, K. Sakamoto, and M.Q. Tran. High-power gyrotrons for electron cyclotron heating and current drive. *Nuclear Fusion*, 59(7):073001, jun 2019.

[34] J.C. Maxwell. *A treatise on electricity and magnetism*. Oxford university press, 1873.

[35] K. Avramidis et al. Numerical studies on the influence of cavity thermal expansion on the performance of a high-power gyrotron. In *Proceedings of the IVEC 2017 on 18th International Vacuum Electronics Conference*, pages 1–2, 04 2017.

[36] EUROFusion, The demonstration power plant.

[37] A. Bertinetti, K.A. Avramidis, F. Albajar, F. Cau, F. Cismondi, Y. Rozier, L. Savoldi, and R. Zanino. Multi-physics analysis of a 1 MW gyrotron cavity cooled by mini-channels. *Fusion Engineering and Design*, 123:313–316, 2017. Proceedings of the 29th Symposium on Fusion Technology (SOFT-29) Prague, Czech Republic, September 5-9, 2016.

[38] K.A. Avramidis, I. Pagonakis, C. Iatrou, and J. Vomvoridis. EURIDICE: A code-package for gyrotron interaction simulations and cavity design. volume 32, 09 2012.

[39] A. Sella. Raschig Rings. *Chemistry World*, 2008.

[40] L. Savoldi et al. Assessment and optimization of the cavity thermal performance for the European continuous wave gyrotrons. In *Proceedings of the 27th IAEA Fusion Energy Conference*, 2018.

[41] R. Marchesin et al. Manufacturing and test of the 1 MW long-pulse 84/126 GHz dual-frequency gyrotron for TCV. In *Proceedings of the 2019 International Vacuum Electronics Conference (IVEC)e*, 2019.

[42] L. Savoldi, K.A. Avramidis, F. Albajar, S. Alberti, A. Leggieri, and F. Sanchez. A validation roadmap of multi-physics simulators of the resonator of MW-class CW gyrotrons for fusion applications. *Energies*, 14(23), 2021.

[43] L. Savoldi et al. CFD analysis of different cooling options for a gyrotron cavity. *IEEE Transactions on Plasma Science*, 44(12):3432–3438, 2016.

[44] L. Savoldi et al. CFD analysis of mini-channel cooling for a gyrotron cavity. In *Proceedings of the 26th Symposium on Fusion Techology*, Austin, TX, USA, 05 2015.

[45] S. Karmakar et al. Electrical and thermal design of a *w* -band gyrotron interaction cavity. *IEEE Transactions on Plasma Science*, 47(7):3155–3159, 2019.

[46] A. Kumar et al. Thermal and structural analysis and its effect on beam-wave interaction for 170-GHz, 1-MW gyrotron cavity. *Journal of Fusion Energy*, 31:164–169, 2012.

[47] A. Bertinetti et al. Design, test and analysis of a gyrotron cavity mock-up cooled using mini channels. *IEEE Transactions on Plasma Science*, 46(6):2207–2215, 2018.

[48] P. Kalaria et al. Design studies of mini-channel cavity cooling for a 170 GHz, 2 MW coaxial-cavity gyrotron. In *Proceedings of the 2019 International Vacuum Electronics Conference (IVEC)*, pages 1–2, 04 2019.

[49] A. Allio, R. Difonzo, A. Leggieri, F. Legrand, R. Marchesin, and L. Savoldi. Test and modeling of the hydraulic performance of high-efficiency cooling configurations for gyrotron resonance cavities. *Energies*, 13(5), 2020.

[50] R. Difonzo, E. Gajetti, L. Savoldi, and N. Fathi. Assessment of different RANS turbulence models in mini-channels for the cooling of MW-class gyrotron resonators. *International Journal of Heat and Mass Transfer*, 193:122922, 2022.

[51] S. Stanculovic et al. Calibration of the KIT test setup for the cooling tests of a gyrotron cavity full-size mock-up equipped with mini-channels. *Fusion Engineering and Design*, 172:112744, 2021.

[52] D. Thevien and G. Janiga. *Optimization and Computationl Fluid Dynamics*. 2008.

[53] G. Allaire, F. Jouve, and A.M. Toader. Structural optimization using sensitivity analysis and a level-set method. *Journal of Computational Physics*, 194(1):363–393, 2004.

[54] E. Papoutsis-Kiachagias and K. Giannakoglou. Continuous adjoint methods for turbulent flows, applied to shape and topology optimization: Industrial applications. *Archives of Computational Methods in Engineering*, 23, 12 2014.

[55] E. Kontoleontos et al. Adjoint-based constrained topology optimization for viscous flows, including heat transfer. *Engineering Optimization*, 45, 08 2013.

[56] J. Alexandersen and C.S. Andreasen. A review of topology optimisation for fluid-based problems. *Fluids*, 5(1), 2020.

[57] H. Brinkman. A calculation of the viscous force exerted by a flowing fluid on a dense swarm of particles. *Flow Turbulence and Combustion*, 1:27–34, 1949.

[58] O. Sigmund and K. Maute. Topology optimization approaches: A comparative review. *Structural and Multidisciplinary Optimization*, 48, 12 2013.

[59] S.C. Morris. *Life's Solution: Inevitable Humans in a Lonely Universe*. Cambridge University Press, 2005.

[60] W.M. Zage. The geometry of binocular visual space. *Mathematics Magazine*, 53(5):289–294, 1980.

[61] J.D. Bagley. *The behavior of adaptive systems which employ genetic and correlation algorithms*. Phd thesis, University of Michigan, Ann Arbor, Michigan, USA, 1967.

[62] J. Holland. *Adaptation in natural and artificial systems*. 1975.

[63] M. M. Be Vellasco R.S. Zebulum, M. A. Pacheco. *Evolutionary Electronics. Automatic Design of Electronic Circuits and Systems by Genetic Algorithms*. 2017.

[64] A. Norouzi and H.A. Zaim. Genetic algorithm application in optimization of wireless sensor networks. *The Scientific World Journal*, 2014(1):286575, 2014.

[65] A. Tsenov. Simulated annealing and genetic algorithm in telecommunications network planning. *INTERNATIONAL JOURNAL OF COMPUTATIONAL INTELLIGENCE*, 3:240–245, 01 2005.

[66] N. Singh and P. K. Chaurasia. A review on genetic algorithm operations and application in telecommunication routing. *International Journal of Computer Sciences and Engineering*, 7:273–277, 07 2019.

[67] A. Ghaheri, S. Shoar, M. Naderan, and S.S. Hoseini. The applications of genetic algorithms in medicine. *Oman Medical Journal*, 30(6):406–416, 12 2015.

[68] P. Srivastava and T.H. Kim. Application of genetic algorithm in software testing. *International Journal of Software Engineering and Its Applications*, 3, 11 2009.

[69] H. Lingaraj. Parallel indexing on color and texture feature extraction using r-tree for content based image retrieval. *International Journal of Computer Sciences and Engineering*, 3:11–15, 11 2015.

[70] I. Abuiziah and N. Shakarneh. A review of genetic algorithm optimization: Operations and applications to water pipeline systems. *International Journal of Mathematical and Computational Sciences*, 7(12):1782 – 1788, 2013.

[71] A. Aly and R. Peralta. Comparison of a genetic algorithm and mathematical programming to the design of groundwater cleanup systems. *Water Resources Research - WATER RESOUR RES*, 35:2415–2426, 08 1999.

[72] T. Bhoskar, O.K. Kulkarni, N.K. Kulkarni, S.L. Patekar, G.M. Kakandikar, and V.M. Nandedkar. Genetic algorithm and its applications to mechanical engineering: A review. *Materials Today: Proceedings*, 2(4):2624–2630, 2015. 4th International Conference on Materials Processing and Characterzation.

[73] Resat Selbaş, Önder Kızılkan, and Marcus Reppich. A new design approach for shell-and-tube heat exchangers using genetic algorithms from economic point of view. *Chemical Engineering and Processing: Process Intensification*, 45(4):268–275, 2006.

[74] P. Wildi-Tremblay and L. Gosselin. Minimizing shell-and-tube heat exchanger cost with genetic algorithms and considering maintenance. *International Journal of Energy Research*, 31:867 – 885, 07 2007.

[75] H. Peng and X. Ling. Optimal design approach for the plat–fin heat exchangers using neural networks cooperated with genetic algorithms. *Applied Thermal Engineering - APPL THERM ENG*, 28:642–650, 04 2008.

[76] P. Wildi-Tremblay and L. Gosselin. Layered porous media architecture for maximal cooling. *International Journal of Heat and Mass Transfer - INT J HEAT MASS TRANSFER*, 50:464–478, 02 2007.

[77] K. Foli and T. Okabe et al. Optimization of micro heat exchanger: CFD, analytical approach and multi-objective evolutionary algorithms. *International Journal of Heat and Mass Transfer*, 49:1090–1099, 03 2006.

[78] R. Hilbert, G. Janiga, R. Baron, and D. Thévenin. Multi-objective shape optimization of a heat exchanger using parallel genetic algorithms. *International Journal of Heat and Mass Transfer*, 49(15):2567–2577, 2006.

[79] L. Gosselin, M. Tye-Gingras, and F. Mathieu-Potvin. Review of utilization of genetic algorithms in heat transfer problems. *International Journal of Heat and Mass Transfer - INT J HEAT MASS TRANSFER*, 52:2169–2188, 04 2009.

[80] Martin Philip Bendsøe and Noboru Kikuchi. Generating optimal topologies in structural design using a homogenization method. *Computer Methods in Applied Mechanics and Engineering*, 71(2):197–224, 1988.

[81] T. Borrvall and J. Petersson. Topology optimization of fluid in stokes flow. *International Journal for Numerical Methods in Fluids*, 41:77 – 107, 01 2003.

[82] A. Gersborg, O. Sigmund, and R. Haber. Topology optimization of channel flow problems. *Structural and Multidisciplinary Optimization*, 30:181–192, 01 2005.

[83] L. Olesen, F. Okkels, and H. Bruus. A high-level programming-language implementation of topology optimization applied to steady-state navier–stokes flow. *International Journal for Numerical Methods in Engineering*, 65:975 – 1001, 02 2006.

[84] A. Evgrafov. The limits of porous materials in the topology optimization of stokes flows. *Applied Mathematics and Optimization*, 52:263–277, 10 2005.

[85] G. Pingen, A. Evgrafov, and K. Maute. Topology optimization of flow domains using the lattice boltzmann method. *Structural and Multidisciplinary Optimization*, 34:507–524, 12 2007.

[86] G. Pingen, A. Evgrafov, and K. Maute. A parallel schur complement solver for the solution of the adjoint steady-state lattice boltzmann equations: Application to design optimisation. *International Journal of Computational Fluid Dynamics*, 22:457–464, 08 2008.

[87] D. Alonso, L. Sá, J. Romero, and E. Silva. Topology optimization based on a two-dimensional swirl flow model of Tesla-type pump devices. *Computers & Mathematics with Applications*, 77, 05 2019.

[88] D. Lim, M. Song, H. Chae, and E. Kim. Topology optimization on vortex-type passive fluidic diode for advanced nuclear reactors. *Nuclear Engineering and Technology*, 51, 03 2019.

[89] A. Sato, T. Yamada, K. Izui, S. Nishiwaki, and S. Takata. A topology optimization method in rarefied gas flow problems using the Boltzmann equation. *Journal of Computational Physics*, 395, 06 2019.

[90] G. Yoon. Topology optimization for turbulent flow with Spalart–Allmaras model. *Computer Methods in Applied Mechanics and Engineering*, 303, 02 2016.

[91] G. Yoon. Topology optimization method with finite elements based on the κ- ε turbulence model. *Computer Methods in Applied Mechanics and Engineering*, 361:112784, 04 2020.

[92] E.M. Dede. Multiphysics topology optimization of heat transfer and fluid flow systems. In *COMSOL Conference 2009*, 2009.

[93] G. Yoon. Topological design of heat dissipating structure with forced convective heat transfer. *Journal of Mechanical Science and Technology*, 24:1225–1233, 06 2010.

[94] A. A. Koga and E. Lopes et al. Development of heat sink device by using topology optimization. *International Journal of Heat and Mass Transfer*, 64(Complete):759–772, 2013.

[95] C. Dilgen, S. Dilgen, D. Fuhrman, O. Sigmund, and B. Lazarov. Topology optimization of turbulent flows. *Computer Methods in Applied Mechanics and Engineering*, 331, 12 2017.

[96] H. Li, X. Ding, F. Meng, D. Jing, and M. Xiong. Optimal design and thermal modelling for liquid-cooled heat sink based on multi-objective topology optimization: An experimental and numerical study. *International Journal of Heat and Mass Transfer*, 144:118638, 12 2019.

[97] D. Hu, Z. Zhang, and Q. Li. Numerical study on flow and heat transfer characteristics of microchannel designed using topological optimizations method. *Science China Technological Sciences*, 63, 11 2019.

[98] R. Difonzo, A. Allio, A. Cammi, and L. Savoldi. Biogeography-based optimization of the resonator cooling in a MW-class gyrotron for fusion applications. *IEEE Transactions on Plasma Science*, 50(11):4074–4079, 2022.

[99] R. Difonzo, A. Cammi, C. Introini, and L. Savoldi. Stability assessment of an optimized cooling configuration of a fusion gyrotron resonant cavity through an analytical model. *Fusion Engineering and Design*, 103(3), 2024.

[100] D. Simon. Biogeography-Based Optimization. *IEEE Transactions on Evolutionary Computation*, 12(6):702–713, 2008.

[101] M. Haiping, F. Minrui, D. Zhiguo, and J. Jing. Biogeography-based optimization with ensemble of migration models for global numerical optimization. In *2012 IEEE Congress on Evolutionary Computation*, pages 1–8, 2012.

[102] M. Mussetta and P. Pirinoli. MmCn-BBO schemes for electromagnetic problem optimization. In *2013 7th European Conference on Antennas and Propagation (EuCAP)*, pages 1058–1059, 2013.

[103] H. Ma, D. Simon, P. Siarry, Z. Yang, and M. Fei. Biogeography-based optimization: A 10-year review. *IEEE Transactions on Emerging Topics in Computational Intelligence*, 1(5):391–407, 2017.

[104] A. Hadidi and A. Nazari. Design and economic optimization of shell-and-tube heat exchangers using biogeography-based (BBO) algorithm. *Applied Thermal Engineering*, 51(1):1263–1272, 2013.

[105] N.S. Nise. *Control Systems Engineering*. Wiley, 2014.

[106] J. Duarte and M. Corradini. Hydraulic and heated equivalent diameters used in heat transfer correlations. *Nuclear Technology*, 201:1–4, 10 2017.

[107] A. Bertinetti. *Development of the Multi-physiCs tool for the integrated simulation of the Cavity and its application for the design of gyrotron cavities for thermonuclear applications*. Phd thesis, Politecnico di Torino, Torino, Italy, 2019.

[108] R. Difonzo. Design and optimization of the cooling strategy for a gyrotron cavity equipped with minichannels. Master's thesis, Politecnico di Torino, 2019.

[109] R. Difonzo, A. Cammi, H. Laqua, and L. Savoldi. Comparative analysis of different strategies exploiting the adjoint topology optimization method for enhancing the performance of a cooling device equipped with micro-channels. In *Proceedings of the 16th International Conference on Heat Transfer, Fluid Mechanics and Thermodynamics*.

[110] R. Difonzo, A. Cammi, N. Galanos, K.C. Giannakoglou, E.M. Papoutsis Kiachagias, and L. Savoldi. Design of the cooling system of the cavity of the european gyrotron using adjoint-based topology optimization exploiting the azimuthal flow direction. In *Proceedings of the 14th International Conference on Computational Heat and Mass Transfer*.

[111] M. H. Jafar, M. A. Thamer, S. M. Wahid, and H. A. Wissam. Modeling the uniformity of manifold with various configurations. *Journal of Fluids*, 2014, 2014.

[112] O.K. Siddiqui, M. Al-Zahrani, A. Al-Sarkhi, and S.M. Zubair. Flow distribution in u- and z-type manifolds: Experimental and numerical investigation. *Arabian Journal for Science and Engineering*, 45, 2020.

[113] M. Mohammadi, G.N. Jovanovic, and K.V. Sharp. Numerical study of flow uniformity and pressure characteristics within a microchannel array with triangular manifolds. *Computers & Chemical Engineering*, 52:134–144, 2013.

[114] Siemens Digital Industries Software. *Simcenter STAR-CCM+ User Guide v2021.1*. Siemens, 2021.

[115] H. Ebadi, F. Carrone, R. Difonzo, J. Fellinger, H.P. Laqua, N. Schneider, and L. Savoldi. A multi-scale hybrid approach to the modelling and design of a novel micro-channel cooling structure for the W7X divertor. *Case Studies in Thermal Engineering*, 42:102734, 2023.

[116] F. Carrone, R. Difonzo, J. Fellinger, and L. Savoldi. Multi-scale lumped modeling of micro-channels cooling structure for W7X divertor unit target module. *Fusion Engineering and Design*, 204:114481, 2024.

[117] N. Galanos, E. Papoutsis-Kiachagias, K. Giannakoglou, Y. Kondo, and K. Tanimoto. Synergistic use of adjoint-based topology and shape optimization for the design of Bi-fluid heat exchangers. *Structural and Multidisciplinary Optimization*, 65, 08 2022.

[118] K. Svanberg. The method of moving asymptotes—a new method for structural optimization. *Internat. J. Numer. Methods Eng.*, 24:359–373, 12 1987.

[119] L. Piegl and W. Tiller. *The NURBS Book, Monographs in Visual Communication (VISUALCOMM),*. Springer, 1995.

[120] L.S. Lazarov and O. Sigmund. Filters in topology optimization based on Helmoltz-type differential equations. *International Journal for Numerical Methods in Engineering*, 86:765–781, 2010.

[121] F. Wang, B.S. Lazarov, and O. Sigmund. On projection methods, convergence and robust formulations in topology optimization. *Structural and Multidisciplinary Optimization*, 43:767–784, 06 2011.

[122] P. Kalaria, P.T. Brucker, S. Ruess, S. Illy, K.A. Avramidis, G. Gantenbein, M. K. A. Thumm, and J. Jelonek. Design studies of mini-channel cavity cooling for a 170 GHz, 2 MW coaxial-cavity gyrotron. *2019 International Vacuum Electronics Conference (IVEC)*, pages 1–2, 2019.

[123] W. Rao and G. Liu et al. Thermal analysis of micro-channel cooling for a megawatt gyrotron travelling wave tube. In *Proceedings of the 2019 International Vacuum Electronics Conference (IVEC)*, pages 1–2, 2019.

[124] American Society of Mechanical Engineers. *ASME V&V 20.1 – Supplement to ASME V&V 20-2009 – Multivariate Metric for Validation*. American Society of Mechanical Engineers, 2009.

[125] T.H. Shih et al. A new $\kappa - \varepsilon$ eddy viscosity model for high reynolds number turbulent flows. *Computers & Fluids*, 24(3):227–238, 1995.

[126] H.K. Versteeg and W. Malalasekera. *An introduction to computational fluid dynamics - the finite volume method.* Addison-Wesley-Longman, 1995.

[127] F.R. Menter. Two-equation eddy-viscosity turbulence models for engineering applications. *AIAA Journal*, 32:1598–1605, 1994.

[128] S. Lardeau and F. Billard. Development of an elliptic-blending lag model for industrial applications. 01 2016.

[129] American Society of Mechanical Engineers. *Standard for Verification and Validation in Computational Fluid Dynamics and Heat Transfer*. American Society of Mechanical Engineers, 2009.

[130] JCGM. 100:2008, Evaluation of measurement data – Guide to the expression of uncertainty in measurement. Technical report.

[131] K. Avramidis et al. HCD-4.2.02-T012-D004-Report on the experimental tests with the mini-channel cavity mock-up. Technical report, Eurofusion, 2020.

Appendix A

Biogeography Based Optimization Algorithm

This appendix describes the general form of the BBO algorithm used in the work presented in Chapter 3. A simplification, with explanations (green comments), of the algorithm used for the optimzation work is reported. The algorithm was written in Java in order to allow the coupling with STAR-CCM+. For this reason, the coding language reported here is similar to the Java one.

The algorithm is reported, with some user defined functions. When a function is called, it is highlighted in the comments and its purpose is also explained. Differently from chapter 3, the name used for the immigration and emigration rates here correspond to the letters used in literature, hence lamda for the immigration rate and mu for the emigration rate.

DECLARATION

Ng=1000; number of optimization iterations used in the presented case

N; number of design variables

int P= represent the number of habitats (or individuals, the solutions) considered during the optimization cycle, at each iteration, hence it is the size of the population

INITIALIZATION

Initialize randomly the population

population=InitPopulation() (function to initialize the population

```
Cost function (HSI) evaluation

cost_stress=CostFunction(population,bounds,cost_penality);) (function to retrieve
the cost function value (Eq. 3.1) and the distance from constraint (on stress in this
case))

sort the population based on the HSI values, from the best (smallest in case of
minimization) to the worst

pop_cost=PopSort(population,cost,delta_stress); (function to sort the population

BBO ITERATIONS

for(int ii=1; ii<=Ng; ii++){

    Save the best design variables (HTC values) and the corresponding value of
    the cost function

    chromkeep=population[0];

    costkeep=cost[0];

    Evaluate the Species Counter (SC), giving informations on the number of
    species living an habitat, based on the HSI

    for(int j=0;j<Np;j++) {

    SC[j]=P-j-1; (the better the habitat is, the higher SC will be)

    } end of the evaluation of SC

    Evaluate the emigration and immigration rates, with a quadratic law

    for(int j=0;j<Np;j++){

    lamda[j]=Math.pow((1-SC[j]/P),2);

    mu[j]=Math.pow(SC[j]/P,2);

    } end of the evaluation of lamda and mu

    find the maximum value of lambda and the minimum value of mu. The Java
    language requires a for cycle that is not reported here.

    MIGRATION:use lambda and mu to decide how much information to share
    among habitats

    for(int k=0;k<Np;k++){
```

```
Normalize the immigration rate lambda
lambdascale= lambdaLower +(lambdaUpper− lambdaLower) ×(lambda[k]−lambda_min)
÷(lambda_max−lambda_min);
Probabilistically input new info into habitat i
for(int j=0;j<N;j++){
if(Math.random()<lambdascale){ generate a random number between 0 and 1
and compare with the normalized lambda
pick a habitat from which to obtain a feature
RandomNum=Math.random()*sum_mu;
Select=mu[0];
SelectIndex=0;
while(RandomNum>Select && SelectIndex<(Np-1)){
SelectIndex++;
Select=Select+mu[SelectIndex];
}// end while
island[k][j]=population[SelectIndex][j]; substitute one feature and save the
new habitat in the temporary variable island
} else {
island[k][j]=population[k][j];
}
} end of the for cycle over the design variables
} end migration process for the exhange of information
Replace the habitats with their new version
for(int k=0;k<Np;k++){
for(int j=0;j<N;j++){
population[k][j]=island[k][j];
}
```

```
        }
        Evaluate the cost function of the modified habitats
        cost_stress=CostFunction(population,bounds,cost_penality);
        for(int i=0;i<Np;i++){
        cost[i]=cost_stress[i][0]; Store cost function values and distance from the constraint limit on the stress
        delta_stress[i]=cost_stress[i][1];
        }
        Sort the population based on the HSI values, from the best (smallest in case of minimization) to the worst
        pop_cost=PopSort(population,cost,delta_stress); (function to sort the population
        ELITISM: replace worst with the previous generations elites
        Sort again the population based on the HSI values, from the best (smallest in case of minimization) to the worst
} end of BBO iterations
```